The Astrophysical Journal Supplement Series, 265:1 (32pp), 2023 March https://doi.org/10.3847/1538-4365/aca286

The TESS Grand Unified Hot Jupiter Survey. II. Twenty New Giant Planets*

Samuel W. Yee[1], Joshua N. Winn[1], Joel D. Hartman[1], Luke G. Bouma[2,56], George Zhou[3], Samuel N. Quinn[4], David W. Latham[4], Allyson Bieryla[4], Joseph E. Rodriguez[5], Karen A. Collins[4], Owen Alfaro[6], Khalid Barkaoui[7,8,9], Corey Beard[10], Alexander A. Belinski[11], Zouhair Benkhaldoun[12], Paul Benni[13], Krzysztof Bernacki[14], Andrew W. Boyle[2], R. Paul Butler[15], Douglas A. Caldwell[16,17], Ashley Chontos[18], Jessie L. Christiansen[19], David R. Ciardi[19], Kevin I. Collins[20], Dennis M. Conti[21], Jeffrey D. Crane[22], Tansu Daylan[1,57], Courtney D. Dressing[23], Jason D. Eastman[4], Zahra Essack[8,24], Phil Evans[25], Mark E. Everett[26], Sergio Fajardo-Acosta[27], Raquel Forés-Toribio[28,29], Elise Furlan[27], Mourad Ghachoui[7,12], Michaël Gillon[7], Coel Hellier[30], Ian Helm[6], Andrew W. Howard[2], Steve B. Howell[17], Howard Isaacson[3,23], Emmanuel Jehin[31], Jon M. Jenkins[17], Eric L. N. Jensen[32], John F. Kielkopf[33], Didier Laloum[21], Naunet Leonhardes-Barboza[34], Pablo Lewin[35], Sarah E. Logsdon[26], Jack Lubin[10], Michael B. Lund[19], Mason G. MacDougall[36], Andrew W. Mann[37], Natalia A. Maslennikova[11,38], Bob Massey[39], Kim K. McLeod[34], Jose A. Muñoz[28,29], Patrick Newman[6], Valeri Orlov[40], Peter Plavchan[6], Adam Popowicz[14], Francisco J. Pozuelos[7,31,41], Tyler A. Pritchard[42,43], Don J. Radford[44], Michael Reefe[6,24], George R. Ricker[24], Alexander Rudat[24], Boris S. Safonov[11], Richard P. Schwarz[4], Heidi Schweiker[26], Nicholas J. Scott[17], S. Seager[8,24,45], Stephen A. Shectman[22], Chris Stockdale[46], Thiam-Guan Tan[47,48], Johanna K. Teske[15], Neil B. Thomas[49], Mathilde Timmermans[7], Roland Vanderspek[24], David Vermilion[6], David Watanabe[50], Lauren M. Weiss[51], Richard G. West[52,53], Judah Van Zandt[36], Michal Zejmo[54], and Carl Ziegler[55]

[1] Department of Astrophysical Sciences, Princeton University, 4 Ivy Lane, Princeton, NJ 08544, USA
[2] Department of Astronomy, California Institute of Technology, Pasadena, CA 91125, USA
[3] University of Southern Queensland, Centre for Astrophysics, West Street, Toowoomba, QLD 4350, Australia
[4] Center for Astrophysics | Harvard & Smithsonian, 60 Garden Street, Cambridge, MA 02138, USA
[5] Center for Data Intensive and Time Domain Astronomy, Department of Physics and Astronomy, Michigan State University, East Lansing, MI 48824, USA
[6] George Mason University, 4400 University Drive, Fairfax, VA 22030, USA
[7] Astrobiology Research Unit, Université de Liège, 19C Allée du 6 Août, 4000 Liège, Belgium
[8] Department of Earth, Atmospheric and Planetary Sciences, Massachusetts Institute of Technology, Cambridge, MA 02139, USA
[9] Instituto de Astrofísica de Canarias (IAC), E-38205 La Laguna, Tenerife, Spain
[10] Department of Physics & Astronomy, University of California, Irvine, Irvine, CA 92697, USA
[11] Sternberg Astronomical Institute, M.V. Lomonosov Moscow State University, 13, Universitetskij pr., 119234, Moscow, Russia
[12] Oukaimeden Observatory, High Energy Physics and Astrophysics Laboratory, Faculty of Sciences Semlalia, Cadi Ayyad University, Marrakech, Morocco
[13] Acton Sky Portal (Private Observatory), Acton, MA, USA
[14] Silesian University of Technology, Department of Electronics, Electrical Engineering and Microelectronics, Akademicka 16, 44-100 Gliwice, Poland
[15] Earth and Planets Laboratory, Carnegie Institution for Science, 5241 Broad Branch Road, NW, Washington, DC 20015, USA
[16] SETI Institute, USA
[17] NASA Ames Research Center, Moffett Field, CA 94035, USA
[18] Institute for Astronomy, University of Hawai'i, Honolulu, HI 96822, USA
[19] Caltech/IPAC-NASA Exoplanet Science Institute, 770 S. Wilson Avenue, Pasadena, CA 91106, USA
[20] George Mason University, 4400 University Drive, Fairfax, VA, 22030 USA
[21] American Association of Variable Star Observers, 49 Bay State Road, Cambridge, MA 02138, USA
[22] Observatories of the Carnegie Institution for Science, 813 Santa Barbara Street, Pasadena, CA 91101, USA
[23] Department of Astronomy, University of California Berkeley, Berkeley, CA 94720, USA
[24] Department of Physics and Kavli Institute for Astrophysics and Space Research, Massachusetts Institute of Technology, Cambridge, MA 02139, USA
[25] El Sauce Observatory, Coquimbo, 1870000, Chile
[26] NSF's National Optical-Infrared Astronomy Research Laboratory, 950 N. Cherry Avenue, Tucson, AZ 85719, USA
[27] NASA Exoplanet Science Institute, Caltech/IPAC, Mail Code 100-22, 1200 E. California Boulevard, Pasadena, CA 91125, USA
[28] Departamento de Astronomía y Astrofísica, Universidad de Valencia, E-46100 Burjassot, Valencia, Spain
[29] Observatorio Astronómico, Universidad de Valencia, E-46980 Paterna, Valencia, Spain
[30] Astrophysics Group, Keele University, Staffordshire, ST5 5BG, UK
[31] Space sciences, Technologies and Astrophysics Research (STAR) Institute, Université de Liège, Belgium
[32] Department of Physics & Astronomy, Swarthmore College, Swarthmore, PA 19081, USA
[33] Department of Physics and Astronomy, University of Louisville, Louisville, KY 40292, USA
[34] Department of Astronomy, Wellesley College, Wellesley, MA 02481, USA
[35] The Maury Lewin Astronomical Observatory, Glendora, CA 91741, USA
[36] Department of Physics & Astronomy, University of California Los Angeles, Los Angeles, CA 90095, USA
[37] Department of Physics and Astronomy, The University of North Carolina at Chapel Hill, Chapel Hill, NC 27599-3255, USA
[38] Faculty of Physics, Moscow State University, 1 bldg. 2, Leninskie Gory, Moscow 119991, Russia
[39] Villa '39 Observatory, Landers, CA 92285, USA
[40] Instituto de Astronomía, Universidad Nacional Autónoma de México, Apdo. Postal 70-264, Cd. Universitaria, 04510 CDMX, México
[41] Instituto de Astrofísica de Andalucía (IAA-CSIC), Glorieta de la Astronomía s/n, E-18008 Granada, Spain
[42] University of Maryland, College Park, MD 20742, USA
[43] NASA Goddard Space Flight Center, Greenbelt, MD 20771, USA
[44] Brierfield Observatory, New South Wales, Australia
[45] Department of Aeronautics and Astronautics, Massachusetts Institute of Technology, 77 Massachusetts Avenue, Cambridge, MA 02139, USA
[46] Hazelwood Observatory, Australia

* This paper includes data gathered with the 6.5 m Magellan Telescopes located at Las Campanas Observatory, Chile

[47] Perth Exoplanet Survey Telescope, Perth, Australia
[48] Curtin Institute of Radio Astronomy, Curtin University, Bentley, 6102, Australia
[49] Department of Astronautics, United States Air Force Academy, CO 80840, USA
[50] Planetary Discoveries, Fredericksburg, VA 22405, USA
[51] Department of Physics and Astronomy, University of Notre Dame, Notre Dame, IN 46556, USA
[52] Centre for Exoplanets and Habitability, University of Warwick, Coventry, CV4 7AL, UK
[53] Department of Physics, University of Warwick, Coventry, CV4 7AL, UK
[54] Janusz Gil Institute of Astronomy, University of Zielona Gora, Prof. Szafrana 2, PL-65-516 Zielona Gora, Poland
[55] Department of Physics, Engineering and Astronomy, Stephen F. Austin State University, 1936 North Street, Nacogdoches, TX 75962, USA
Received 2022 September 15; revised 2022 October 26; accepted 2022 November 3; published 2023 February 13

Abstract

NASA's Transiting Exoplanet Survey Satellite (TESS) mission promises to improve our understanding of hot Jupiters by providing an all-sky, magnitude-limited sample of transiting hot Jupiters suitable for population studies. Assembling such a sample requires confirming hundreds of planet candidates with additional follow-up observations. Here we present 20 hot Jupiters that were detected using TESS data and confirmed to be planets through photometric, spectroscopic, and imaging observations coordinated by the TESS Follow-up Observing Program. These 20 planets have orbital periods shorter than 7 days and orbit relatively bright FGK stars ($10.9 < G < 13.0$). Most of the planets are comparable in mass to Jupiter, although there are four planets with masses less than that of Saturn. TOI-3976b, the longest-period planet in our sample ($P = 6.6$ days), may be on a moderately eccentric orbit ($e = 0.18 \pm 0.06$), while observations of the other targets are consistent with them being on circular orbits. We measured the projected stellar obliquity of TOI-1937A b, a hot Jupiter on a 22.4 hr orbit with the Rossiter–McLaughlin effect, finding the planet's orbit to be well aligned with the stellar spin axis ($|\lambda| = 4.^{\circ}0 \pm 3.^{\circ}5$). We also investigated the possibility that TOI-1937 is a member of the NGC 2516 open cluster but ultimately found the evidence for cluster membership to be ambiguous. These objects are part of a larger effort to build a complete sample of hot Jupiters to be used for future demographic and detailed characterization work.

Unified Astronomy Thesaurus concepts: Exoplanets (498); Hot Jupiters (753); Radial velocity (1332); Exoplanet detection methods (489); Transit photometry (1709)

Supporting material: data behind figure, figure sets, machine-readable table

1. Introduction

Hot Jupiters were among the first extrasolar planets to be discovered, initiating the longest-running mystery in exoplanet science—how did these gas giant planets come to occupy such small orbits? The core-accretion theory for giant planet formation, which was devised before the discovery of any exoplanets, held that giant planets could only form at distances of a few astronomical units, beyond the ice line (see, e.g., Lissauer 1993). Dawson & Johnson (2018) and Fortney et al. (2021) reviewed the three main categories of theory that have emerged to explain the existence of hot Jupiters—in situ formation, inward migration of initially wide-orbiting planets via gravitational interactions with the protoplanetary gas disk, and eccentricity excitation followed by tidal dissipation.

Even though we now know of hundreds of hot Jupiters, it is not yet clear which of these processes, if any, is primarily responsible for the production of hot Jupiters. One line of evidence that may help us shed light on this mystery is the study of the demographics of the hot Jupiter population—the distribution of planet properties, the joint distribution of planetary and stellar properties, and the dependence of all these distributions on other aspects of planetary systems such as wide-orbiting companions. However, hot Jupiter demographics have been difficult to determine, in part because hot Jupiters are rare, occurring around 0.5%–1% of Sunlike stars (e.g., Mayor et al. 2011; Wright et al. 2012; Fressin et al. 2013), and also because most of the currently known hot Jupiters were discovered by a heterogeneous collection of surveys with poorly characterized selection biases.

NASA's Transiting Exoplanet Survey Satellite (TESS) mission provides an opportunity to clarify hot Jupiter demographics. As an all-sky survey with the photometric precision to be nearly complete to transiting hot Jupiters around relatively bright stars (Zhou et al. 2019), TESS will not only discover hundreds of new hot Jupiters but will also allow us to unify the previously discovered hot Jupiters into a homogeneous sample with a well-characterized selection function. A magnitude-limited sample of stars brighter than a Gaia G magnitude of 12.5 will host ~400 transiting hot Jupiters (Yee et al. 2021), an order of magnitude larger than the previous best statistical samples (from the Kepler mission and radial velocity [RV] surveys). Of these 400 planets, ≈40% are already known from the previous ground-based transit surveys. In fact, TESS has already begun to provide some insights into the demographics of hot Jupiters. Zhou et al. (2019) and Beleznay & Kunimoto (2022) investigated the dependence of hot Jupiter occurrence on stellar mass based on 18 and 97 TESS planet candidates, respectively, finding tentative evidence for an anticorrelation between the occurrence rate and stellar mass for AFG stellar hosts.

However, while the TESS mission has announced hundreds of new hot Jupiter planet candidates as TESS Objects of Interest (TOIs) (Guerrero et al. 2021; Kunimoto et al. 2022), follow-up observations are key to separating the true planets from the false positives in this sample, as well as characterizing the planets and their host stars. A major factor

[56] 51 Pegasi b Fellow.
[57] LSSTC Catalyst Fellow.

Table 1
Summary of New Planetary Systems

TOI	TIC	G (mag)	Stellar $T_{\rm eff}$ (K)	Stellar Radius ($R_\odot$)	Orbital Period (days)	Planet Radius (R_J)	Planet Mass (M_J)
TOI-1937A b	268301217	13.02	5814^{+91}_{-93}	$1.080^{+0.025}_{-0.024}$	0.947	$1.247^{+0.059}_{-0.062}$	$2.01^{+0.17}_{-0.16}$
TOI-2364b	39414571	12.09	5306^{+76}_{-68}	$0.886^{+0.021}_{-0.017}$	4.020	$0.768^{+0.023}_{-0.018}$	$0.225^{+0.043}_{-0.049}$
TOI-2583A b	7548817	12.46	5936^{+65}_{-68}	$1.477^{+0.036}_{-0.032}$	4.521	$1.290^{+0.040}_{-0.033}$	$0.250^{+0.058}_{-0.056}$
TOI-2587A b	68007716	11.41	5760^{+80}_{-79}	$1.726^{+0.049}_{-0.047}$	5.457	$1.077^{+0.042}_{-0.040}$	$0.218^{+0.054}_{-0.046}$
TOI-2796b	220076110	12.36	5764^{+81}_{-78}	1.069 ± 0.024	4.808	1.59 (>1.54)	$0.44^{+0.10}_{-0.11}$
TOI-2803A b	124379043	12.43	6280^{+99}_{-96}	$1.245^{+0.022}_{-0.021}$	1.962	$1.616^{+0.034}_{-0.032}$	$0.975^{+0.083}_{-0.070}$
TOI-2818b	151483286	11.84	5721^{+88}_{-83}	$1.229^{+0.032}_{-0.031}$	4.040	$1.363^{+0.046}_{-0.045}$	0.71 ± 0.26
TOI-2842b	178162579	12.46	5910 ± 100	$1.265^{+0.040}_{-0.037}$	3.551	$1.146^{+0.051}_{-0.048}$	$0.370^{+0.052}_{-0.047}$
TOI-2977b	361343239	12.44	5691^{+94}_{-93}	$1.073^{+0.024}_{-0.020}$	2.351	$1.174^{+0.031}_{-0.027}$	$1.68^{+0.26}_{-0.25}$
TOI-3023b	454248975	12.03	5760^{+85}_{-88}	$1.668^{+0.046}_{-0.033}$	3.901	$1.466^{+0.043}_{-0.032}$	$0.62^{+0.10}_{-0.09}$
TOI-3364b	280655495	11.29	5706^{+95}_{-91}	$1.419^{+0.036}_{-0.030}$	5.877	$1.091^{+0.038}_{-0.032}$	$1.67^{+0.12}_{-0.13}$
TOI-3688A b	245509452	12.37	5950 ± 100	$1.302^{+0.038}_{-0.035}$	3.246	$1.167^{+0.048}_{-0.044}$	$0.98^{+0.10}_{-0.11}$
TOI-3807b	289661991	12.03	5772^{+84}_{-80}	1.468 ± 0.037	2.899	2.00 (>1.65)	$1.04^{+0.15}_{-0.14}$
TOI-3819b	95660472	12.41	5859^{+72}_{-71}	1.538 ± 0.037	3.244	$1.172^{+0.036}_{-0.035}$	$1.11^{+0.18}_{-0.20}$
TOI-3912b	156648452	12.31	5725^{+69}_{-68}	$1.392^{+0.035}_{-0.034}$	3.494	$1.274^{+0.041}_{-0.040}$	$0.406^{+0.071}_{-0.068}$
TOI-3976A b	154293917	12.22	5975^{+70}_{-69}	$1.501^{+0.039}_{-0.038}$	6.608	$1.095^{+0.036}_{-0.035}$	$0.175^{+0.037}_{-0.036}$
TOI-4087b	310002617	11.71	6060^{+74}_{-67}	$1.112^{+0.021}_{-0.020}$	3.177	$1.164^{+0.025}_{-0.024}$	0.73 ± 0.14
TOI-4145A b	279947414	12.06	5281^{+86}_{-76}	$0.859^{+0.018}_{-0.017}$	4.066	$1.187^{+0.032}_{-0.031}$	0.43 ± 0.13
TOI-4463A b	8599009	10.95	5640^{+89}_{-82}	$1.062^{+0.027}_{-0.024}$	2.881	$1.183^{+0.064}_{-0.045}$	$0.794^{+0.039}_{-0.040}$
TOI-4791b	100389539	11.32	6058^{+99}_{-94}	$1.409^{+0.039}_{-0.038}$	4.281	1.110 ± 0.050	$2.31^{+0.32}_{-0.33}$

Note. We summarize the key stellar and planetary properties for the 20 new hot Jupiter systems described in this paper, as derived from our global fits (Section 4).

in our ability to confirm hundreds of planets is the successful operation of the TESS Follow-Up Observing Program (TFOP; Collins et al. 2018; ExoFOP 2019),[58,59] in which any interested astronomer is invited to participate. The TFOP helps to organize and coordinate follow-up observations between members of the community, thereby maximizing observing efficiency.

We began the TESS Grand Unified Hot Jupiter Survey (Yee et al. 2022, hereafter Paper I) to accelerate the process of building up a magnitude-complete sample of hot Jupiters ($P < 10$ days, $8\,R_\oplus \leqslant R_p \leqslant 24\ R_\oplus$), by coordinating between follow-up groups, performing new observations, and characterizing each planet candidate. The first 10 planets found in our survey were described in Paper I. In this paper, we present 20 new planets discovered by TESS and confirmed by ground-based follow-up observations. These planets orbit FGK stars brighter than $G = 13$ mag, have orbital periods $P < 7$ days, and have masses between $0.18\,M_J$ and $2.3\,M_J$, as determined by high-precision RV observations. A summary of the new planets is provided in Table 1.

Section 2 of this paper describes the photometric, imaging, and spectroscopic observations; Section 3 presents our characterization of the planet host stars; and Section 4 describes our global modeling of the planetary systems with `EXOFASTv2`. Because our data collection and analysis procedures are similar to those described in Paper I, we describe them more concisely in this paper. We discuss our results and place the new systems in the context of the broader hot Jupiter sample in Section 5.

[58] https://heasarc.gsfc.nasa.gov/docs/tess/followup.html
[59] https://exofop.ipac.caltech.edu/tess/

2. Observations and Data

2.1. TESS Photometry

The 20 planets described in this paper were first identified as transiting planet candidates in the TESS photometry. None of them orbit stars that had been preselected for 2 minute cadence observations during the TESS Prime Mission (sectors 1–26). Instead, the TESS photometry for these targets during the Prime Mission comes from the full-frame images (FFIs), which were combined and downloaded at 30 minute cadence. Following the conclusion of its Prime Mission in July 2020, TESS reobserved most of the sky as part of the first Extended Mission (EM1). Six of our targets (TOI-1937b, -2583b, -3807b, -3819b, -3912b, and -4087b) were identified as planet candidates based on Prime Mission data and selected for 2 minute cadence observations during EM1. The remaining objects continued to be observed as part of the FFIs, which are available with a 10 minute cadence in EM1. Table 2 summarizes the TESS observations for each target.

The short-cadence data were reduced by the TESS Science Processing Operations Center (SPOC) pipeline (Jenkins et al. 2016), with light curves extracted from the "postage stamp" images around each selected target. The SPOC pipeline computes optimal apertures to extract light curves from each target and estimates the contamination from stars within the same aperture to correct the flux levels. Meanwhile, the FFI data were calibrated with the `tica` software (Fausnaugh et al. 2020) and light curves were extracted with the MIT Quick-Look Pipeline (QLP; Huang et al. 2020a, 2020b; Kunimoto et al. 2021). The QLP produces light curves for each target using difference imaging, subtracting each frame from a reference frame generated from the median of 40 frames with minimal scattered light. This approach automatically accounts for any contamination from other stars within the same aperture. The TESS SPOC pipeline has also recently begun

Table 2
Summary of TESS Observations

Target	Sector	Source[a]	Cadence (s)
TOI-1937A	7,9	CDIPS	1800
⋯	34–36	SPOC	120
TOI-2364	6	SPOC	1800
⋯	33	SPOC	600
TOI-2583A	14,25,26	SPOC	1800
⋯	40	SPOC	120
TOI-2587A	7	SPOC	1800
⋯	34	SPOC	600
TOI-2796	6	SPOC	1800
⋯	32	SPOC	600
TOI-2803A	6	QLP	1800
⋯	33	QLP	600
TOI-2818	7,8	QLP	1800
⋯	34	QLP	600
TOI-2842	7	QLP	1800
⋯	33	QLP	600
TOI-2977	9	QLP	1800
⋯	36,37	QLP	600
TOI-3023	10,12	SPOC	1800
⋯	37	QLP	600
⋯	38	SPOC	600
TOI-3364	9	SPOC	1800
⋯	35,36	SPOC	600
TOI-3688A	18	QLP	1800
TOI-3807	14,20	SPOC	1800
⋯	47	SPOC	120
TOI-3819	20	SPOC	1800
⋯	44–47	SPOC	120
TOI-3912	23	SPOC	1800
⋯	50	SPOC	120
TOI-3976A	16,23,24	SPOC	1800
TOI-4087	14,19,21,26	SPOC	1800
⋯	40,41,47	SPOC	120
TOI-4145A	18,19,25,26	SPOC	1800
TOI-4463A	26	SPOC	1800
TOI-4791	33,34	SPOC	600

Notes. The raw TESS data are available on MAST, while the flattened and normalized TESS photometry used in our analysis are provided as online supplementary material (data behind the figure for Figure 15).
[a] The source column indicates the High-Level Science Product source of the TESS light curves used in the analysis.

extracting light curves for a subset of the targets in the FFIs (Caldwell et al. 2020), and we use these light curves when available.

The transit signals of the majority of our targets were first found through a box least-squares transit search (Kovács et al. 2002; Hartman & Bakos 2016) of the QLP light curves. These transit events were then triaged and vetted by the TESS Science Office (Yu et al. 2019; Kunimoto et al. 2022) before being announced to the community as TESS TOIs (Guerrero et al. 2021).

Eight of the targets described here were first identified by other investigators and announced as "community TOIs" (cTOIs). TOI-1937A b and TOI-4145b were found by the Cluster Difference Imaging Photometric Survey (CDIPS; Bouma et al. 2019), which extracted light curves of potential members of stellar clusters from the FFI data and searched the data for transiting planet candidates. We discuss the potential cluster membership of these two targets in Section 3.3. TOI-2364b and TOI-2796b were identified and vetted as planet candidates by Montalto et al. (2020), who used the DIAmante difference imaging pipeline to extract light curves from the first year of TESS FFIs and performed an independent box least-squares transit search. Olmschenk et al. (2021) flagged TOI-2583b, TOI-2818b, TOI-2842b, TOI-4087b, and TOI-4145b in their search of the FFI light curves extracted by the `eleanor` pipeline (Feinstein et al. 2019), using the Quasiperiodic Automatic Transit Search (QATS; Carter & Agol 2013; Kruse et al. 2019) and Discovery and Vetting of Exoplanets (DAVE; Kostov et al. 2019) pipelines to identify and vet the transit candidates. All six targets underwent further vetting by the TESS Science Office and were subsequently also flagged as TOIs (Mireles et al. 2021).

We used the `lightkurve` Python package (Lightkurve Collaboration et al. 2018) to download all available TESS photometry from the Mikulski Archive for Space Telescopes (MAST). When available, we used the Presearch Data Conditioning (PDC; Smith et al. 2012; Stumpe et al. 2012, 2014) light curves produced by the SPOC pipeline, which have been corrected for instrumental systematics. When SPOC light curves were unavailable, we used those produced by the QLP, except for the case of TOI-1937A. For the sector 7 and 9 observations of TOI-1937A, we used the CDIPS light curves based on the smallest choice of aperture (`IRM1`).

While inspecting the light curves, we noticed that the TESS Sector 9 QLP light curve for TOI-2977 showed a different transit depth from the QLP light curves from sectors 36 and 37. We determined that this was due to a 0.6 mag difference in the TESS magnitudes between versions 7 and 8 of the TESS Input Catalog (TIC; Stassun et al. 2018, 2019). These magnitudes are used by the QLP to convert the difference fluxes into absolute fluxes, with TICv7 used for light curves from the TESS Prime Mission, while TICv8 was used for TESS EM1 light curves. We therefore used the updated TICv8 magnitude to correct the sector 9 light curve for TOI-2977, bringing the resulting transit depth into agreement with those from the later sectors and ground-based photometry.

Before using the TESS data to help determine the system properties (Section 4), we "flattened" the SPOC light curves using the `Keplerspline`[60] routine (Vanderburg & Johnson 2014; Shallue & Vanderburg 2018), which attempts to eliminate variations in the light curve due to stellar variability and residual instrumental effects. In this step, we also normalized the light curves such that the data obtained outside of transits has a mean flux of unity. We note that the QLP data were already detrended using this procedure during the light-curve production process. For our analysis, we used only the segments of the light curves that are centered on transits and span three transit durations, excluding the remaining out-of-transit data. All the raw TESS data used in this manuscript can be found on MAST, while the flattened and normalized TESS photometry data are provided as online supplementary material.

2.2. WASP Photometry

Two of our targets, TOI-2583b and TOI-2803b, were also detected as planet candidates by the WASP transit search (Pollacco et al. 2006). The WASP survey comprises two wide-field camera arrays at the Observatorio del Roque de los Muchachos on La Palma and the Sutherland Station of the South African Astronomical Observatory (SAAO). TOI-2583

[60] https://github.com/avanderburg/keplersplinev2

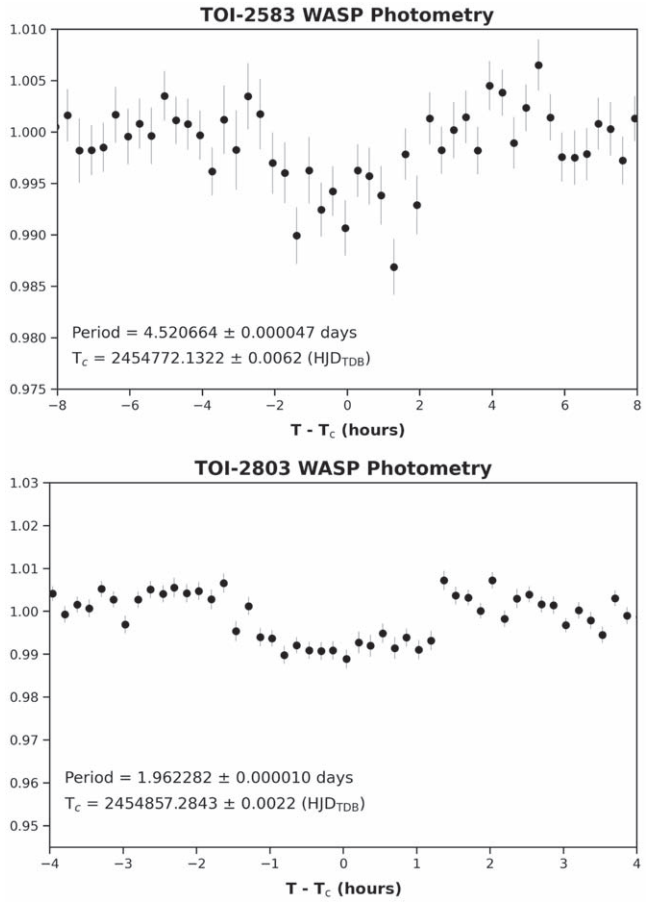

Figure 1. WASP photometry for TOI-2583 (top) and TOI-2803 (bottom), binned and phase folded onto the ephemeris found by the WASP transit-finding algorithm.

was observed by WASP between 2004 and 2010, while TOI-2803 was observed between 2006 and 2012, with the transit events detected at the same period as those found by TESS. Figure 1 shows the phase-folded WASP photometry for these two objects. To incorporate the power from the long baseline of the WASP photometry in our fits, we use the times of conjunction found by the WASP transit search algorithm ($T_c = 2454772.1322 \pm 0.0062$ $\mathrm{HJD_{TDB}}$ for TOI-2583b; $T_c = 2454857.2843 \pm 0.0022$ $\mathrm{HJD_{TDB}}$ for TOI-2803b) as a prior for our global fits (Section 4).

In addition to TOI-2583 and TOI-2803, archival WASP photometry was also available for TOI-2587, TOI-3364, TOI-3819, TOI-3912, and TOI-3976. We searched the WASP photometry of all targets to check for rotational modulation. In all cases, no significant modulations were detected, with 95% upper limits between 1 and 3 mmag.

2.3. Follow-up Ground-based Photometry

Apart from the TESS and archival WASP photometry, we obtained additional light curves from a wide range of ground-based facilities, organized by the TFOP Seeing-limited Photometry Sub-Group 1. The superior angular resolution of the ground-based photometry (typically a few arcseconds) compared with that of TESS helped to rule out the possibility that the transit-like fading events are actually due to a nearby eclipsing binary rather than the intended target star. In some cases, the target was observed in multiple photometric bands, and the lack of chromatic variation in transit depths was evidence that the transit events are due to a planetary companion rather than a luminous companion. The ground-based observations also extended the timespan over which transits have been detected, thereby allowing the orbital period to be determined with greater precision.

We summarize all the ground-based follow-up photometry in Table 3. The observations from the Perth Exoplanet Survey Telescope (PEST) were reduced by a custom software package,[61] while the TRAPPIST-North (Gillon et al. 2011; Barkaoui et al. 2019) observations were reduced with the procedures described by Gillon et al. (2013). The five light curves of TOI-1937 obtained from the Las Cumbres Observatory Global Telescope (LCOGT; Brown et al. 2013) were extracted from the calibrated science images produced by the LCOGT network using aperture photometry routines from the FITSH package (Pal 2012). For all remaining observations, data reduction and aperture photometry were performed using the `AstroImageJ` software (Collins et al. 2017), with scheduling assisted by the `TAPIR` software (Jensen 2013).

We included most of the ground-based time-series photometry in our global fits (Section 4), simultaneously fitting a transit model while detrending against the columns listed in Table 3. The TRAPPIST-North light curve of TOI-2364, the MLO light curve of TOI-3688, and the 2021 November 19 GMU light curve of TOI-3819 were excluded from the fits because no transits were detected in those light curves. The nondetections are all consistent with the ephemerides derived from the rest of the data. For TOI-2583, we also excluded the OAUV light curve, for which the data during the transit were strongly affected by variable sky conditions. All of the ground-based time-series photometry data are available through ExoFoP (see footnote 59) and as supplementary material accompanying this paper.

2.4. High Angular Resolution Imaging

As part of follow-up observations coordinated by the TFOP High-Resolution Imaging Sub-Group 3 (SG3), we obtained high angular-resolution imaging of all the targets described here. Observations were made using the 'Alopeke and Zorro speckle cameras on the Gemini-North and Gemini-South telescopes, respectively (Scott et al. 2021), and reduced according to the procedures in Howell et al. (2011); the High-Resolution Camera (HRCam; Tokovinin & Cantarutti 2008) speckle imaging instrument on the Southern Astrophysical Research (SOAR) 4.1 m telescope; the ShARCS camera using the adaptive optics system on the Shane 3 m telescope at Lick Observatory (Kupke et al. 2012; Gavel et al. 2014; McGurk et al. 2014); the NN-explore Exoplanet Stellar Speckle Imager (NESSI; Scott et al. 2018) on the WIYN 3.5 m telescope at Kitt Peak National Observatory (KPNO); the speckle polarimeter on the 2.5 m telescope at the Caucasian Mountain Observatory (CMO) of Sternberg Astronomical Institute (SAI) of Lomonosov Moscow State University (Safonov et al. 2017); and the Palomar High Angular Resolution Observer (PHARO; Hayward et al. 2001) on the 200 inch Hale telescope at Palomar Observatory. The observation strategy and data reduction procedures for the SOAR observations are described in Tokovinin (2018), Ziegler & Tokovinin (2019), and Ziegler et al. (2021), while the ShARCS observations were reduced with the publicly available

[61] http://pestobservatory.com/the-pest-pipeline/

Table 3
Summary of Ground-based Photometric Follow-up Observations

Target	Facility/Instrument	Aperture (m)	Filter	Date (UT)	Cadence (s)	Used in Fit	Precision[a] (mmag)	Detrending Vectors
TOI-1937A	LCO SSO/Sinistro	1.0	i'	2020 Jan 22	207	Y	0.8	BJD_{TDB}, $(BJD_{TDB})^2$, Shape (S)
⋯	LCO CTIO/Sinistro	1.0	i'	2020 Jan 29	207	Y	1.0	BJD_{TDB}, $(BJD_{TDB})^2$, Shape (S)
⋯	LCO SAAO/Sinistro	1.0	i'	2020 Jan 31	207	Y	2.7	BJD_{TDB}, $(BJD_{TDB})^2$, Shape (S)
⋯	LCO CTIO/Sinistro	1.0	g'	2020 Feb 13	207	Y	1.2	BJD_{TDB}, $(BJD_{TDB})^2$, Shape (S)
⋯	El Sauce	0.36	R	2020 Feb 14	180	Y	4.0	Airmass
⋯	LCO SSO/Sinistro	1.0	z'	2020 Apr 22	207	Y	1.5	BJD_{TDB}, $(BJD_{TDB})^2$, Shape (S)
⋯	El Sauce	0.36	V	2020 Dec 29	180	Y	5.7	Airmass
TOI-2364	TRAPPIST-North	0.6	z'	2020 Nov 28	25	N	⋯	⋯
⋯	Hazelwood	0.318	R	2021 Jan 8	180	Y	2.2	Total Counts
TOI-2583A	WASP	⋯	WASP	2004 May 14	40	N	⋯	⋯
⋯	TRAPPIST-North	0.6	$I+z$	2021 May 7	20	Y	2.7	Meridian Flip
⋯	OAUV/T50	0.5	R	2021 May 16	150	N	⋯	⋯
⋯	FLWO/KeplerCam	1.2	B	2021 Jun 13	180	Y	2.3	Airmass
⋯	FLWO/KeplerCam	1.2	z'	2021 Jun 13	180	Y	2.2	Airmass
⋯	Mount Lemmon/ULMT	0.6	g'	2021 Jun 22	128	Y	2.1	⋯
TOI-2587A	FLWO/KeplerCam	1.2	i'	2021 Mar 31	28	Y	7.2	Airmass
⋯	Mount Lemmon/ULMT	0.6	r'	2021 Mar 31	64	Y	1.9	Total Counts, J.D.-2400000
TOI-2796	LCO SSO/SBIG-6303	0.4	i'	2021 Sep 1	120	Y	3.4	Airmass, BJD_{TDB}
⋯	El Sauce	0.36	B	2021 Nov 3	180	Y	7.1	Airmass, Sky/Pixel
⋯	CMO/RC600	0.6	g'	2021 Dec 6	50	Y	2.3	Airmass
TOI-2803A	WASP	⋯	WASP	2006 Oct 20	40	N	⋯	⋯
⋯	Brierfield	0.36	R	2021 Oct 6	180	Y	2.7	Airmass
⋯	LCO CTIO/SBIG-6303	0.4	i'	2021 Oct 25	140	Y	3.9	Airmass, Total Counts, FWHM
⋯	El Sauce	0.36	B	2021 Oct 28	180	Y	4.1	Airmass
⋯	LCO SSO/SBIG-6303	0.4	g'	2021 Dec 2	140	Y	6.7	⋯
⋯	Brierfield	0.36	B	2021 Dec 2	240	Y	7.0	Airmass
TOI-2818	El Sauce	0.51	R	2021 Dec 8	30	Y	3.0	Airmass, Total Counts
⋯	LCO CTIO/SBIG-6303	0.4	g'	2021 Dec 12	60	Y	9.6	⋯
TOI-2842	El Sauce	0.36	R	2021 Nov 5	180	Y	3.3	Airmass
⋯	El Sauce	0.51	B	2021 Dec 7	180	Y	2.8	Airmass, Sky/Pixel
TOI-2977	El Sauce	0.51	R	2022 Jan 8	60	Y	2.3	Y position
⋯	PEST	0.3	g'	2022 Feb 26	250	Y	3.3	FWHM
⋯	PEST	0.3	i'	2022 Feb 26	250	Y	4.7	FWHM
TOI-3023	Brierfield	0.36	i'	2021 Jun 25	240	Y	2.2	⋯
⋯	El Sauce	0.51	R	2022 Jan 26	60	Y	3.0	Airmass, FWHM
TOI-3364	Hazelwood	0.318	R	2021 Dec 12	120	Y	2.6	FWHM
TOI-3688A	MLO	0.356	i'	2021 Oct 9	90	N	⋯	⋯
⋯	FLWO/KeplerCam	1.2	i'	2021 Dec 1	34	Y	2.7	Airmass
TOI-3807	GMU/SBIG-16803	0.8	R	2021 Nov 23	60	Y	3.8	Airmass, FWHM, Sky/Pixel
⋯	Acton Sky Portal	0.36	r'	2021 Nov 24	35	Y	5.1	Airmass
⋯	FLWO/KeplerCam	1.2	i'	2022 Feb 16	96	Y	4.5	Airmass
⋯	FLWO/KeplerCam	1.2	B	2022 Feb 16	96	Y	4.7	Airmass
⋯	FLWO/KeplerCam	1.2	B	2022 Mar 23	120	Y	2.4	FWHM
⋯	FLWO/KeplerCam	1.2	z	2022 Mar 23	120	Y	2.9	FWHM
TOI-3819	GMU/SBIG-16803	0.8	R	2021 Nov 19	70	N	⋯	⋯
⋯	GMU/SBIG-16803	0.8	R	2022 Feb 11	70	Y	4.4	Airmass, Sky/Pixel, X position
⋯	FLWO/KeplerCam	1.2	i'	2022 Apr 18	40	Y	1.9	Airmass
TOI-3912	OAUV/T50	0.5	R	2021 Jul 15	120	Y	3.1	BJD_{TDB}, Airmass
⋯	SUTO/OTIVAR	0.3	B	2022 Mar 20	300	Y	6.2	Airmass
⋯	FLWO/KeplerCam	1.2	i'	2022 Mar 24	40	Y	2.1	Airmass, Total Counts
⋯	Villa '39	0.355	B	2022 Mar 31	360	Y	2.8	Airmass
⋯	Villa '39	0.355	i'	2022 Mar 31	240	Y	2.5	Airmass, Meridian Flip
TOI-3976A	FLWO/KeplerCam	1.2	i'	2022 Apr 22	36	Y	2.8	Airmass
TOI-4087	OAUV/T50	0.5	R	2021 Oct 4	75	Y	4.0	Total Counts, Y position
⋯	SUTO/OTIVAR	0.3	B	2022 Apr 19	300	Y	3.8	Airmass
TOI-4145A	OPM/RC8	0.2	I	2021 Aug 23	120	Y	8.8	Airmass
⋯	SUTO/OTIVAR	0.3	B	2021 Dec 28	180	Y	6.3	Airmass
TOI-4463A	Mount Lemmon/ULMT	0.6	r'	2022 Apr 25	48	Y	1.5	Total Counts
⋯	Brierfield	0.36	R	2022 Jun 7	120	Y	6.8	Airmass
⋯	Whitin/CDK700	0.7	z'	2022 Jun 16	30	Y	2.5	Airmass
⋯	Whitin/CDK700	0.7	g'	2022 Jun 16	30	Y	1.8	Airmass

Table 3
(Continued)

Target	Facility/Instrument	Aperture (m)	Filter	Date (UT)	Cadence (s)	Used in Fit	Precision[a] (mmag)	Detrending Vectors
TOI-4791	PEST	0.3	*R*	2022 Jan 17	120	Y	3.0	FWHM, Sky/Pixel

Notes. The ground-based follow-up photometry is publicly available via ExoFoP (see footnote 59) and are also provided as online supplementary material (data behind the figure for Figure 15). The following facilities were used for ground-based photometric observations: 0.4 m and 1.0 m telescopes of the LCOGT (Brown et al. 2013) using sites at Siding Spring Observatory (SSO), Cerro Tololo Inter-American Observation (CTIO), and the SAAO; the 0.36 m and 0.51 m telescopes at the El Sauce Observatory; TRAPPIST-North at the Oukaimeden Observatory (Gillon et al. 2011; Jehin et al. 2011; Barkaoui et al. 2019); the Hazelwood Observatory; the Observatori Astronòmic de la Universitat de València (OAUV) T50 0.5 m telescope; KeplerCam on the Fred Lawrence Whipple Observatory (FLWO) 1.2 m telescope; the University of Louisville Manner Telescope (ULMT) at Mount Lemmon; the Caucasian Mountain Observatory (CMO); the Brierfield Observatory; PEST; the Maury Lewin Astronomical Observatory (MLO); the 0.8 m telescope at George Mason University (GMU) with automation described in Reefe et al. (2022); the Acton Sky Portal; the Silesian University of Technology Observatories (SUTO) OTIVAR 0.3 m telescope; the Villa '39 observatory; the private observatory of the Mount at Saint-Pierre-du-Mont, France (OPM); and the Wellesley College Whitin Observatory.
[a] Precision is computed as the rms of the residuals when the observed data points are subtracted from the transit and detrending model.

Table 4
Summary of High-resolution Imaging Observations

Target	Telescope	Instrument	Filter	Date	Image Type	Contrast
TOI-1937A	Gemini-S (8 m)	Zorro	562 nm	2020 Mar 13	Speckle	Δmag = 5.01 at 0.″5
⋯	Gemini-S (8 m)	Zorro	832 nm	2020 Mar 13	Speckle	Δmag = 5.97 at 0.″5
⋯	SOAR (4.1 m)	HRCam	I_c	2020 Dec 3	Speckle	Δmag = 4.6 at 1.″0
TOI-2364	SOAR (4.1 m)	HRCam	I_c	2020 Dec 3	Speckle	Δmag = 6.2 at 1.″0
⋯	Palomar (5 m)	PHARO	Brγ	2021 Feb 24	AO	Δmag = 6.791 at 0.″5
⋯	Gemini-S (8 m)	Zorro	562 nm	2021 Feb 27	Speckle	Δmag = 5.01 at 0.″5
⋯	Gemini-S (8 m)	Zorro	832 nm	2021 Feb 27	Speckle	Δmag = 6.2 at 0.″5
TOI-2583A	Shane (3 m)	ShARCS	J	2021 Jun 1	AO	⋯
⋯	Shane (3 m)	ShARCS	K_s	2021 Jun 1	AO	⋯
TOI-2587A	WIYN (3.5 m)	NESSI	562 nm	2021 Apr 24	Speckle	Δmag = 4.0 at 1.″0
⋯	WIYN (3.5 m)	NESSI	832 nm	2021 Apr 24	Speckle	Δmag = 5.1 at 1.″0
⋯	SOAR (4.1 m)	HRCam	I_c	2021 Nov 20	Speckle	Δmag = 6.6 at 1.″0
TOI-2796	SOAR (4.1 m)	HRCam	I_c	2021 Oct 18	Speckle	Δmag = 6.8 at 1.″0
TOI-2803A	SOAR (4.1 m)	HRCam	I_c	2021 Oct 1	Speckle	Δmag = 5.6 at 1.″0
TOI-2818	SOAR (4.1 m)	HRCam	I_c	2021 Oct 1	Speckle	Δmag = 6.8 at 1.″0
TOI-2842	SOAR (4.1 m)	HRCam	I_c	2021 Nov 20	Speckle	Δmag = 6.4 at 1.″0
TOI-2977	SOAR (4.1 m)	HRCam	I_c	2022 Mar 20	Speckle	Δmag = 5.7 at 1.″0
TOI-3023	SOAR (4.1 m)	HRCam	I_c	2022 Apr 15	Speckle	Δmag = 5.6 at 1.″0
TOI-3364	SOAR (4.1 m)	HRCam	I_c	2021 Nov 20	Speckle	Δmag = 7.1 at 1.″0
TOI-3688A	SAI-2.5 m (2.5 m)	Speckle Polarimeter	I_c	2021 Sep 9	Speckle	Δmag = 4.6 at 1.″0
TOI-3807	WIYN (3.5 m)	NESSI	832 nm	2022 Apr 17	Speckle	Δmag = 4.9 at 1.″0
TOI-3912	WIYN (3.5 m)	NESSI	832 nm	2022 Apr 18	Speckle	Δmag = 5.0 at 1.″0
TOI-3976A	WIYN (3.5 m)	NESSI	832 nm	2022 Apr 21	Speckle	Δmag = 5.2 at 1.″0
TOI-4087	WIYN (3.5 m)	NESSI	832 nm	2022 Apr 20	Speckle	Δmag = 4.6 at 1.″0
⋯	SAI-2.5 m (2.5 m)	Speckle Polarimeter	I_c	2022 May 13	Speckle	Δmag = 6.6 at 1.″0
TOI-4145A	SAI-2.5 m (2.5 m)	Speckle Polarimeter	I_c	2021 Oct 30	Speckle	Δmag = 5.1 at 1.″0
⋯	Gemini-N (8 m)	'Alopeke	562 nm	2022 Feb 15	Speckle	Δmag = 3.64 at 0.″5
⋯	Gemini-N (8 m)	'Alopeke	832 nm	2022 Feb 15	Speckle	Δmag = 5.25 at 0.″5
TOI-4463A	SAI-2.5 m (2.5 m)	Speckle Polarimeter	I_c	2021 Oct 22	Speckle	Δmag = 6.3 at 1.″0
⋯	SOAR (4.1 m)	HRCam	I_c	2022 Apr 15	Speckle	Δmag = 6.9 at 1.″0
⋯	WIYN (3.5 m)	NESSI	832 nm	2022 May 5	Speckle	Δmag = 5.5 at 1.″0
⋯	Palomar (5 m)	PHARO	Brγ	2022 May 21	AO	Δmag = 6.755 at 0.″5
⋯	Palomar (5 m)	PHARO	*H*cont	2022 May 21	AO	Δmag = 7.385 at 0.″5

`SImMER` pipeline (Savel et al. 2020).[62] These imaging observations are summarized in Table 4.

Nearby companions were detected in these high-resolution imaging observations only for the targets TOI-1937 (Figure 2), TOI-2583 (Figure 3), and TOI-2977 (Figure 4). The SOAR speckle imaging of TOI-1937 detected a companion at an angular separation of 2.″5 from the primary, which has $\Delta I = 4.3$ mag. The ShARCS imaging of TOI-2583 detected a companion at an angular separation of 5.″4 from the primary, with $\Delta J = 4.4$ mag and $\Delta K_s = 4.0$ mag. Finally, for the target TOI-2977, a fainter companion ($\Delta I_c = 1.7$ mag) at an angular separation of 0.″77 was revealed by the SOAR observations (Figure 4). We discuss the treatment of these companions in Section 3.2. No other companions were detected in the high angular resolution imaging down to the detection limits for the remaining targets, and we show these data in Figure 5.

[62] https://github.com/arjunsavel/SImMER

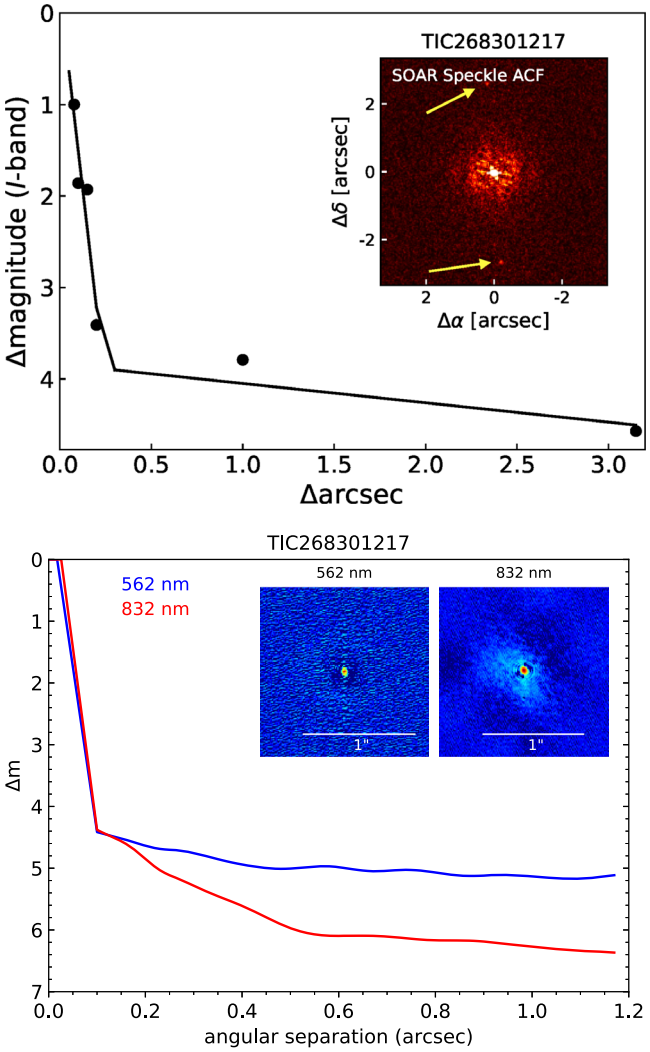

Figure 2. High-resolution imaging data for TOI-1937. Top: SOAR HRCam speckle sensitivity curve (solid line) and autocorrelation function (ACF, inset image). The detected companion appears as two dots $\approx 2\farcs5$ to the north and south of the primary (marked by yellow arrows). Bottom: Gemini-South Zorro 5σ sensitivity curve and reconstructed image (inset), taken at 562 nm and 832 nm. The field of view for these images is smaller than the separation of the $2\farcs5$ companion, and no further stars were detected down to instrumental detection limits.

2.5. High-resolution Spectroscopy

In order to confirm each planetary candidate and measure its mass, we obtained high-resolution spectroscopy of their host stars for the purpose of measuring precise relative RVs. We obtained 5–13 observations per target, scheduled primarily at orbital quadrature when possible, with the goal of obtaining at least a $\approx 4\sigma$ mass measurement of the planetary companion. These observations are summarized in Table 5, with the full table of extracted RVs provided in machine-readable form as supplementary material to this paper.

The instruments used for these observations were the Planet Finder Spectrograph (PFS) on the Magellan II Clay 6.5 m telescope (Crane et al. 2006, 2008, 2010); the High Resolution Echelle Spectrometer (HIRES; Vogt et al. 1994) on the Keck I 10 m telescope; the NEID spectrograph (Halverson et al. 2016; Schwab et al. 2016) on the WIYN 3.5 m telescope at Kitt Peak National Observatory (KPNO); the CTIO High Resolution Spectrometer (CHIRON; Tokovinin et al. 2013; Paredes et al. 2021) on the CTIO 1.5 m telescope; and the Tillinghast Reflector Echelle Spectrograph (TRES; Fűrész 2008) on the FLWO 1.5 m Tillinghast Reflector. Our observing strategy and data reduction procedures are detailed in Paper I, but we also describe them briefly here.

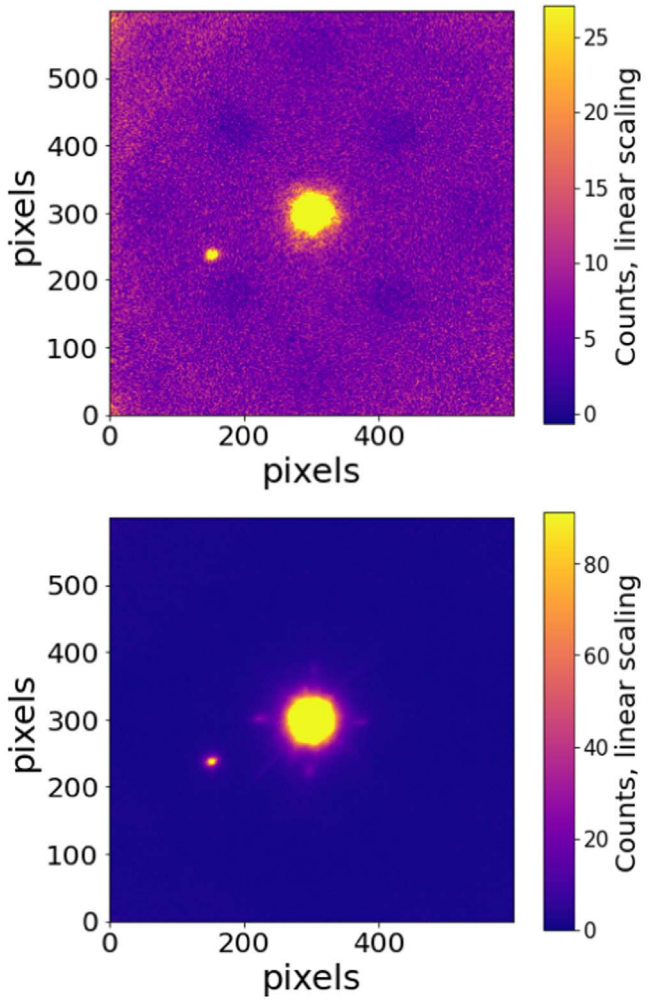

Figure 3. ShARCS AO imaging of TOI-2583, taken in J band (top) and K_s band (bottom), revealing a nearby companion at $\approx 5''$.

The HIRES spectra were observed through the queue organized by the California Planet Search (CPS; Howard et al. 2010; Howard & Fulton 2016)), using the standard CPS observing setup and data reduction procedures. We used the matched template technique from Dalba et al. (2020) to extract the RVs without the need for an expensive high signal-to-noise ratio (S/N) template, instead using an archival HIRES template spectrum matched to a low S/N reconnaissance observation of the target. This procedure increases the RV scatter by ≈ 4.7 m s^{-1}, which we added in quadrature to the instrumental uncertainties.

The NEID spectra were observed through the NEID queue in NEID's high-resolution (HR) mode. The data were reduced using v1.1.2–v1.1.4 of the standard NEID Data Reduction Pipeline (NEID-DRP),[63] which extracts RVs via cross correlation with a stellar line mask following procedures developed by Baranne et al. (1996) and Pepe et al. (2002). We note that the NEID data from the nights of 2022 May 9 and 2022 May 10 were affected

[63] https://neid.ipac.caltech.edu/docs/NEID-DRP

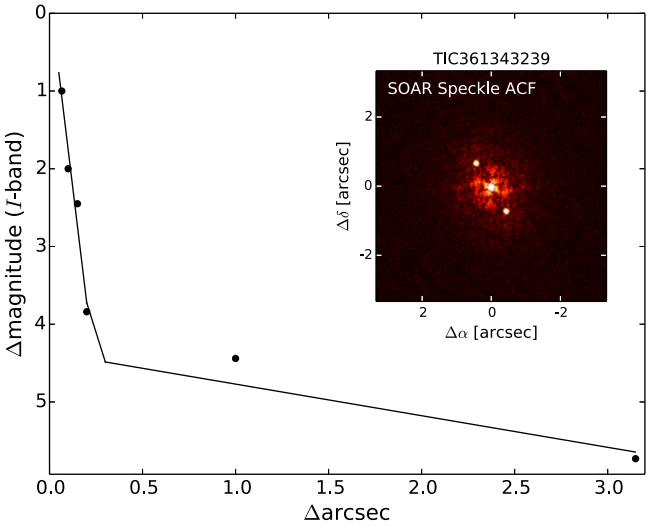

Figure 4. Speckle sensitivity curve (solid line) and ACF (inset image) from the SOAR HRCam observations of TOI-2977. In the ACF image, the two dots to the northwest and southeast of the center represent the detection of a stellar companion at $0\farcs77$ from the primary.

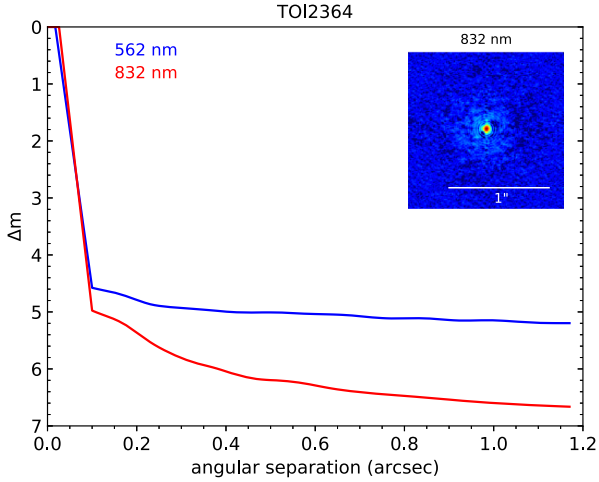

Figure 5. High-resolution imaging of hot Jupiter hosts without detected companions. The first figure shows the Gemini-South Zorro observation of TOI-2364. All imaging data used in this paper are available via ExoFoP (see footnote 59).

(The complete figure set (22 images) is available.)

by an RV drift due to the failure of the Fabry–Perot etalon laser used to calibrate nightly drifts. Using observations of standard stars taken on those nights, we estimated the offsets to be $35.8 \pm 1.2\,\mathrm{m\,s^{-1}}$ and $31.5 \pm 1.3\,\mathrm{m\,s^{-1}}$, respectively, and used these to correct one observation each of TOI-3807 and TOI-4087 taken on those nights.

The PFS observations were made in 3×3 binning mode with an iodine cell. An additional high S/N iodine-free template observation was obtained and used in the pipeline from Butler et al. (1996) to extract RVs.

The CHIRON spectra were taken using the echelle spectrograph with an image slicer and bracketed with calibration observations of a ThAr lamp. These spectra were reduced using the standard CHIRON pipeline, and RVs were extracted via least-squares deconvolution (Donati et al. 1997; Zhou et al. 2020). The TRES observations were reduced, and RVs were extracted using the pipeline described by Buchhave et al. (2010) and Quinn et al. (2012).

For the PFS, HIRES, NEID, and CHIRON spectra, we also used the procedures from Hartman et al. (2019) to measure bisector inverse slopes (BIS) from the iodine-free orders. These measurements were used to check for spurious RV variations that are actually due to variations in the spectral line profiles, rather than orbital motion. For all the systems presented here, we did not observe any significant correlations between the RVs and BIS measurements.

2.6. Catalog Photometry and Astrometry

To ensure we have a complete view of each planetary system, we used the `astroquery` package (Ginsburg et al. 2019) to gather information about each target from the literature. We obtained photometric and astrometric observations from the TESS Input Catalog (TIC; Stassun et al. 2018, 2019), Gaia DR3 (Brown et al. 2021; Lindegren et al. 2021; Riello et al. 2021), 2MASS (Cutri et al. 2003; Skrutskie et al. 2006), WISE (Cutri 2012), and Tycho-2 (Høg et al. 2000) catalogs. We corrected the Gaia photometry for the known parallax zero-point error as described in Lindegren et al. (2021).[64] These data are shown in Table 6.

2.7. Rossiter–McLaughlin Effect of TOI-1937

We observed a transit of TOI-1937A b on the night of 2020 December 29 both spectroscopically and photometrically, in order to measure the projected stellar obliquity through the Rossiter–McLaughlin (RM; McLaughlin 1924; Rossiter 1924) effect. The photometric observations were acquired from El Sauce, and the spectroscopy was acquired using Magellan/PFS. The photometric results are shown in Figure 15, with the transit occurring at the expected time. The PFS observations were made in the same manner as described in Section 2.5, with 13 exposures of 12 minutes each, covering the full transit duration.

The resulting velocities are shown as a function of time in Figure 6. The expected RM anomaly has an amplitude $\Delta v_{\mathrm{RM}} \approx \delta \cdot v \sin i \cdot \sqrt{1 - b^2} \approx 52\,\mathrm{m\,s^{-1}}$, which agrees visually with the data. We therefore fitted the RVs using the Hirano et al. (2010, 2011) models for the RM effect. We assumed a Gaussian prior on $v \sin i$ and $a/R_\star$ from Table 7 and also allowed for a white noise jitter term to be added in quadrature to the measurement uncertainties. We fixed the limb darkening using the V-band tabulation from Claret & Bloemen (2011). We then varied the sky-projected obliquity, the projected stellar equatorial velocity, and the Gaussian dispersion of the spectral lines, along with a linear trend accounting for the out-of-transit variability. Given that the TESS light curves (Figure 9) show photometric variability only at the level of ∼1%, with no evidence of spot-crossing events in the simultaneous transit photometry, we did not account for starspot-induced variability in the RM model (e.g., Oshagh et al. 2013, 2018).

The model shown in Figure 6 suggests a good fit to the data for a model that has a projected stellar obliquity that is well aligned with the orbit of TOI-1937A b: $\lambda = 4\fdg0 \pm 3\fdg5$.

[64] https://gitlab.com/icc-ub/public/gaiadr3_zeropoint

Table 5
Summary of RV Measurements

Target	Instrument	N_{obs}	Median σ_{RV} (m s^{-1})[a]	First Observation Date (UT)	Last Observation Date (UT)
TOI-1937A	Magellan-Clay/PFS	13	8.5	2020 Feb 4	2020 Nov 4
TOI-2364	Magellan-Clay/PFS	6	3.2	2021 Oct 19	2022 Jan 23
…	FLWO/TRES	4	38.1	2017 Dec 22	2019 Oct 31
TOI-2583A	Keck I/HIRES	6	6.5	2021 Oct 10	2022 Jun 11
…	FLWO/TRES	2	44.5	2021 Mar 22	2021 Mar 29
TOI-2587A	WIYN/NEID	10	6.7	2021 Nov 10	2022 Apr 22
…	FLWO/TRES	2	35.9	2021 Apr 23	2021 May 7
TOI-2796	Keck I/HIRES	3	5.5	2021 Nov 24	2022 Jan 8
…	WIYN/NEID	7	8.8	2021 Dec 6	2022 Jan 4
…	FLWO/TRES	2	48.9	2021 Oct 1	2021 Oct 13
TOI-2803A	Magellan-Clay/PFS	6	6.0	2022 Jan 13	2022 Mar 24
…	FLWO/TRES	3	87.8	2021 Nov 11	2021 Nov 14
TOI-2818	CTIO-1.5 m/CHIRON	7	27.0	2021 Dec 21	2022 Mar 15
TOI-2842	Magellan-Clay/PFS	6	6.8	2022 Jan 13	2022 Mar 25
…	FLWO/TRES	2	51.4	2021 Nov 2	2021 Nov 11
TOI-2977	CTIO-1.5 m/CHIRON	6	33.5	2022 Mar 24	2022 May 22
TOI-3023	Magellan-Clay/PFS	6	5.0	2022 Jan 21	2022 Jun 19
TOI-3364	Magellan-Clay/PFS	6	2.3	2022 Jan 13	2022 Mar 22
TOI-3688A	WIYN/NEID	7	11.3	2021 Nov 28	2022 Jan 10
…	FLWO/TRES	2	47.9	2021 Sep 18	2021 Oct 9
TOI-3807	WIYN/NEID	5	9.4	2022 Mar 7	2022 Jun 7
…	FLWO/TRES	2	31.2	2021 Nov 29	2021 Dec 9
TOI-3819	WIYN/NEID	6	11.4	2021 Dec 13	2022 Jan 7
…	FLWO/TRES	2	39.0	2021 Nov 11	2021 Nov 19
TOI-3912	Keck I/HIRES	7	5.7	2022 Apr 21	2022 May 30
…	FLWO/TRES	2	33.8	2022 Feb 11	2022 Feb 16
TOI-3976A	Keck I/HIRES	12	6.0	2022 Apr 21	2022 Aug 1
…	FLWO/TRES	2	32.0	2022 Jan 31	2022 Feb 16
TOI-4087	WIYN/NEID	7	14.2	2022 May 9	2022 Jun 7
…	FLWO/TRES	8	34.7	2022 Feb 6	2022 Jun 14
TOI-4145A	WIYN/NEID	8	7.2	2021 Nov 28	2022 Mar 18
…	FLWO/TRES	2	34.4	2021 Sep 20	2021 Sep 22
TOI-4463A	WIYN/NEID	6	3.9	2022 Mar 7	2022 Jun 1
…	FLWO/TRES	2	27.5	2021 Sep 16	2021 Sep 29
TOI-4791	CTIO-1.5 m/CHIRON	6	52.0	2022 Mar 16	2022 Mar 26
…	FLWO/TRES	2	47.5	2022 Jan 10	2022 Feb 7

Notes. The complete table of RV measurements is available in machine-readable form as data behind the figure for Figure 15, provided as relative RVs with an arbitrary target- and instrument-specific offset subtracted.
[a] Median instrumental RV uncertainty for each target and instrument.

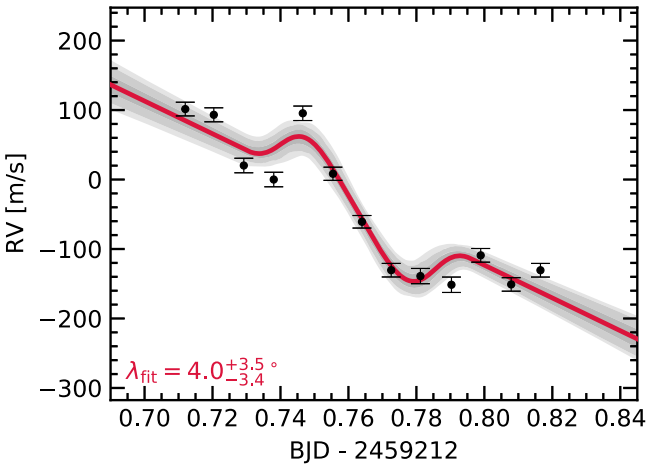

Figure 6. RVs of TOI-1937A from the night of 2020 December 29. The best-fit model of the RM effect is shown in red, with the corresponding 1σ, 2σ, and 3σ uncertainties in gray.

3. Stellar Characterization

3.1. Spectroscopic Parameters

We used the high-resolution spectra of each target to perform an initial characterization of the stellar properties of these planet hosts.

For stars with observations from TRES, spectroscopic atmospheric properties were derived using the Stellar Parameter Classification code (SPC; Buchhave et al. 2012), which cross-correlates the observed spectrum against a grid of synthetic spectra from Kurucz (1993). We classified each observation of the same target separately, adopting the median value in each parameter and using the scatter in the results as the uncertainty, with an error floor of 50 K in T_{eff}, 0.1 dex in $\log g$, 0.08 dex in [Fe/H], and 0.5 km s^{-1} in $v \sin i$. The CHIRON spectra were analyzed by matching against a library of ∼10,000 observed spectra that were previously classified using SPC, as described by Zhou et al. (2020). As we did for the TRES observations, we adopted the median value and scatter of the results derived from

Table 6
Catalog Photometry and Astrometry of Planet Host Stars

Target	TOI-1937	TOI-2364	TOI-2583	TOI-2587	TOI-2796	Source
Identifiers						
TIC	268301217	39414571	7548817	68007716	220076110	
Gaia DR3	5489726768531119616	3022644120017418496	2115776451371641984	3085216850017388672	3222453935725951488	
2MASS	07452898-5222599	05563119-0500430	18090407 + 4520127	07434358-0104235	05363665 + 0053466	
Tycho-2	…	…	…	4831-01170-1	…	
WISE	J074528.97-522259.6	J055631.19-050043.2	J180904.08 + 452012.7	J074343.60-010423.9	J053636.65 + 005346.5	
Astrometric Measurements						
R.A. (J2000)	07:45:28.973	05:56:31.207	18:09:04.087	07:43:43.611	05:36:36.653	1
Decl. (J2000)	−52:22:59.73	−05:00:43.31	+45:20:12.84	−01:04:24.01	+00:53:46.61	1
μ_α (mas yr^{-1})	−5.627 ± 0.013	12.225 ± 0.019	7.831 ± 0.011	22.004 ± 0.023	2.537 ± 0.018	1
μ_δ (mas yr^{-1})	11.309 ± 0.013	−15.462 ± 0.015	4.991 ± 0.012	−25.296 ± 0.019	2.635 ± 0.012	1
Parallax (mas)	2.389 ± 0.011	4.574 ± 0.019	1.781 ± 0.009	2.626 ± 0.022	2.838 ± 0.015	1
b (deg)	−13.549	−14.493	26.060	11.112	−16.157	1
l (deg)	265.308	211.153	72.654	219.944	203.334	1
Photometric Measurements						
T (mag)	12.493 ± 0.006	11.552 ± 0.006	12.045 ± 0.007	10.966 ± 0.006	11.916 ± 0.022	2
G (mag)	13.005 ± 0.003	12.082 ± 0.003	12.453 ± 0.003	11.405 ± 0.003	12.353 ± 0.003	1
G_{BP} (mag)	13.417 ± 0.003	12.511 ± 0.003	12.759 ± 0.003	11.738 ± 0.003	12.695 ± 0.003	1
G_{RP} (mag)	12.421 ± 0.004	11.488 ± 0.004	11.983 ± 0.004	10.909 ± 0.004	11.851 ± 0.004	1
B_T (mag)	…	…	…	12.263 ± 0.226	…	3
V_T (mag)	…	…	…	11.612 ± 0.173	…	3
J (mag)	11.717 ± 0.029[a]	10.909 ± 0.024	…	10.354 ± 0.023	11.286 ± 0.022	4
H (mag)	11.324 ± 0.026[a]	10.436 ± 0.022	11.192 ± 0.020	10.079 ± 0.023	10.976 ± 0.022	4
K_s (mag)	11.226 ± 0.021[a]	10.363 ± 0.021	…	9.991 ± 0.023	10.936 ± 0.023	4
W1 (mag)	11.135 ± 0.023[a]	10.290 ± 0.022	11.082 ± 0.023[b]	9.954 ± 0.022	10.885 ± 0.023	5
W2 (mag)	11.155 ± 0.020[a]	10.362 ± 0.020	11.112 ± 0.021[b]	9.998 ± 0.019	10.942 ± 0.021	5
W3 (mag)	11.160 ± 0.086[a]	10.657 ± 0.105	11.015 ± 0.088[b]	9.940 ± 0.060	10.840 ± 0.127	5

Target	TOI-2803	TOI-2818	TOI-2842	TOI-2977[c]	TOI-3023	Source
Identifiers						
TIC	124379043	151483286	178162579	361343239	454248975	
Gaia DR3	2913482170369046656	5545555570947605376	3046327742219111808	5305241494923209856	5227928170880093568	
2MASS	06122753-2329331	07561435-3507000	07121060-1038217	09354239-6021271	11011602-7221246	
Tycho-2	…	…	…	…	…	
WISE	J061227.53-232933.0	J075614.35-350700.1	J071210.60-103821.6	J093542.37-602126.9	J110115.86-722124.2	
Astrometric Measurements						
R.A. (J2000)	06:12:27.538	07:56:14.356	07:12:10.610	09:35:42.363	11:01:15.790	1
Decl. (J2000)	−23:29:32.98	−35:07:00.16	−10:38:21.62	−60:21:26.90	−72:21:24.12	1
μ_α (mas yr^{-1})	0.749 ± 0.009	−6.034 ± 0.010	3.268 ± 0.013	−21.720 ± 0.118	−66.732 ± 0.011	1
μ_δ (mas yr^{-1})	11.908 ± 0.011	−8.990 ± 0.012	4.195 ± 0.014	20.892 ± 0.108	25.773 ± 0.011	1
Parallax (mas)	1.997 ± 0.012	3.170 ± 0.010	2.174 ± 0.013	2.919 ± 0.094	2.546 ± 0.009	1
b (deg)	−18.658	−3.394	−0.295	−6.150	−11.266	1
l (deg)	230.374	251.037	224.751	280.905	294.716	1
Photometric Measurements						
T (mag)	12.075 ± 0.006	11.394 ± 0.006	12.033 ± 0.006	11.938 ± 0.007	11.485 ± 0.006	2
G (mag)	12.417 ± 0.003	11.830 ± 0.003	12.455 ± 0.003	12.492 ± 0.003	12.028 ± 0.003	1
G_{BP} (mag)	12.669 ± 0.003	12.166 ± 0.003	12.778 ± 0.003	12.748 ± 0.003	12.464 ± 0.003	1
G_{RP} (mag)	12.006 ± 0.004	11.329 ± 0.004	11.970 ± 0.004	11.791 ± 0.005	11.420 ± 0.004	1
B_T (mag)	…	…	…	…	…	3
V_T (mag)	…	…	…	…	…	3
J (mag)	11.607 ± 0.024	10.743 ± 0.027	11.410 ± 0.024	11.128 ± 0.026	10.680 ± 0.024	4
H (mag)	11.355 ± 0.026	10.454 ± 0.026	11.152 ± 0.023	10.776 ± 0.026	10.312 ± 0.023	4
K_s (mag)	11.282 ± 0.025	10.403 ± 0.025	11.062 ± 0.019	10.666 ± 0.026	10.243 ± 0.023	4
W1 (mag)	11.201 ± 0.023	10.329 ± 0.022	11.050 ± 0.023	10.610 ± 0.023	10.159 ± 0.022	5
W2 (mag)	11.243 ± 0.021	10.374 ± 0.020	11.101 ± 0.022	10.651 ± 0.021	10.189 ± 0.020	5
W3 (mag)	11.255 ± 0.129	10.199 ± 0.053	11.247 ± 0.146	10.641 ± 0.104	9.986 ± 0.033	5

Target	TOI-3364	TOI-3688	TOI-3807	TOI-3819	TOI-3912	Source
Identifiers						
TIC	280655495	245509452	289661991	95660472	156648452	
Gaia DR3	5409268527708808320	4541879811886471 68	1117620107545810944	8766082926084165 12	1255520718461480960	
2MASS	09380910-4920069	02370772 + 5451046	09162700 + 6904269	08072719 + 2923194	14231236 + 2404357	
Tycho-2	8176-00923-1	3691-01688-1	4376-00887-1	…	…	
WISE	J093809.09-492006.7	J023707.74 + 545104.7	J091627.00 + 690426.8	J080727.18 + 292319.2	J142312.36 + 240435.5	
Astrometric Measurements						
R.A. (J2000)	09:38:09.064	02:37:07.762	09:16:27.016	08:07:27.181	14:23:12.359	1
Decl. (J2000)	−49:20:06.79	+54:51:04.37	+69:04:26.86	+29:23:19.11	+24:04:35.63	1
μ_α (mas yr^{-1})	−26.417 ± 0.014	18.777 ± 0.009	−0.654 ± 0.009	−6.144 ± 0.015	7.746 ± 0.011	1
μ_δ (mas yr^{-1})	14.037 ± 0.013	−11.398 ± 0.013	−1.238 ± 0.010	−22.673 ± 0.012	−0.364 ± 0.012	1
Parallax (mas)	3.628 ± 0.013	2.494 ± 0.011	2.327 ± 0.011	1.779 ± 0.016	2.128 ± 0.013	1

Table 6
(Continued)

Target	TOI-3364	TOI-3688	TOI-3807	TOI-3819	TOI-3912	Source
b (deg)	2.278	−4.934	37.871	28.443	69.117	1
l (deg)	273.783	137.832	144.331	192.471	29.666	1
Photometric Measurements						
T (mag)	10.814 ± 0.006	11.843 ± 0.013	11.582 ± 0.007	11.982 ± 0.009	11.875 ± 0.007	2
G (mag)	11.293 ± 0.003	12.357 ± 0.003	12.025 ± 0.003	12.404 ± 0.003	12.298 ± 0.003	1
G_{BP} (mag)	11.664 ± 0.003	12.772 ± 0.003	12.368 ± 0.003	12.727 ± 0.003	12.624 ± 0.003	1
G_{RP} (mag)	10.760 ± 0.004	11.776 ± 0.004	11.520 ± 0.004	11.921 ± 0.004	11.812 ± 0.004	1
B_T (mag)	12.422 ± 0.193	13.075 ± 0.272	12.986 ± 0.207	…	…	3
V_T (mag)	11.929 ± 0.171	12.318 ± 0.188	11.956 ± 0.133	…	…	3
J (mag)	10.156 ± 0.022	11.129 ± 0.026	10.956 ± 0.027	11.398 ± 0.020	11.270 ± 0.021	4
H (mag)	9.876 ± 0.022	10.819 ± 0.024	10.634 ± 0.030	11.143 ± 0.019	11.016 ± 0.019	4
K_s (mag)	9.783 ± 0.019	10.732 ± 0.020	10.617 ± 0.019	11.077 ± 0.017	10.922 ± 0.018	4
W1 (mag)	9.691 ± 0.023	10.125 ± 0.122	10.591 ± 0.022	11.033 ± 0.022	10.898 ± 0.023	5
W2 (mag)	9.729 ± 0.020	10.662 ± 0.021	10.644 ± 0.021	11.078 ± 0.022	10.931 ± 0.019	5
W3 (mag)	9.593 ± 0.037	10.656 ± 0.101	10.591 ± 0.073	10.827 ± 0.120	10.858 ± 0.081	5

Target	TOI-3976	TOI-4087	TOI-4145	TOI-4463	TOI-4791	Source
Identifiers						
TIC	154293917	310002617	279947414	8599009	100389539	
Gaia DR3	1585783740516554624	1725490333641502976	568619413331898240	4524517290642206336	2930141657016297216	
2MASS	14572548 + 4416274	14314234 + 8322215	02374306 + 8016028	18372595 + 1843470	07173322-1949443	
Tycho-2	…	4634-01080-1	4503-00293-1	1574-00343-1	5973-02018-1	
WISE	J145725.44 + 441627.4	J143142.22 + 832221.7	J023743.14 + 801602.6	J183725.95 + 184347.5	J071733.21-194944.2	
Astrometric Measurements						
R.A. (J2000)	14:57:25.441	14:31:42.182	02:37:43.141	18:37:25.951	07:17:33.211	1
Decl. (J2000)	+44:16:27.57	+83:22:21.75	+80:16:02.57	+18:43:47.85	−19:49:44.18	1
μ_α (mas yr^{-1})	−19.831 ± 0.008	−16.514 ± 0.014	11.694 ± 0.010	−5.157 ± 0.017	−14.195 ± 0.018	1
μ_δ (mas yr^{-1})	10.118 ± 0.011	10.456 ± 0.014	−13.534 ± 0.011	50.619 ± 0.017	6.098 ± 0.018	1
Parallax (mas)	1.914 ± 0.009	3.220 ± 0.011	4.879 ± 0.010	5.628 ± 0.018	3.104 ± 0.018	1
b (deg)	59.505	33.091	18.352	11.414	−3.410	1
l (deg)	75.443	119.586	127.501	48.278	233.498	1
Photometric Measurements						
T (mag)	11.814 ± 0.007	11.296 ± 0.027	11.524 ± 0.006	10.467 ± 0.006	10.896 ± 0.006	2
G (mag)	12.211 ± 0.003	11.701 ± 0.003	12.049 ± 0.003	10.951 ± 0.003	11.313 ± 0.003	1
G_{BP} (mag)	12.511 ± 0.003	12.007 ± 0.003	12.472 ± 0.003	11.324 ± 0.003	11.624 ± 0.003	1
G_{RP} (mag)	11.751 ± 0.004	11.235 ± 0.004	11.463 ± 0.004	10.411 ± 0.004	10.836 ± 0.004	1
B_T (mag)	…	12.509 ± 0.167	13.152 ± 0.263	11.778 ± 0.066	11.908 ± 0.086	3
V_T (mag)	…	12.148 ± 0.156	12.179 ± 0.160	11.106 ± 0.066	11.579 ± 0.102	3
J (mag)	11.238 ± 0.021	10.754 ± 0.022	10.775 ± 0.023	9.802 ± 0.021	10.319 ± 0.026	4
H (mag)	10.960 ± 0.018	10.493 ± 0.029	10.380 ± 0.028	9.454 ± 0.018	10.108 ± 0.023	4
K_s (mag)	…	10.436 ± 0.025	10.286 ± 0.021	9.402 ± 0.015	10.019 ± 0.023	4
W1 (mag)	10.883 ± 0.023	10.390 ± 0.023	10.198 ± 0.023	9.343 ± 0.023	9.959 ± 0.023	5
W2 (mag)	10.904 ± 0.021	10.432 ± 0.019	10.251 ± 0.020	9.393 ± 0.021	9.990 ± 0.020	5
W3 (mag)	10.869 ± 0.068	10.381 ± 0.047	10.216 ± 0.059	9.397 ± 0.036	10.030 ± 0.050	5

Notes. The catalog photometry presented here has not been corrected for contamination by nearby stellar companions (Section 3.2).
[a] The 2MASS and WISE photometry of TOI-1937 are a blend of both the primary and secondary components (Section 3.2).
[b] The WISE photometry of TOI-2583 is a blend of both the primary and secondary components.
[c] All catalog photometry of TOI-2977 is a blend of both the primary and secondary components.
Sources: (1) Gaia DR3 (Brown et al. 2021); (2) TESS Input Catalog (Stassun et al. 2019); (3) Tycho-2 (Høg et al. 2000); (4) 2MASS (Cutri et al. 2003; Skrutskie et al. 2006); (5) WISE (Cutri 2012).

the spectra of the same target, with error floors of 50 K in $T_{\rm eff}$, 0.1 dex in $\log g$, 0.1 dex in [Fe/H], and 0.5 km s^{-1} in $v \sin i$.

Because not all of our targets have spectra from TRES or CHIRON, we used the `SpecMatch-Emp` code (Yee et al. 2017)[65] to derive spectroscopic parameters for all our targets, using the highest S/N iodine-free spectrum from PFS, HIRES, NEID, or CHIRON per object. This code matches the target spectrum to a library of observed Keck/HIRES spectra from stars with empirically well-determined stellar properties, yielding $T_{\rm eff}$, $R_\star$, and [Fe/H] for the target with median uncertainties of $\sigma(T_{\rm eff}) = 110$ K, $\sigma(\Delta R_\star/R_\star) = 15\%$, and σ([Fe/H]) = 0.09 dex, as derived from a cross-validation test. To derive $v \sin i$, we used `SpecMatch-Synth`[66] (Petigura 2015), which performs a similar matching procedure using the Kurucz (1993) synthetic spectral library. We combined the $v \sin i$ and macroturbulent velocity $v_{\rm mac}$ (assumed using the relationship

[65] https://github.com/samuelyeewl/specmatch-emp
[66] https://github.com/petigura/specmatch-syn

with stellar $T_{\rm eff}$ from Valenti & Fischer 2005) from this code together with $T_{\rm eff}$, $R_\star$, and [Fe/H] from SpecMatch-Emp, reporting these in Table 8.

We decided to adopt the SpecMatch spectroscopic parameters for the rest of our analysis, using them as priors for our global EXOFASTv2 fits, since we could apply the same code homogeneously to all our targets. We compared the SpecMatch-derived parameters with those from SPC when available and found agreement in almost all cases to better than 2σ.

3.1.1. Iterative Solution for TOI-2803

The case with the largest discrepancy was for TOI-2803, where SpecMatch-Emp reported $[{\rm Fe/H}] = -0.43 \pm 0.09$ dex based on the PFS template spectrum, whereas SPC reported a metallicity of -0.11 ± 0.10 dex based on two TRES spectra. Furthermore, the spectroscopic stellar $T_{\rm eff}$, $\log g$, and $R_\star$ also differed from the results derived from the global EXOFASTv2 fits (Section 4). The global fits provide better constraints on the stellar surface gravity ($\log g$) from the measured transit duration (Seager & Mallen-Ornelas 2003), as well as on the stellar $T_{\rm eff}$ based on the Gaia parallaxes and measured SED.

To resolve the discrepancy and arrive at a self-consistent solution, an iterative approach was required. First, we fixed $\log g = 4.3$ dex (based on the fits to the transit light curve) in the SPC analysis of the TRES spectrum. We also performed a new analysis of the PFS spectrum using the Zonal Atmospheric Stellar Parameters Estimator (ZASPE; Brahm et al. 2017) code, also holding $\log g$ fixed. ZASPE derives spectroscopic parameters using only the most sensitive spectral regions to compare the target with a grid of spectra computed with the SPECTRUM spectral synthesis program (Gray 1999) and the ATLAS model atmospheres (Castelli & Kurucz 2003). The results from these analyses are included in Table 8. We then used only the spectroscopic metallicities as priors in two separate global EXOFASTv2 fits.

The global fit returned $T_{\rm eff} = 6280 \pm 100$ K, $\log g = 4.30 \pm 0.01$ dex, $[{\rm Fe/H}] = -0.11 \pm 0.07$ dex when the SPC TRES metallicity prior was used ($[{\rm Fe/H}] = -0.11 \pm 0.08$ dex). Meanwhile, when the ZASPE PFS metallicity prior was used ($[{\rm Fe/H}] = -0.35 \pm 0.07$ dex), the global EXOFASTv2 fit required a hotter star ($T_{\rm eff} = 6436 \pm 80$ K) than was found by the spectroscopic analysis ($T_{\rm eff} = 6341 \pm 122$ K). Given that the results were most self-consistent when using the SPC TRES metallicity, we chose to adopt that set of stellar properties.

3.2. Stars with Nearby Companions

3.2.1. Gaia-detected Companions

We investigated the stellar multiplicity of the 20 planet host stars by querying the Gaia DR3 catalog (Gaia Collaboration et al. 2022) for nearby stars within 30″ with similar proper motions to the planet host. Eight of our targets were found to have such companions, with angular separations between 1.″7 and 20″ away and are listed in Table 9. We also crossmatched our sample with the catalog of wide binaries from El-Badry et al. (2021), who computed the probabilities that each potential binary pair is due to a chance alignment, given their parallaxes, projected separation, and requiring that their proper motions are consistent with a Keplerian orbit. All eight binary pairs we identified were also listed in the El-Badry et al. (2021) catalog, with chance alignment probabilities $<3 \times 10^{-3}$, suggesting that they are bound. In each case, the planet host star was the brighter of the two; as such, we refer to them subsequently as the "A" component.

For these eight cases, the secondary component was also identified in the TIC; hence any dilution of the TESS light curve due to their light would have already been accounted for. In the cases of TOI-1937 and TOI-4145, the secondaries were located 2.″48 and 1.″74 from the primary, respectively, and would have contaminated the ground-based light curves. We therefore computed a dilution factor for each band using the SED-fitting procedures described in Section 3.2.2 to correct the light curves for these targets.

3.2.2. Companions from High-resolution Imaging

For the majority of targets described in this paper, high-resolution imaging did not detect any stellar companions (Figure 5).

The SOAR HRCam speckle imaging of the target TOI-2977 (Section 2.4, Figure 4) revealed a nearby star 1.7 magnitudes fainter in the I_c band located 0.″77 away from the primary. This star was not identified in the Gaia DR3 catalog (Gaia Collaboration et al. 2022).[67] Although we did not detect any lines of this nearby star in our spectroscopic observations, we need to correct the broadband catalog and time-series photometry for contamination by this nearby star.

We used the same procedures as described in Paper I to perform this correction. Briefly, we fitted the catalog photometry from Gaia, 2MASS, and WISE, as well as the Δmag measured by SOAR HRCam, with a blended two-component model of the SED using the isochrones package (Morton 2015; Dotter 2016; Choi et al. 2016). We made the assumption that the two stars are physically associated and have the same parallax as measured for the primary by Gaia, as is the case for most stars separated by $<1''$ (Horch et al. 2014; Matson et al. 2018). We determined an upper limit on the line-of-sight extinction from the dust maps of Schlegel et al. (1998) and Schlafly & Finkbeiner (2011). Priors were placed on the spectroscopic properties of the primary from those derived by the SpecMatch-Emp analysis (Section 3.1). We imposed an error floor of 0.02 mag for the Gaia and 2MASS photometry and 0.03 mag for the WISE photometry.

We plot the best-fit SED model in the top panel of Figure 7 and present the stellar properties of the primary and secondary components in Table 10. If the two components are indeed bound, TOI-2977B is a mid-K dwarf with a sky-projected separation of $\approx$260 au from the primary. We subtracted the model fluxes of the secondary from the observed catalog fluxes and also used them to compute dilution factors for the TESS and ground-based time-series photometry. These corrected fluxes and dilution factors were then included in our global modeling of the TOI-2977 system (Section 4).

Apart from the TOI-2977 system, the high-resolution imaging observations detected companions for TOI-1937 and TOI-2583, which were also identified by Gaia (Table 9). For TOI-1937, SOAR speckle imaging detected the nearby star at a separation of 2.″5 and $\Delta I = 4.3$ mag (Figure 2). Similarly for TOI-2583, the ShARCS AO imaging detected the companion

[67] Gaia DR3 did identify a faint star about 2.″4 away and $\approx$6.25 mag fainter than the primary in the Gaia G band, which we neglect in the remainder of our analysis due to its faintness.

Table 7
Median Values and 68% Confidence Intervals for Fitted Stellar and Planetary Parameters

		TOI-1937 b	TOI-2364 b	TOI-2583 b	TOI-2587 b	TOI-2796 b
Planet Parameters						
P (days)	Period	$0.94667944 \pm 0.00000047$	4.0197517 ± 0.0000043	4.5207265 ± 0.0000049	5.456640 ± 0.000011	$4.8084983^{+0.0000057}_{-0.0000056}$
T_c (BJD_{TDB})	Time of conjunction	$2{,}459{,}085.91023 \pm 0.00012$	$2{,}459{,}058.21396 \pm 0.00033$	$2{,}459{,}216.01039 \pm 0.00036$	$2{,}458{,}950.09242 \pm 0.00076$	$2{,}459{,}026.48882 \pm 0.00045$
T_{14} (days)	Transit duration	0.05737 ± 0.00057	$0.11563^{+0.00097}_{-0.00093}$	$0.1836^{+0.0013}_{-0.0012}$	0.1734 ± 0.0023	0.0818 ± 0.0017
τ (days)	Ingress/egress duration	$0.0220^{+0.0014}_{-0.0012}$	$0.00988^{+0.00066}_{-0.00040}$	$0.0163^{+0.0013}_{-0.0010}$	$0.0204^{+0.0020}_{-0.0021}$	$0.04089^{+0.00087}_{-0.00083}$
$a/R_\star$	Planet–star separation	$3.85^{+0.09}_{-0.10}$	$11.84^{+0.22}_{-0.33}$	$8.31^{+0.23}_{-0.27}$	$7.92^{+0.38}_{-0.30}$	$11.43^{+0.33}_{-0.30}$
$(R_P/R_\star)^2$	Transit depth	0.0141 ± 0.0016	$0.00794^{+0.00016}_{-0.00015}$	$0.00806^{+0.00015}_{-0.00014}$	0.00411 ± 0.00013	0.0234 (>0.0224)
i (deg)	Inclination	$77.00^{+0.44}_{-0.49}$	$88.98^{+0.62}_{-0.54}$	$88.16^{+0.98}_{-0.76}$	$84.81^{+0.49}_{-0.40}$	84.90 (<85.22)
K ($m\ s^{-1}$)	RV semiamplitude	386 ± 28	$29.7^{+5.6}_{-6.4}$	27.1 ± 6.1	$22.7^{+5.4}_{-4.7}$	50^{+11}_{-12}
a (au)	Semimajor axis	$0.01932^{+0.00035}_{-0.00039}$	$0.04871^{+0.00069}_{-0.00079}$	$0.0571^{+0.0010}_{-0.0013}$	$0.0635^{+0.0025}_{-0.0013}$	$0.0569^{+0.0010}_{-0.0011}$
R_P (R_J)	Planet radius	$1.247^{+0.059}_{-0.062}$	$0.768^{+0.023}_{-0.018}$	$1.290^{+0.040}_{-0.033}$	$1.077^{+0.042}_{-0.040}$	1.59 (>1.54)
M_P (M_J)	Planet mass	$2.01^{+0.17}_{-0.16}$	$0.225^{+0.043}_{-0.049}$	$0.250^{+0.058}_{-0.056}$	$0.218^{+0.054}_{-0.046}$	$0.44^{+0.10}_{-0.11}$
ρ_P ($g\ cm^{-3}$)	Planet density	$1.28^{+0.21}_{-0.17}$	$0.61^{+0.13}_{-0.14}$	$0.144^{+0.037}_{-0.035}$	$0.216^{+0.064}_{-0.052}$	0.03 (<0.15)
$\log g_P$ (cgs)	Planet surface gravity	$3.506^{+0.047}_{-0.048}$	$2.97^{+0.08}_{-0.11}$	$2.57^{+0.09}_{-0.11}$	2.67 ± 0.11	2.39 (<2.67)
$b \equiv a \cos i/R_\star$	Transit impact parameter	$0.8653^{+0.0086}_{-0.0084}$	$0.21^{+0.10}_{-0.13}$	$0.27^{+0.10}_{-0.14}$	$0.716^{+0.027}_{-0.036}$	1.00 (>0.97)
e	Eccentricity	0.0 (fixed)	0.0 (fixed)	0.0 (fixed)	0.0 (fixed)	0.0 (fixed)
e_{lim}[a]	1σ upper limit on eccentricity	<0.034	<0.067	<0.089	<0.171	<0.172
τ_{circ} (Gyr)[b]	Tidal circularization timescale	$0.00168^{+0.00042}_{-0.00033}$	1.02 ± 0.26	$0.166^{+0.051}_{-0.046}$	$0.78^{+0.31}_{-0.23}$	0.010 (<0.144)
$\langle F \rangle$ ($Gerg\ s^{-1}\ cm^{-2}$)	Incident flux	$4.39^{+0.30}_{-0.29}$	$0.322^{+0.020}_{-0.016}$	$1.022^{+0.054}_{-0.044}$	$0.991^{+0.066}_{-0.069}$	$0.479^{+0.029}_{-0.027}$
T_{eq} (K)	Planet equilibirum temperature	2097^{+35}_{-36}	1091^{+17}_{-14}	1456^{+19}_{-16}	1445^{+23}_{-26}	1205^{+18}_{-17}
Stellar Parameters						
$M_\star$ ($M_\odot$)	Stellar mass	$1.072^{+0.059}_{-0.064}$	$0.954^{+0.041}_{-0.046}$	$1.215^{+0.063}_{-0.082}$	$1.15^{+0.14}_{-0.07}$	$1.063^{+0.057}_{-0.062}$
$R_\star$ ($R_\odot$)	Stellar radius	$1.080^{+0.025}_{-0.024}$	$0.886^{+0.021}_{-0.017}$	$1.477^{+0.036}_{-0.032}$	$1.726^{+0.049}_{-0.047}$	1.069 ± 0.024
$\log g_\star$ (cgs)	Stellar surface gravity	$4.401^{+0.026}_{-0.029}$	$4.524^{+0.018}_{-0.029}$	$4.184^{+0.028}_{-0.035}$	$4.024^{+0.057}_{-0.039}$	4.400 ± 0.030
$\rho_\star$ ($g\ cm^{-3}$)	Stellar density	$1.198^{+0.090}_{-0.092}$	$1.94^{+0.11}_{-0.16}$	$0.531^{+0.045}_{-0.050}$	$0.316^{+0.048}_{-0.034}$	$1.22^{+0.11}_{-0.09}$
$L_\star$ ($L_\odot$)	Stellar luminosity	$1.202^{+0.088}_{-0.086}$	$0.560^{+0.037}_{-0.027}$	$2.445^{+0.084}_{-0.085}$	2.96 ± 0.14	$1.136^{+0.069}_{-0.063}$
T_{eff} (K)	Stellar effective temperature	5814^{+91}_{-93}	5306^{+76}_{-68}	5936^{+65}_{-68}	5760^{+80}_{-79}	5764^{+81}_{-78}
[Fe/H] (dex)	Metallicity	0.196 ± 0.084	0.344 ± 0.085	$0.158^{+0.084}_{-0.085}$	$0.13^{+0.09}_{-0.10}$	$0.239^{+0.076}_{-0.079}$
$[Fe/H]_0$ (dex)[c]	Initial metallicity	$0.192^{+0.077}_{-0.078}$	$0.309^{+0.079}_{-0.080}$	$0.212^{+0.073}_{-0.074}$	$0.167^{+0.084}_{-0.098}$	$0.228^{+0.071}_{-0.073}$
Age (Gyr)	Stellar age	$3.6^{+3.1}_{-2.3}$	$3.5^{+4.2}_{-2.4}$	$4.4^{+1.9}_{-1.2}$	$6.7^{+1.7}_{-2.6}$	$4.0^{+3.3}_{-2.5}$
EEP[d]	Equal evolutionary phase	351^{+39}_{-27}	334^{+25}_{-36}	404 ± 28	$451.4^{+5.9}_{-41.0}$	354^{+39}_{-28}
A_V (mag)	Visual extinction	$0.540^{+0.091}_{-0.098}$	$0.102^{+0.099}_{-0.069}$	$0.061^{+0.031}_{-0.038}$	$0.093^{+0.050}_{-0.058}$	$0.145^{+0.073}_{-0.072}$
d (pc)	Distance	418.7 ± 1.9	$218.63^{+0.89}_{-0.88}$	$561.2^{+2.9}_{-2.8}$	380.9 ± 3.2	352.4 ± 1.8

Table 7
(Continued)

		TOI-2803 b	TOI-2818 b	TOI-2842 b	TOI-2977 b	TOI-3023 b
Planet Parameters						
P (days)	Period	$1.96229325 \pm 0.00000082$	$4.0397090^{+0.0000024}_{-0.0000023}$	$3.5514058^{+0.0000077}_{-0.0000078}$	2.3505614 ± 0.0000025	3.9014971 ± 0.0000031
T_c ($\mathrm{BJD_{TDB}}$)	Time of conjunction	$2{,}459{,}207.68640^{+0.00022}_{-0.00023}$	$2{,}459{,}023.44641 \pm 0.00025$	$2{,}459{,}172.17909 \pm 0.00077$	$2{,}459{,}373.83677 \pm 0.00029$	$2{,}459{,}071.19220 \pm 0.00030$
T_{14} (days)	Transit duration	$0.12879^{+0.00080}_{-0.00074}$	$0.1585^{+0.0013}_{-0.0012}$	0.1073 ± 0.0022	$0.12225^{+0.00084}_{-0.00081}$	$0.2067^{+0.0010}_{-0.0009}$
τ (days)	Ingress/egress duration	$0.01545^{+0.00047}_{-0.00024}$	0.0182 ± 0.0013	$0.0216^{+0.0022}_{-0.0020}$	$0.01258^{+0.00039}_{-0.00024}$	$0.01750^{+0.00082}_{-0.00031}$
$a/R_\star$	Planet–star separation	$5.512^{+0.043}_{-0.070}$	$8.63^{+0.28}_{-0.25}$	8.07 ± 0.30	$6.806^{+0.059}_{-0.090}$	$6.53^{+0.06}_{-0.13}$
$(R_P/R_\star)^2$	Transit depth	0.01781 ± 0.00034	0.01300 ± 0.00030	$0.00867^{+0.00037}_{-0.00036}$	$0.01265^{+0.00034}_{-0.00033}$	0.00815 ± 0.00012
i (deg)	Inclination	$89.0^{+0.7}_{-1.0}$	$87.73^{+0.75}_{-0.55}$	$84.42^{+0.34}_{-0.35}$	$89.19^{+0.57}_{-0.82}$	$88.9^{+0.8}_{-1.0}$
K ($\mathrm{m\ s^{-1}}$)	RV semiamplitude	$146.7^{+11.0}_{-8.9}$	91 ± 33	$45.2^{+5.8}_{-5.4}$	266^{+39}_{-38}	74 ± 11
a (au)	Semimajor axis	0.03185 ± 0.00052	$0.0493^{+0.0010}_{-0.0008}$	$0.0475^{+0.0010}_{-0.0011}$	$0.03386^{+0.00067}_{-0.00050}$	$0.0505^{+0.0015}_{-0.0009}$
R_P (R_J)	Planet radius	$1.616^{+0.034}_{-0.032}$	$1.363^{+0.046}_{-0.045}$	$1.146^{+0.051}_{-0.048}$	$1.174^{+0.031}_{-0.027}$	$1.466^{+0.043}_{-0.032}$
M_P (M_J)	Planet mass	$0.975^{+0.083}_{-0.070}$	0.71 ± 0.26	$0.370^{+0.052}_{-0.047}$	$1.68^{+0.26}_{-0.25}$	$0.62^{+0.10}_{-0.09}$
ρ_P ($\mathrm{g\ cm^{-3}}$)	Planet density	$0.287^{+0.026}_{-0.023}$	$0.34^{+0.14}_{-0.13}$	$0.304^{+0.065}_{-0.056}$	$1.28^{+0.21}_{-0.20}$	$0.245^{+0.039}_{-0.038}$
$\log g_P$ (cgs)	Planet surface gravity	$2.966^{+0.035}_{-0.033}$	$2.98^{+0.14}_{-0.18}$	$2.843^{+0.071}_{-0.074}$	$3.479^{+0.062}_{-0.069}$	$2.856^{+0.062}_{-0.070}$
$b \equiv a \cos i/R_\star$	Transit impact parameter	$0.097^{+0.093}_{-0.067}$	$0.34^{+0.07}_{-0.11}$	$0.785^{+0.020}_{-0.022}$	$0.097^{+0.095}_{-0.067}$	$0.13^{+0.11}_{-0.09}$
e	Eccentricity	0.0 (fixed)	0.0 (fixed)	0.0 (fixed)	0.0 (fixed)	0.0 (fixed)
e_lim[a]	1σ upper limit on eccentricity	<0.097	<0.147	<0.090	<0.126	<0.097
τ_circ (Gyr)[b]	Tidal circularization timescale	$0.00542^{+0.00059}_{-0.00057}$	$0.190^{+0.086}_{-0.074}$	$0.149^{+0.049}_{-0.038}$	$0.089^{+0.017}_{-0.016}$	$0.111^{+0.019}_{-0.020}$
$\langle F \rangle$ ($\mathrm{Gerg\ s^{-1}\ cm^{-2}}$)	Incident flux	$2.92^{+0.18}_{-0.17}$	$0.814^{+0.064}_{-0.056}$	$1.064^{+0.087}_{-0.077}$	$1.290^{+0.091}_{-0.084}$	$1.475^{+0.092}_{-0.089}$
T_eq (K)	Planet equilibirum temperature	1893^{+29}_{-28}	1376^{+26}_{-24}	1471^{+29}_{-27}	1544 ± 26	1596^{+24}_{-25}
Stellar Parameters						
$M_\star$ ($M_\odot$)	Stellar mass	$1.118^{+0.056}_{-0.054}$	$0.977^{+0.063}_{-0.049}$	$1.135^{+0.077}_{-0.079}$	$0.936^{+0.057}_{-0.041}$	$1.12^{+0.11}_{-0.06}$
$R_\star$ ($R_\odot$)	Stellar radius	$1.245^{+0.022}_{-0.021}$	$1.229^{+0.032}_{-0.031}$	$1.265^{+0.040}_{-0.037}$	$1.073^{+0.024}_{-0.020}$	$1.668^{+0.046}_{-0.033}$
$\log g_\star$ (cgs)	Stellar surface gravity	$4.298^{+0.011}_{-0.015}$	$4.250^{+0.034}_{-0.030}$	$4.288^{+0.038}_{-0.040}$	$4.350^{+0.012}_{-0.013}$	$4.048^{+0.017}_{-0.021}$
$\rho_\star$ ($\mathrm{g\ cm^{-3}}$)	Stellar density	$0.822^{+0.019}_{-0.031}$	$0.745^{+0.074}_{-0.063}$	$0.789^{+0.093}_{-0.084}$	$1.078^{+0.028}_{-0.042}$	$0.346^{+0.009}_{-0.020}$
$L_\star$ ($L_\odot$)	Stellar luminosity	$2.17^{+0.14}_{-0.12}$	$1.46^{+0.11}_{-0.10}$	$1.76^{+0.15}_{-0.13}$	$1.089^{+0.095}_{-0.083}$	$2.78^{+0.22}_{-0.21}$
T_eff (K)	Stellar effective temperature	6280^{+99}_{-96}	5721^{+88}_{-83}	5910 ± 100	5691^{+94}_{-93}	5760^{+85}_{-88}
[Fe/H] (dex)	Metallicity	$-0.105^{+0.068}_{-0.072}$	$-0.02^{+0.11}_{-0.09}$	$0.233^{+0.087}_{-0.090}$	$0.013^{+0.087}_{-0.085}$	$0.085^{+0.084}_{-0.083}$
$[\mathrm{Fe/H}]_0$ (dex)[c]	Initial metallicity	$-0.025^{+0.058}_{-0.056}$	$0.040^{+0.093}_{-0.081}$	0.250 ± 0.076	$0.058^{+0.080}_{-0.078}$	$0.132^{+0.073}_{-0.075}$
Age (Gyr)	Stellar age	$3.7^{+1.5}_{-1.3}$	$9.5^{+2.6}_{-2.8}$	$4.7^{+3.0}_{-2.3}$	$9.8^{+2.6}_{-3.0}$	$7.0^{+1.7}_{-2.2}$
EEP[d]	Equal evolutionary phase	378^{+23}_{-29}	$426.7^{+9.5}_{-16.0}$	396^{+27}_{-47}	408^{+10}_{-18}	$449.7^{+5.4}_{-28.0}$
A_V (mag)	Visual extinction	$0.062^{+0.046}_{-0.043}$	$0.13^{+0.11}_{-0.08}$	0.21 ± 0.11	0.30 ± 0.12	$0.61^{+0.10}_{-0.11}$
d (pc)	Distance	501.1 ± 2.9	315.0 ± 1.0	460.2 ± 2.6	$355.7^{+9.5}_{-9.0}$	392.8 ± 1.4

Table 7
(Continued)

		TOI-3364 b	TOI-3688 b	TOI-3807 b	TOI-3819 b	TOI-3912 b
Planet Parameters						
P (days)	Period	5.8768918 ± 0.0000069	3.246075 ± 0.000012	$2.8989727^{+0.0000038}_{-0.0000039}$	3.2443141 ± 0.0000055	3.4936264 ± 0.0000038
T_c ($\mathrm{BJD_{TDB}}$)	Time of conjunction	$2{,}459{,}090.99481^{+0.00040}_{-0.00041}$	$2{,}459{,}108.0507 \pm 0.0014$	$2{,}459{,}218.13454 \pm 0.00055$	$2{,}459{,}502.74370 \pm 0.00038$	$2{,}459{,}442.81871^{+0.00037}_{-0.00036}$
T_{14} (days)	Transit duration	0.1936 ± 0.0013	$0.1451^{+0.0038}_{-0.0037}$	0.0742 ± 0.0019	$0.1158^{+0.0015}_{-0.0014}$	0.1482 ± 0.0014
τ (days)	Ingress/egress duration	$0.0149^{+0.0011}_{-0.0007}$	$0.0132^{+0.0012}_{-0.0008}$	$0.03710^{+0.00095}_{-0.00094}$	$0.0220^{+0.0015}_{-0.0014}$	$0.0176^{+0.0015}_{-0.0014}$
$a/R_\star$	Planet–star separation	$10.24^{+0.20}_{-0.32}$	$7.53^{+0.23}_{-0.25}$	$6.14^{+0.19}_{-0.18}$	6.43 ± 0.17	$7.16^{+0.25}_{-0.24}$
$(R_P/R_\star)^2$	Transit depth	$0.00624^{+0.00024}_{-0.00022}$	$0.00850^{+0.00043}_{-0.00042}$	0.0150 (>0.0136)	0.00613 ± 0.00013	0.00885 ± 0.00019
i (deg)	Inclination	$88.79^{+0.75}_{-0.68}$	$87.9^{+1.2}_{-1.0}$	79.96 (<80.81)	$82.79^{+0.30}_{-0.31}$	$85.64^{+0.55}_{-0.52}$
K ($\mathrm{m\ s^{-1}}$)	RV semiamplitude	168 ± 10	119^{+11}_{-13}	130^{+18}_{-16}	131^{+20}_{-23}	$51.2^{+8.5}_{-8.4}$
a (au)	Semimajor axis	$0.0675^{+0.0011}_{-0.0016}$	$0.04560^{+0.00089}_{-0.00098}$	$0.0421^{+0.0007}_{-0.0011}$	$0.04611^{+0.00069}_{-0.00096}$	$0.0463^{+0.0012}_{-0.0010}$
R_P (R_J)	Planet radius	$1.091^{+0.038}_{-0.032}$	$1.167^{+0.048}_{-0.044}$	2.00 (>1.65)	$1.172^{+0.036}_{-0.035}$	$1.274^{+0.041}_{-0.040}$
M_P (M_J)	Planet mass	$1.67^{+0.12}_{-0.13}$	$0.98^{+0.10}_{-0.11}$	$1.04^{+0.15}_{-0.14}$	$1.11^{+0.18}_{-0.20}$	$0.406^{+0.071}_{-0.068}$
ρ_P ($\mathrm{g\ cm^{-3}}$)	Planet density	$1.60^{+0.19}_{-0.20}$	$0.76^{+0.13}_{-0.12}$	0.065 (<0.289)	0.85 ± 0.17	$0.243^{+0.053}_{-0.047}$
$\log g_P$ (cgs)	Planet surface gravity	$3.542^{+0.039}_{-0.046}$	$3.251^{+0.056}_{-0.064}$	1.72 (<2.98)	$3.302^{+0.072}_{-0.087}$	$2.792^{+0.078}_{-0.087}$
$b \equiv a \cos i/R_\star$	Transit impact parameter	$0.22^{+0.11}_{-0.13}$	$0.27^{+0.13}_{-0.16}$	1.03 (>1.00)	$0.808^{+0.012}_{-0.013}$	$0.544^{+0.045}_{-0.052}$
e	Eccentricity	0.0 (fixed)	0.0 (fixed)	0.0 (fixed)	0.0 (fixed)	0.0 (fixed)
e_lim[a]	1σ upper limit on eccentricity	<0.036	<0.099	<0.098	<0.093	<0.102
τ_circ (Gyr)[b]	Tidal circularization timescale	$8.0^{+1.4}_{-1.5}$	$0.255^{+0.065}_{-0.056}$	0.0032 (<0.0293)	$0.287^{+0.075}_{-0.067}$	$0.088^{+0.026}_{-0.021}$
$\langle F \rangle$ ($\mathrm{Gerg\ s^{-1}\ cm^{-2}}$)	Incident flux	$0.579^{+0.042}_{-0.037}$	$1.258^{+0.098}_{-0.090}$	$1.67^{+0.10}_{-0.10}$	$1.614^{+0.083}_{-0.075}$	$1.187^{+0.065}_{-0.063}$
T_eq (K)	Planet equilibirum temperature	1264^{+22}_{-21}	1534^{+29}_{-28}	1646^{+25}_{-24}	1633^{+21}_{-19}	1512 ± 20
Stellar Parameters						
$M_\star$ ($M_\odot$)	Stellar mass	$1.186^{+0.059}_{-0.083}$	$1.199^{+0.072}_{-0.076}$	$1.181^{+0.064}_{-0.092}$	$1.242^{+0.057}_{-0.076}$	$1.088^{+0.086}_{-0.070}$
$R_\star$ ($R_\odot$)	Stellar radius	$1.419^{+0.036}_{-0.030}$	$1.302^{+0.038}_{-0.035}$	1.468 ± 0.037	1.538 ± 0.037	$1.392^{+0.035}_{-0.034}$
$\log g_\star$ (cgs)	Stellar surface gravity	$4.209^{+0.020}_{-0.033}$	$4.288^{+0.031}_{-0.035}$	$4.174^{+0.031}_{-0.035}$	$4.156^{+0.027}_{-0.029}$	$4.188^{+0.037}_{-0.038}$
$\rho_\star$ ($\mathrm{g\ cm^{-3}}$)	Stellar density	$0.587^{+0.035}_{-0.053}$	$0.767^{+0.073}_{-0.074}$	$0.521^{+0.050}_{-0.045}$	$0.478^{+0.040}_{-0.038}$	$0.569^{+0.061}_{-0.056}$
$L_\star$ ($L_\odot$)	Stellar luminosity	$1.93^{+0.16}_{-0.14}$	$1.92^{+0.16}_{-0.15}$	$2.15^{+0.14}_{-0.11}$	2.51 ± 0.11	$1.876^{+0.060}_{-0.059}$
T_eff (K)	Stellar effective temperature	5706^{+95}_{-91}	5950 ± 100	5772^{+84}_{-80}	5859^{+72}_{-71}	5725^{+69}_{-68}
[Fe/H] (dex)	Metallicity	$0.387^{+0.072}_{-0.081}$	$0.262^{+0.085}_{-0.086}$	$0.278^{+0.084}_{-0.081}$	$0.273^{+0.084}_{-0.082}$	$0.187^{+0.087}_{-0.090}$
$[\mathrm{Fe/H}]_0$ (dex)[c]	Initial metallicity	$0.392^{+0.062}_{-0.071}$	$0.277^{+0.073}_{-0.070}$	$0.301^{+0.074}_{-0.070}$	$0.297^{+0.077}_{-0.072}$	$0.227^{+0.076}_{-0.080}$
Age (Gyr)	Stellar age	$5.4^{+2.4}_{-1.5}$	$3.3^{+2.2}_{-1.7}$	$5.6^{+2.7}_{-1.5}$	$4.5^{+1.6}_{-1.1}$	$7.5^{+2.8}_{-2.5}$
EEP[d]	Equal evolutionary phase	414^{+21}_{-25}	374^{+38}_{-37}	420^{+22}_{-25}	408^{+22}_{-27}	432^{+11}_{-22}
A_V (mag)	Visual extinction	0.22 ± 0.11	0.52 ± 0.11	$0.119^{+0.084}_{-0.075}$	$0.077^{+0.046}_{-0.049}$	0.034 ± 0.023
d (pc)	Distance	$275.60^{+0.99}_{-0.98}$	400.9 ± 1.8	429.0 ± 2.0	$562.1^{+5.0}_{-4.9}$	470.0 ± 2.8

Table 7
(Continued)

		TOI-3976 b	TOI-4087 b	TOI-4145 b	TOI-4463 b	TOI-4791 b
Planet Parameters						
P (days)	Period	$6.607662^{+0.000016}_{-0.000015}$	$3.17748350 \pm 0.00000094$	4.0664428 ± 0.0000058	$2.8807198^{+0.0000028}_{-0.0000027}$	$4.280880^{+0.000022}_{-0.000023}$
T_c ($\mathrm{BJD_{TDB}}$)	Time of conjunction	$2{,}459{,}011.15791 \pm 0.00077$	$2{,}459{,}244.566414^{+0.000093}_{-0.000092}$	$2{,}458{,}925.88211^{+0.00017}_{-0.00016}$	$2{,}459{,}291.64004 \pm 0.00032$	$2{,}459{,}237.59508 \pm 0.00036$
T_{14} (days)	Transit duration	0.1882 ± 0.0022	$0.12434^{+0.00049}_{-0.00048}$	$0.08773^{+0.00098}_{-0.00095}$	$0.0772^{+0.0015}_{-0.0014}$	$0.1389^{+0.0015}_{-0.0014}$
τ (days)	Ingress/egress duration	$0.0173^{+0.0014}_{-0.0013}$	$0.01344^{+0.00052}_{-0.00049}$	$0.0271^{+0.0017}_{-0.0016}$	$0.0330^{+0.0061}_{-0.0041}$	$0.0175^{+0.0014}_{-0.0013}$
$a/R_\star$	Planet–star separation	$10.63^{+0.36}_{-0.35}$	8.63 ± 0.14	$12.07^{+0.24}_{-0.23}$	$8.17^{+0.21}_{-0.24}$	$8.46^{+0.27}_{-0.26}$
$(R_P/R_\star)^2$	Transit depth	0.00562 ± 0.00013	$0.011565^{+0.000099}_{-0.000097}$	$0.02015^{+0.00038}_{-0.00036}$	$0.01311^{+0.00091}_{-0.00054}$	0.00655 ± 0.00045
i (deg)	Inclination	$87.28^{+0.39}_{-0.36}$	$87.82^{+0.37}_{-0.33}$	86.20 ± 0.12	$83.82^{+0.21}_{-0.28}$	$85.55^{+0.34}_{-0.33}$
K ($\mathrm{m\ s^{-1}}$)	RV semiamplitude	$16.3^{+3.4}_{-3.3}$	90^{+17}_{-18}	57^{+17}_{-18}	$108.7^{+3.3}_{-2.9}$	250^{+32}_{-34}
a (au)	Semimajor axis	$0.0743^{+0.0013}_{-0.0014}$	$0.04469^{+0.00048}_{-0.00054}$	$0.04823^{+0.00075}_{-0.00079}$	$0.04036^{+0.00074}_{-0.00082}$	$0.0555^{+0.0011}_{-0.0012}$
R_P (R_J)	Planet radius	$1.095^{+0.036}_{-0.035}$	$1.164^{+0.025}_{-0.024}$	$1.187^{+0.032}_{-0.031}$	$1.183^{+0.064}_{-0.045}$	1.110 ± 0.050
M_P (M_J)	Planet mass	$0.175^{+0.037}_{-0.036}$	0.73 ± 0.14	0.43 ± 0.13	$0.794^{+0.039}_{-0.040}$	$2.31^{+0.32}_{-0.33}$
ρ_P ($\mathrm{g\ cm^{-3}}$)	Planet density	$0.165^{+0.041}_{-0.037}$	0.57 ± 0.12	$0.32^{+0.10}_{-0.10}$	$0.595^{+0.080}_{-0.096}$	$2.09^{+0.46}_{-0.40}$
$\log g_P$ (cgs)	Planet surface gravity	$2.56^{+0.09}_{-0.11}$	$3.125^{+0.077}_{-0.096}$	$2.88^{+0.12}_{-0.15}$	$3.148^{+0.040}_{-0.056}$	$3.668^{+0.071}_{-0.078}$
$b \equiv a \cos i/R_\star$	Transit impact parameter	$0.505^{+0.049}_{-0.059}$	$0.328^{+0.044}_{-0.051}$	$0.800^{+0.010}_{-0.011}$	$0.880^{+0.013}_{-0.009}$	$0.657^{+0.027}_{-0.030}$
e	Eccentricity	0.0 (fixed)	0.0 (fixed)	0.0 (fixed)	0.0 (fixed)	0.0 (fixed)
e_{lim}[a]	1σ upper limit on eccentricity	<0.207	<0.124	<0.135	<0.040	<0.152
τ_{circ} (Gyr)[b]	Tidal circularization timescale	$1.39^{+0.44}_{-0.37}$	$0.173^{+0.039}_{-0.037}$	$0.223^{+0.079}_{-0.071}$	$0.106^{+0.024}_{-0.027}$	$2.62^{+0.87}_{-0.66}$
$\langle F \rangle$ ($\mathrm{Gerg\ s^{-1}\ cm^{-2}}$)	Incident flux	$0.638^{+0.031}_{-0.027}$	$1.026^{+0.056}_{-0.046}$	$0.303^{+0.022}_{-0.018}$	$0.861^{+0.062}_{-0.052}$	$1.066^{+0.077}_{-0.068}$
T_{eq} (K)	Planet equilibirum temperature	1295^{+16}_{-14}	1458^{+20}_{-17}	1074^{+19}_{-16}	1395^{+25}_{-22}	1472^{+26}_{-24}
Stellar Parameters						
$M_\star$ ($M_\odot$)	Stellar mass	$1.254^{+0.067}_{-0.072}$	$1.178^{+0.039}_{-0.042}$	$0.905^{+0.043}_{-0.044}$	$1.056^{+0.059}_{-0.063}$	$1.242^{+0.072}_{-0.077}$
$R_\star$ ($R_\odot$)	Stellar radius	$1.501^{+0.039}_{-0.038}$	$1.112^{+0.021}_{-0.020}$	$0.859^{+0.018}_{-0.017}$	$1.062^{+0.027}_{-0.024}$	$1.409^{+0.039}_{-0.038}$
$\log g_\star$ (cgs)	Stellar surface gravity	$4.183^{+0.034}_{-0.035}$	$4.416^{+0.015}_{-0.016}$	$4.526^{+0.020}_{-0.021}$	$4.410^{+0.027}_{-0.032}$	$4.234^{+0.032}_{-0.033}$
$\rho_\star$ ($\mathrm{g\ cm^{-3}}$)	Stellar density	$0.521^{+0.055}_{-0.050}$	$1.205^{+0.060}_{-0.058}$	$2.01^{+0.12}_{-0.11}$	$1.24^{+0.10}_{-0.11}$	$0.624^{+0.062}_{-0.057}$
$L_\star$ ($L_\odot$)	Stellar luminosity	2.588 ± 0.069	$1.500^{+0.089}_{-0.069}$	$0.516^{+0.040}_{-0.031}$	$1.026^{+0.080}_{-0.062}$	$2.40^{+0.19}_{-0.16}$
T_{eff} (K)	Stellar effective temperature	5975^{+70}_{-69}	6060^{+74}_{-67}	5281^{+86}_{-76}	5640^{+89}_{-82}	6058^{+99}_{-94}
[Fe/H] (dex)	Metallicity	$0.182^{+0.078}_{-0.079}$	0.237 ± 0.079	$0.168^{+0.084}_{-0.087}$	0.250 ± 0.085	$0.207^{+0.085}_{-0.089}$
$[\mathrm{Fe/H}]_0$ (dex)[c]	Initial metallicity	$0.237^{+0.071}_{-0.072}$	$0.205^{+0.073}_{-0.074}$	$0.155^{+0.081}_{-0.083}$	$0.242^{+0.077}_{-0.078}$	$0.252^{+0.072}_{-0.073}$
Age (Gyr)	Stellar age	$3.8^{+1.5}_{-1.3}$	$0.8^{+1.2}_{-0.6}$	$4.7^{+4.2}_{-3.1}$	$4.1^{+3.5}_{-2.6}$	$3.3^{+1.8}_{-1.4}$
EEP[d]	Equal evolutionary phase	394^{+25}_{-42}	313^{+26}_{-41}	340^{+22}_{-30}	354^{+40}_{-27}	378 ± 35
A_V (mag)	Visual extinction	$0.038^{+0.015}_{-0.022}$	$0.089^{+0.072}_{-0.058}$	$0.16^{+0.12}_{-0.10}$	$0.15^{+0.11}_{-0.09}$	$0.16^{+0.10}_{-0.09}$
d (pc)	Distance	$522.2^{+2.5}_{-2.4}$	310.4 ± 1.1	204.96 ± 0.40	$177.64^{+0.56}_{-0.54}$	$322.1^{+1.9}_{-1.8}$

Notes. This table contains the fit results from the preferred fit for each target. Table 3 in Eastman et al. (2019) provides a detailed description of all derived and fitted parameters.
[a] This is 68% upper limit on eccentricity derived from the eccentric fits.
[b] The tidal circularization timescale is computed with Equation (3) of Adams & Laughlin (2006), assuming a tidal quality factor $Q_S = 10^6$.
[c] The stellar metallicity when the star was formed, which defines the grid points for the MIST stellar evolutionary tracks.
[d] The equal evolutionary phase (EEP) corresponds to specific points in the stellar evolutionary tracks, as described in Dotter (2016). Table 7 is published in its entirety online. This version only shows the results from the preferred fit for each target. The full version includes these results and fits where the eccentricity was allowed to float. Note that the full version also includes the results from the additional fit parameters outlined in Table 11.

(This table is available in its entirety in machine-readable form.)

Table 8
Spectroscopic Stellar Properties

Target	Code	Instrument	$T_{\rm eff}$ (K)	$R_\star$ ($R_\odot$)	log g (dex)	[Fe/H] (dex)	$v \sin i$ (km s^{-1})	$v_{\rm mac}$ (km s^{-1})	Adopted
TOI-1937	SpecMatch	PFS	5798 ± 110	1.16 ± 0.21	⋯	0.22 ± 0.09	8.0 ± 1.0	3.8 ± 0.2	Y
TOI-2364	SpecMatch	PFS	5271 ± 110	0.96 ± 0.10	⋯	0.36 ± 0.09	1.3 ± 1.0	4.5 ± 0.2	Y
TOI-2583	SpecMatch	HIRES	5867 ± 110	1.39 ± 0.25	⋯	0.15 ± 0.09	2.4 ± 1.0	3.7 ± 0.2	Y
⋯	SPC	TRES	6059 ± 50	⋯	4.35 ± 0.10	0.29 ± 0.08	5.2 ± 0.5	⋯	N
TOI-2587	SpecMatch	NEID	5766 ± 110	1.92 ± 0.34	⋯	0.17 ± 0.09	2.8 ± 1.0	4.2 ± 0.2	Y
⋯	SPC	TRES	5792 ± 50	⋯	4.22 ± 0.10	0.15 ± 0.08	4.2 ± 0.5	⋯	N
TOI-2796	SpecMatch	NEID	5721 ± 110	1.27 ± 0.18	⋯	0.22 ± 0.09	2.7 ± 1.0	4.3 ± 0.2	Y
⋯	SPC	TRES	5742 ± 58	⋯	4.44 ± 0.10	0.32 ± 0.08	6.0 ± 0.5	⋯	N
TOI-2803	SpecMatch	PFS	6151 ± 110	1.80 ± 0.32	⋯	−0.43 ± 0.09	2.2 ± 1.0	3.6 ± 0.2	N
⋯	SPC	TRES	6058 ± 108	⋯	4.26 ± 0.18	−0.11 ± 0.10	5.4 ± 0.8	⋯	N
⋯	SPC	TRES	6277 ± 70	⋯	4.30 (fixed)	−0.11 ± 0.08	5.4 ± 0.8	⋯	Y
⋯	ZASPE	PFS	6436 ± 80	⋯	4.30 (fixed)	−0.35 ± 0.07	4.8 ± 0.3	⋯	N
TOI-2818	SpecMatch	CHIRON	5715 ± 110	1.24 ± 0.22	⋯	0.02 ± 0.09	2.9 ± 1.0	4.0 ± 0.2	Y
⋯	SPC	CHIRON	5767 ± 50	⋯	4.27 ± 0.10	−0.06 ± 0.10	5.2 ± 0.5	⋯	N
TOI-2842	SpecMatch	PFS	5942 ± 110	1.59 ± 0.29	⋯	0.26 ± 0.09	5.2 ± 1.0	3.6 ± 0.2	Y
⋯	SPC	TRES	6004 ± 75	⋯	4.30 ± 0.13	0.35 ± 0.08	7.6 ± 0.5	⋯	N
TOI-2977	SpecMatch	CHIRON	5674 ± 110	1.15 ± 0.21	⋯	0.04 ± 0.09	4.7 ± 1.0	4.0 ± 0.2	Y
⋯	SPC	CHIRON	5790 ± 74	⋯	4.25 ± 0.21	0.05 ± 0.10	6.2 ± 0.5	⋯	N
TOI-3023	SpecMatch	PFS	5651 ± 110	1.85 ± 0.33	⋯	0.09 ± 0.09	3.0 ± 1.0	4.0 ± 0.2	Y
TOI-3364	SpecMatch	PFS	5626 ± 110	1.49 ± 0.27	⋯	0.39 ± 0.09	2.0 ± 1.0	4.3 ± 0.2	Y
TOI-3688	SpecMatch	NEID	5909 ± 110	1.69 ± 0.31	⋯	0.26 ± 0.09	4.3 ± 1.0	4.2 ± 0.2	Y
⋯	SPC	TRES	6110 ± 50	⋯	4.33 ± 0.10	0.47 ± 0.08	6.3 ± 0.5	⋯	N
TOI-3807	SpecMatch	NEID	5755 ± 110	1.88 ± 0.34	⋯	0.31 ± 0.09	3.1 ± 1.0	3.9 ± 0.2	Y
⋯	SPC	TRES	5942 ± 50	⋯	4.34 ± 0.10	0.41 ± 0.08	5.5 ± 0.5	⋯	N
TOI-3819	SpecMatch	NEID	5847 ± 110	1.95 ± 0.35	⋯	0.29 ± 0.09	5.8 ± 1.0	4.0 ± 0.2	Y
⋯	SPC	TRES	5964 ± 50	⋯	4.29 ± 0.10	0.41 ± 0.08	6.8 ± 0.5	⋯	N
TOI-3912	SpecMatch	HIRES	5730 ± 110	1.48 ± 0.27	⋯	0.19 ± 0.09	2.3 ± 1.0	3.7 ± 0.2	Y
⋯	SPC	TRES	5829 ± 50	⋯	4.29 ± 0.10	0.22 ± 0.08	4.4 ± 0.5	⋯	N
TOI-3976	SpecMatch	HIRES	5942 ± 110	1.33 ± 0.24	⋯	0.17 ± 0.09	2.0 ± 1.0	3.6 ± 0.2	Y
⋯	SPC	TRES	6032 ± 64	⋯	4.30 ± 0.11	0.36 ± 0.08	5.3 ± 0.5	⋯	N
TOI-4087	SpecMatch	NEID	5888 ± 110	1.18 ± 0.21	⋯	0.27 ± 0.09	4.6 ± 1.0	4.0 ± 0.2	Y
⋯	SPC	TRES	5957 ± 50	⋯	4.43 ± 0.10	0.27 ± 0.08	6.5 ± 0.5	⋯	N
TOI-4145	SpecMatch	NEID	5266 ± 110	0.87 ± 0.09	⋯	0.20 ± 0.09	2.2 ± 1.0	4.8 ± 0.2	Y
⋯	SPC	TRES	5380 ± 50	⋯	4.63 ± 0.10	0.24 ± 0.08	3.8 ± 0.5	⋯	N
TOI-4463	SpecMatch	NEID	5566 ± 110	1.14 ± 0.21	⋯	0.28 ± 0.09	1.6 ± 1.0	4.2 ± 0.2	Y
⋯	SPC	TRES	5646 ± 50	⋯	4.42 ± 0.10	0.17 ± 0.08	3.4 ± 0.5	⋯	N
TOI-4791	SpecMatch	CHIRON	6011 ± 110	1.77 ± 0.32	⋯	0.23 ± 0.09	10.9 ± 1.0	3.3 ± 0.2	Y
⋯	SPC	CHIRON	6128 ± 50	⋯	4.27 ± 0.10	0.12 ± 0.10	11.2 ± 0.5	⋯	N
⋯	SPC	TRES	6231 ± 50	⋯	4.31 ± 0.10	0.42 ± 0.08	11.9 ± 0.5	⋯	N

at 5.″3, which was also resolved by Gaia (Figure 3). We performed a multicomponent SED fit (lower panels of Figure 7) for these two targets similarly to TOI-2977. The broadband photometry is compatible with an M0.5V stellar companion to TOI-1937A and an M2.5V stellar companion to TOI-2583A. We only included dilution corrections to the ground-based photometry for TOI-1937A, but not for TOI-2583A, where the ground-based photometry resolved both stellar components.

In the case of TOI-1937A and TOI-2583A, our spectroscopic observations resolved the primary; thus the spectroscopic properties and RV variations are measured for the primary star. The TESS SPOC Data Validation reports (doi:10.17909/t9-2tc5-a751, doi:10.17909/t9-yjj5-4t42) for these two targets also showed that the difference image centroid offset compared with the TIC positions were 0.″89 ± 2.″54 for TOI-1937A and 1.″75 ± 2.″5 for TOI-2583A, indicating that the transits did occur on the primary star. For TOI-2977A, while the spectroscopic observations did not resolve the 0.″77 companion, we did not detect its line in the measured spectrum, nor were there large BIS variations, suggesting that the measured RV variations are also due to motion of the primary star.

3.3. Potential Cluster Membership

3.3.1. TOI-1937: Ambiguous Member of NGC 2516

TOI-1937 was reported by Kounkel & Covey (2019) to be a member of the southern open cluster NGC 2516 ($d \approx 400$ pc, $t \approx 150$ Myr, $M_{\rm tot} \approx 1400\,M_\odot$; Bouma et al. 2021; Meingast et al. 2021). Very few if any hot Jupiters have well-measured ages below a few hundred million years. If TOI-1937 were a member of NGC 2516, it would therefore likely represent a new upper limit for the arrival time of hot Jupiters on their close-in orbits, which might in turn help to constrain the mechanism by which these planets migrate. We investigated the possible cluster membership of TOI-1937 by considering the available six-dimensional positions and kinematics of the star relative to the cluster, the stellar rotation period, the photospheric lithium content, and the stellar metallicity. Our analysis drew heavily from the rotation and lithium analyses performed by Bouma et al. (2021). We ultimately found that current evidence for the cluster membership of TOI-1937 is inconclusive, as laid out

Table 9
Properties of Stellar Companions

	Primary	Secondary
TOI-1937		
Gaia DR3 ID	5489726768531119616	5489726768531118848
TIC ID	268301217	766593811
Ang. Sep. (″)	⋯	2.48
Proj. Sep. (au)	⋯	1030
Parallax (mas)	2.411 ± 0.011	2.351 ± 0.089
μ_α (mas yr^{-1})	-5.627 ± 0.013	-5.39 ± 0.10
μ_δ (mas yr^{-1})	11.309 ± 0.013	11.349 ± 0.096
RV (km s^{-1})	24.8 ± 2.5	⋯
G (mag)	13.005 ± 0.003	17.649 ± 0.003
$G_{\rm BP}$ (mag)	13.417 ± 0.003	17.9 ± 0.1
$G_{\rm RP}$ (mag)	12.421 ± 0.004	16.25 ± 0.02
T (mag)	12.493 ± 0.006	16.86 ± 0.08
TOI-2583		
Gaia DR3 ID	2115776451371641984	2115776451371641472
TIC ID	7548817	7548819
Ang. Sep. (″)	⋯	5.26
Proj. Sep. (au)	⋯	2927
Parallax (mas)	1.7970 ± 0.0090	1.66 ± 0.13
μ_α (mas yr^{-1})	7.831 ± 0.011	7.59 ± 0.16
μ_δ (mas yr^{-1})	4.991 ± 0.012	4.80 ± 0.19
RV (km s^{-1})	-38.3 ± 1.1	⋯
G (mag)	12.453 ± 0.003	18.707 ± 0.004
$G_{\rm BP}$ (mag)	12.759 ± 0.003	19.34 ± 0.09
$G_{\rm RP}$ (mag)	11.983 ± 0.004	17.39 ± 0.03
T (mag)	12.045 ± 0.007	17.87 ± 0.03
TOI-2587		
Gaia DR3 ID	3085216850017388672	3085216850017388032
TIC ID	68007716	68007714
Ang. Sep. (″)	⋯	8.88
Proj. Sep. (au)	⋯	3334
Parallax (mas)	2.664 ± 0.022	2.625 ± 0.019
μ_α (mas yr^{-1})	22.004 ± 0.023	21.595 ± 0.019
μ_δ (mas yr^{-1})	-25.296 ± 0.019	-25.542 ± 0.016
RV (km s^{-1})	-24.71 ± 0.35	-24.4 ± 1.8
G (mag)	11.405 ± 0.003	13.702 ± 0.003
$G_{\rm BP}$ (mag)	11.738 ± 0.003	14.162 ± 0.003
$G_{\rm RP}$ (mag)	10.909 ± 0.004	13.077 ± 0.004
T (mag)	10.966 ± 0.006	13.147 ± 0.006
TOI-2803		
Gaia DR3 ID	2913482170369046656	2913482170369045120
TIC ID	124379043	124379044
Ang. Sep. (″)	⋯	19.54
Proj. Sep. (au)	⋯	9656
Parallax (mas)	2.023 ± 0.012	2.024 ± 0.012
μ_α (mas yr^{-1})	0.7490 ± 0.0090	0.7950 ± 0.0090
μ_δ (mas yr^{-1})	11.908 ± 0.011	11.972 ± 0.011
RV (km s^{-1})	24.7 ± 1.2	24.9 ± 1.4
G (mag)	12.417 ± 0.003	12.753 ± 0.003
$G_{\rm BP}$ (mag)	12.669 ± 0.003	13.025 ± 0.003
$G_{\rm RP}$ (mag)	12.006 ± 0.004	12.326 ± 0.004
T (mag)	12.075 ± 0.006	12.395 ± 0.006
TOI-3688		
Gaia DR3 ID	4541879811886471 68	4541879811929255 68
TIC ID	245509452	245509454
Ang. Sep. (″)	⋯	4.96
Proj. Sep. (au)	⋯	1976
Parallax (mas)	2.512 ± 0.011	2.51 ± 0.18
μ_α (mas yr^{-1})	18.7770 ± 0.0090	18.86 ± 0.17
μ_δ (mas yr^{-1})	-11.398 ± 0.013	-11.13 ± 0.25
RV (km s^{-1})	0.69 ± 0.61	⋯
G (mag)	12.357 ± 0.003	18.434 ± 0.004
$G_{\rm BP}$ (mag)	12.772 ± 0.003	19.51 ± 0.06
$G_{\rm RP}$ (mag)	11.776 ± 0.004	17.08 ± 0.01
T (mag)	11.84 ± 0.01	17.03 ± 0.01
TOI-3976		
Gaia DR3 ID	1585783740516554624	1585783706157262720
TIC ID	154293917	1102055625
Ang. Sep. (″)	⋯	6.81
Proj. Sep. (au)	⋯	3526
Parallax (mas)	1.9310 ± 0.0090	1.98 ± 0.21
μ_α (mas yr^{-1})	-19.8310 ± 0.0080	-19.81 ± 0.19
μ_δ (mas yr^{-1})	10.118 ± 0.011	9.45 ± 0.27
RV (km s^{-1})	-44.68 ± 0.69	⋯
G (mag)	12.211 ± 0.003	19.158 ± 0.004
$G_{\rm BP}$ (mag)	12.511 ± 0.003	20.1 ± 0.1
$G_{\rm RP}$ (mag)	11.751 ± 0.004	17.89 ± 0.03
T (mag)	11.814 ± 0.007	18.29 ± 0.04
TOI-4145		
Gaia DR3 ID	568619413331898240	568619417628568704
TIC ID	279947414	629870229
Ang. Sep. (″)	⋯	1.74
Proj. Sep. (au)	⋯	356
Parallax (mas)	4.9017 ± 0.0096	5.71 ± 0.16
μ_α (mas yr^{-1})	11.690 ± 0.010	11.93 ± 0.20
μ_δ (mas yr^{-1})	-13.534 ± 0.011	-16.83 ± 0.59
RV (km s^{-1})	1.16 ± 0.54	⋯
G (mag)	12.049 ± 0.003	17.367 ± 0.005
$G_{\rm BP}$ (mag)	12.472 ± 0.003	⋯
$G_{\rm RP}$ (mag)	11.463 ± 0.004	⋯
T (mag)	11.524 ± 0.006	16.6 ± 0.6
TOI-4463		
Gaia DR3 ID	4524517290642206336	4524517290642204928
TIC ID	8599009	8599017
Ang. Sep. (″)	⋯	11.37
Proj. Sep. (au)	⋯	2009
Parallax (mas)	5.659 ± 0.018	5.644 ± 0.067
μ_α (mas yr^{-1})	-5.157 ± 0.017	-5.258 ± 0.068
μ_δ (mas yr^{-1})	50.619 ± 0.017	50.977 ± 0.072
RV (km s^{-1})	-90.38 ± 0.32	⋯
G (mag)	10.951 ± 0.003	16.768 ± 0.003
$G_{\rm BP}$ (mag)	11.324 ± 0.003	18.28 ± 0.02
$G_{\rm RP}$ (mag)	10.411 ± 0.004	15.539 ± 0.005
T (mag)	10.467 ± 0.006	15.482 ± 0.008

Notes. The angular and projected separation between the two components are from the catalog of El-Badry et al. (2021). T magnitude is from the TESS Input Catalog (Stassun et al. 2018, 2019), while all remaining parameters, including systemic RVs, are drawn from Gaia DR3 (Katz et al. 2022; Gaia Collaboration et al. 2022).

in the following paragraphs. We do note, however, that multiple age indicators would need to be compromised by the presence of the hot Jupiter if the star were a member of NGC 2516. Implications for whether TOI-1937 is a young hot Jupiter, or whether it is simply a tidally spun-up field star, are discussed in Section 5.1.

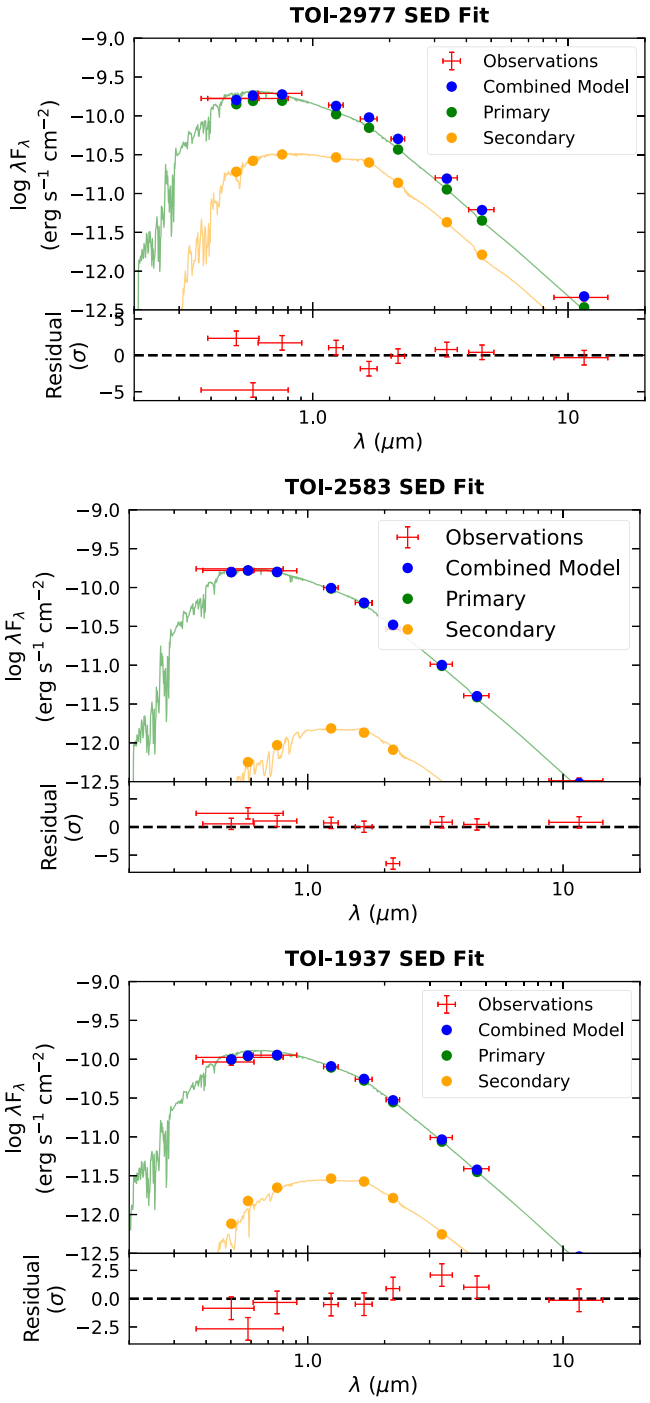

Figure 7. Multicomponent SED fit for the TOI-2977 system (top), TOI-2583 system (middle), and TOI-1937 system (bottom). The red points with vertical error bars show the observed catalog fluxes and uncertainties from Gaia, 2MASS, and WISE, while the horizontal error bars illustrate the width of the photometric band. The green and orange points show the model fluxes of the primary and secondary, respectively, while the blue points show the combined flux of both stars. For illustrative purposes, we underplot extinction-corrected Kurucz (1993) atmospheric models for the two stellar components, although these models were not used directly in the fit, which was based on MIST bolometric correction tables. For TOI-2583, the 6σ residual between the model and observed flux in the K_s band reflects a large discrepancy between the difference as measured by 2MASS (Δ(mag) = 1.7) and by the ShARCS AO imaging (Δ(mag) = 4.0). We excluded the 2MASS K_s-band flux from the SED fit, relying on the AO measurements instead, but show the residual here.

Positions, kinematics, and false-positive rates analyses of the positions and kinematics of NGC 2516 from Gaia DR2 yielded the discovery of tidal tails that lead and lag up to ±250 pc from the central core of the cluster, relative to its orbit in the galaxy (Kounkel & Covey 2019; Meingast et al. 2021). A visualization is available online.[68] TOI-1937 was included as a member of the trailing tail by Kounkel & Covey (2019). The star was not reported as a cluster member by Meingast et al. (2021) due to a more stringent cut on the maximum tangential velocities out to which a star could be considered as a candidate cluster member. The reality of the tidal tails is supported by inspection of the lowest-mass M-dwarfs, which are more luminous than their field counterparts, as one would expect for ≈150 Myr pre-main-sequence stars. The stellar rotation periods also show a gyrochronal locus consistent with other open clusters (Bouma et al. 2021). However, the expected field star contaminant rate from the clustering algorithms used by both Kounkel & Covey (2019) and Meingast et al. (2021) is expected to increase with separation from the core of the cluster; Bouma et al. 2021 estimated that up to ≈40% of the candidate members in the outermost regions of the cluster's tidal tails are in fact field stars.

TOI-1937 is in this wide-separation regime (Figure 8): it is ≈70 pc outside the core of the cluster, with a tangential on-sky velocity that is ≈5.4 km s^{-1} separate from that of the cluster core, although its systemic velocity of $RV_{sys} = 22.4 \pm 0.1$ km s^{-1} is consistent with that of NGC 2516 (23.8 ± 1.1 km s^{-1}; Healy & McCullough 2020). The spatial and kinematic evidence, coupled with the fraction of nearby stars that are likely field interlopers, leaves the cluster membership of TOI-1937 ambiguous.

Rotation and Gyrochronology. A Lomb–Scargle analysis of the TESS sector 34, 35, and 36 light curves yields a rotation period for TOI-1937 of 6.6 ± 0.2 days (Figure 9). At $(G_{BP} - G_{RP})_0 = 0.87$, comparable stars on the slow sequence of NGC 2516 have rotation periods between 4.0 and 5.5 days. Similar-age clusters such as the Pleiades have an

Table 10
TOI-2977 Stellar Properties from SED Fit

	Primary	Secondary
Stellar Properties		
$T_{\rm eff}$ (K)	$5737.0^{+90.0}_{-92.0}$	$4614.0^{+83.0}_{-81.0}$
[Fe/H] (dex)	$0.017^{+0.076}_{-0.078}$	$0.044^{+0.072}_{-0.073}$
Age (Gyr)	$5.5^{+3.0}_{-2.8}$	$5.5^{+3.0}_{-2.8}$
$M_\star$ ($M_\odot$)	0.978 ± 0.046	$0.734^{+0.023}_{-0.024}$
$R_\star$ ($R_\odot$)	$1.004^{+0.037}_{-0.034}$	0.698 ± 0.016
log g (cgs)	$4.424^{+0.040}_{-0.041}$	$4.615^{+0.013}_{-0.014}$
Synthetic Photometry		
G (mag)	12.57 ± 0.02	$14.50^{+0.10}_{-0.09}$
$G_{\rm BP}$ (mag)	12.94 ± 0.02	15.1 ± 0.1
$G_{\rm RP}$ (mag)	12.03 ± 0.02	$13.76^{+0.09}_{-0.08}$
T (mag)	12.02 ± 0.02	$13.74^{+0.09}_{-0.08}$
B_T (mag)	13.58 ± 0.03	16.3 ± 0.2
V_T (mag)	12.80 ± 0.02	15.0 ± 0.1
J (mag)	11.42 ± 0.02	$12.81^{+0.07}_{-0.06}$
H (mag)	11.06 ± 0.02	12.18 ± 0.05
K (mag)	11.01 ± 0.02	12.08 ± 0.05
W1 (mag)	10.98 ± 0.02	12.04 ± 0.05
W2 (mag)	11.00 ± 0.02	12.10 ± 0.05
W3 (mag)	10.96 ± 0.02	12.00 ± 0.05

[68] https://homepage.univie.ac.at/stefan.meingast/coronae.html made by Meingast et al. (2021), last accessed 2022 July 30.

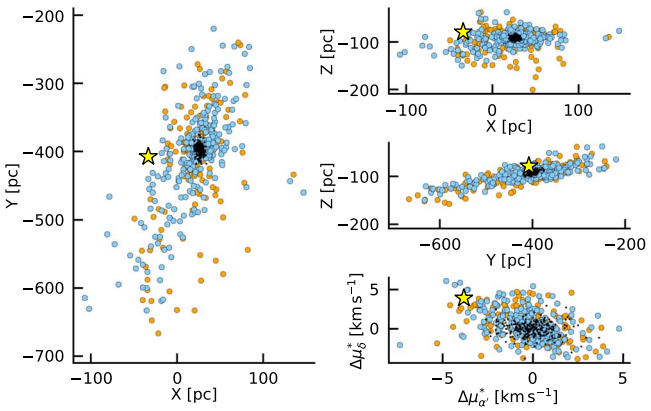

Figure 8. *XYZ* galactic coordinates and on-sky velocities of TOI-1937 (yellow star) in relation to the NGC 2516 cluster. The galactic center is in the direction of $+\hat{X}$, and galactic rotation is in the direction of $+\hat{Y}$. The black dots represent stars in the core of the cluster; blue circles are stars that are rotationally confirmed to be in the tidal tails; orange circles are reported candidate members of the tidal tails for which stellar rotation was expected but not detected. The latter are likely field interlopers. In the vicinity of TOI-1937, the contamination rate from such stars is about one in three.

indistinguishable distribution of G-dwarf rotation periods. (Fritzewski et al. 2020). The rotation period of TOI-1937A would therefore imply a gyrochronal age of ≈300–400 Myr, based on the gyrochronal loci of M 48 and NGC 3532 (Barnes et al. 2015; Fritzewski et al. 2021). The rotation period is well below that of the Praesepe slow sequence (≈700 Myr; Douglas et al. 2017).

The main assumption of gyrochronology—that spin down is dominated by magnetic braking—may not be applicable to TOI-1937 due to the presence of the hot Jupiter. There is a significant amount of population-level evidence that hot Jupiters can tidally spin up their host stars (Maxted et al. 2015; Cameron & Jardine 2018; Penev et al. 2018; Tejada Arevalo et al. 2021). Given the short orbital period ($P < 1$ day) of the hot Jupiter TOI-1937A b, this may be the case for TOI-1937A, which would imply that the gyrochronal age of TOI-1937A is unreliable and the system may in fact be older than inferred.

Lithium. Photospheric lithium can be used as an age diagnostic for FGKM stars (Soderblom 2010). One well-studied feature is the Li I 6708 Å doublet, and at least 90% of 150 Myr old Sunlike stars show it in absorption (e.g., Soderblom et al. 1993; Bouma et al. 2021). Given its stellar mass, TOI-1937A would be expected to display an equivalent width for this doublet of 110–140 mÅ if it were a bona fide member of NGC 2516 (Bouma et al. 2021). Field stars of the same mass typically show an equivalent width between 0 and 70 mÅ (Berger et al. 2018). Using the highest S/N PFS spectrum available, from 11 November 2020, we find $\mathrm{EW_{Li}} < 25.1$ mÅ at 3σ, after correcting for the neighboring Fe I blend at 6707.44 Å. The nondetection of lithium would be quite anomalous for a 150 Myr solar-mass star. While as with gyrochronology, one could imagine scenarios in which the hot Jupiter affects the stellar lithium abundance (Israelian et al. 2009; Figueira et al. 2014; Delgado Mena et al. 2015), this would require special justification. The lack of lithium is the strongest argument against the membership of TOI-1937 in NGC 2516.

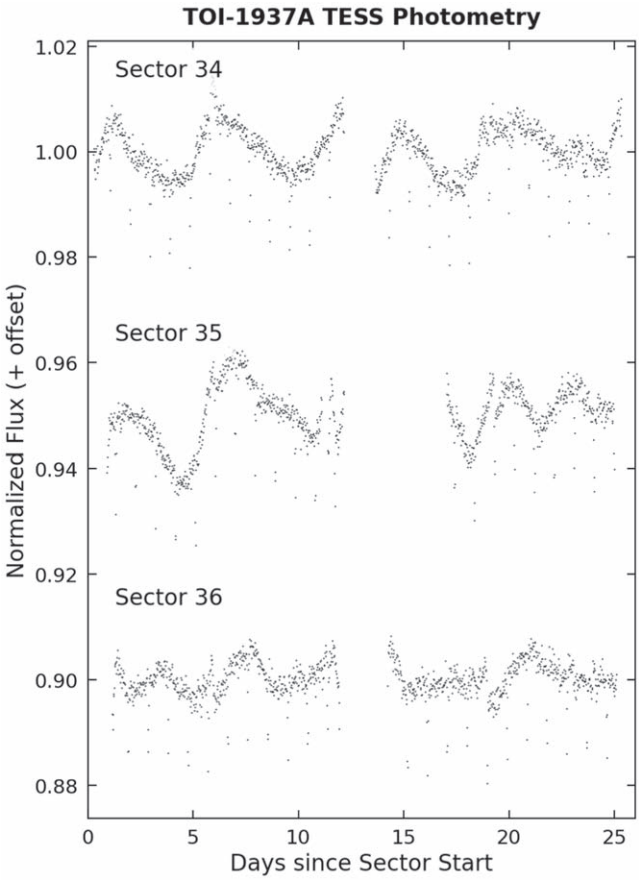

Figure 9. TESS SPOC light curves from sectors 34–36 for TOI-1937, binned to 30 minutes cadence. The planetary transits as well as the 6.6 day rotational modulation are clearly visible in the light curves.

Metallicity. The most up-to-date analysis of the metallicity of NGC 2516 appears to be that of Baratella et al. (2020) (but see Bailey et al. 2018). The study by Baratella et al. (2020) suggested that for young stars, using only Fe lines to estimate the microturbulence parameter could yield overestimates, which can propagate to yield underestimated cluster abundances. Based on 10 spectra of Sunlike stars in NGC 2516 acquired with VLT/FLAMES, they report a mean cluster metallicity of $[\mathrm{Fe/H}] = 0.08 \pm 0.01$. Our application of `SpecMatch-Emp` to the PFS spectra of TOI-1937 yielded $[\mathrm{Fe/H}] = 0.22 \pm 0.09$, which, while slightly higher than the cluster metallicity, is approximately consistent within the uncertainties.

3.3.2. TOI-4145: Not a Member of Platais-3

TOI-4145 was reported, also by Kounkel & Covey (2019), to be a candidate member of Platais-3 based on its 3D positions and 2D sky velocities from Gaia DR2. The mean distance of the cluster is $d \approx 180$ pc, and its age could be between 210 and 440 Myr (Bossini et al. 2019; Kounkel & Covey 2019). Similar to TOI-1937, the star is in the positional and kinematic outskirts of the cluster—it would need to be in its "corona," or "tidal tail," but the false-positive rates in the membership lists in this region of Platais-3 are much less well quantified than they are for NGC 2516. Regardless, the cluster's age range, combined with the stellar $T_{\mathrm{eff}} \approx 5400$ K, leads to some

immediate predictions that can confirm or refute membership. First, the rotation period should be between 7 and 9 days, with an amplitude of 0.2%–2% (Fritzewski et al. 2021). Second, the EW_{Li} should be between 50 and 120 mÅ.

The TESS light curves of TOI-4145 do not show any evidence for a rotation signal. The photometric precision achieved is $\approx$400 ppm $hr^{1/2}$, well in excess of what would be necessary to detect the relevant rotation signal. The NEID spectra similarly yield a nondetection with $EW_{Li} < 33.5$ mÅ at 3σ, after excluding the Fe blend. There is therefore no corroborating evidence for TOI-4145 being a bona fide member of Platais-3.

4. Planetary System Characterization

We used the EXOFASTv2 code (Eastman et al. 2013, 2019) to fit all the available data for each target and thereby characterize each planetary system. EXOFASTv2 fits the broadband photometry, transit light curves, and RV time series with a self-consistent stellar and planetary model. For example, the constraint on the stellar density from the transit model is forced to be consistent with the constraint on the stellar properties from fitting the broadband photometry. The uncertainties on each parameter are measured through a differential evolution Markov Chain Monte Carlo (DE-MCMC) exploration of the posterior distribution.

We follow the same fitting strategy as used in Paper I but reiterate the key points here. We use the SpecMatch-Emp-derived spectroscopic parameters and uncertainties as Gaussian priors on the stellar $T_{\rm eff}$, $R_\star$, and [Fe/H]. A Gaussian prior is also imposed on the stellar parallax, with the mean and standard deviation derived from the zero-point-corrected Gaia DR3 parallax measurement (Lindegren et al. 2021). We incorporate the Gaia and 2MASS photometry with an error floor of 0.02 mag and the WISE photometry with an error floor of 0.03 mag. An upper limit on the line-of-sight extinction A_V is imposed based on the sky coordinates of each target and the dust maps from Schlegel et al. (1998) and Schlafly & Finkbeiner (2011).

We fit the radial velocities with independent offset and jitter terms for each instrument and target but did not allow for any linear or quadratic RV trends because the data did not suggest such terms were necessary. For the systems with only two TRES observations, we did not include the TRES RVs in the fit, since doing so would require adding two more free parameters (a per-instrument offset and jitter term) for the same number of new data points. However, we include those TRES data points in Figure 15 for illustrative purposes, with the relative RV offset computed by a simple χ^2 minimization to the best-fitting RV model.

The transit light curves are fit by a quadratic limb-darkened transit model from Mandel & Agol (2002) and Agol et al. (2020), with the limb-darkening coefficients constrained by the tables from Claret & Bloemen (2011) and Claret (2017) during the EXOFASTv2 fit. When fitting the long-cadence 30 minute and 10 minute data from TESS, this model is computed at 2 minute intervals and integrated over the length of the exposure, to account for distortions in the transit shape arising from the finite integration time of the observations (e.g., Kipping 2010). Although the TESS light curves are in theory already corrected for dilution from neighboring stars in the same pixel, this assumes that all stars are accounted for with correct magnitudes in the TESS Input Catalog (TIC; Stassun et al. 2018, 2019). To account for possible errors in this correction, we allowed for an additional dilution factor to be fit for the TESS light curves, imposing a Gaussian prior centered at zero and with a width equal to 10% of size of the dilution factor already corrected for in the TIC. We also fitted for a separate flux baseline F_0 and added variance σ^2 for each sector of TESS data as well as each ground-based light curve. The ground-based light curves are simultaneously detrended against the variables listed in Table 3, assuming an additive detrending model.

We ran the EXOFASTv2 fit until the DE-MCMC algorithm converged under the criteria recommended by Eastman et al. (2019): Gelman–Rubin statistic (Gelman & Rubin 1992) $GR < 1.01$ and more than 1000 independent MCMC draws. As in Paper I, we ran two fits per system—one in which the eccentricity was fixed to zero and one in which the eccentricity was allowed to float. We adopted the zero-eccentricity set of parameters as our fiducial results but also state the 1σ upper limits on the eccentricity derived from the latter fit.

Two of the objects, TOI-2796b and TOI-3807b, were found to be on orbits that lead to grazing transits. In these cases, fitting the light curve leads to a strong covariance between the impact parameter b and planet-to-star radius ratio $R_p/R_\star$. The EXOFASTv2 MCMC exploration of the posterior distributions for these parameters shows long tails out to unphysical values for the planet radius. For these objects, instead of reporting the median of the posterior distribution for the planet radius R_p and impact parameter b, we report the posterior modes as well as the 95% lower limits on these parameters (and corresponding lower or upper limits for those parameters that depend directly on R_p and b).

We present the results and 1σ uncertainties from our MCMC fitting procedures in Tables 7 and 11 and plot the light curve, RV, and stellar flux data alongside the best-fit models in Figure 15. The full set of fitted parameters is provided as machine-readable data behind the figure accompanying the online version of this paper.

5. Discussion

The 20 newly confirmed hot Jupiters in this paper bring us closer to a complete, magnitude-limited sample of transiting giant planets that may reveal new insights into their formation and subsequent evolution. In this section, we place them in context by comparing them with the previously known hot Jupiter sample from the NASA Exoplanet Archive (NASA Exoplanet Archive 2022).[69]

Figure 10 shows the Gaia color–magnitude diagram of all currently known hot Jupiters. Our 20 new planets all orbit FGK dwarfs, which was one of our survey's selection criteria for follow-up observations of planet candidates. All but one of them orbit host stars consistent with supersolar metallicities, with the median [Fe/H] of our sample being +0.2 dex (Figure 11), as expected based on the steep dependence of the occurrence rate of hot Jupiters and metallicity of their host stars (Santos et al. 2004; Valenti & Fischer 2005). This connection has been interpreted as arising from the greater ease of forming giant planets in high-metallicity disks (e.g., Mordasini et al. 2012), eventually producing hot Jupiters either through disk migration or via scattering events between planets, further enhancing this correlation (Dawson & Murray-Clay 2013; Buchhave et al. 2018).

[69] https://exoplanetarchive.ipac.caltech.edu/, accessed 2022 August 16.

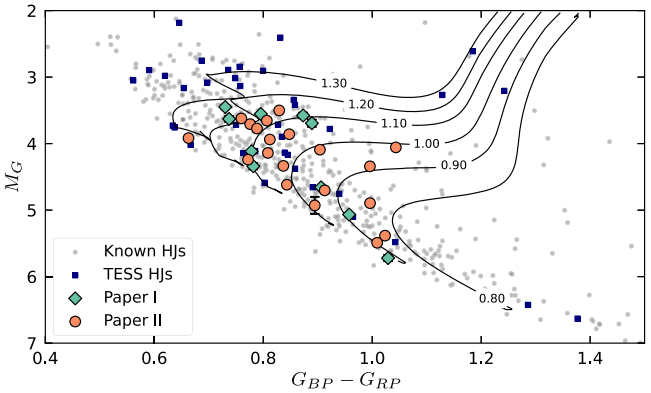

Figure 10. Gaia $G_{BP} - G_{RP}$ vs. G color–magnitude diagram for known hot Jupiter hosts in the NASA Exoplanet Archive (gray points). The orange circles show the newly confirmed planets described in this paper, while the green diamonds show the planets from Paper I. Navy blue squares represent the other confirmed hot Jupiters discovered by the TESS mission. We also plot the MIST evolutionary tracks for a metallicity of [Fe/H] = +0.20 dex, equal to the median metallicity of the stellar hosts in our sample, labeled with the corresponding stellar mass between 0.8 and 1.3 $M_\odot$. The symbols in this plot are consistent with those used in the following figures.

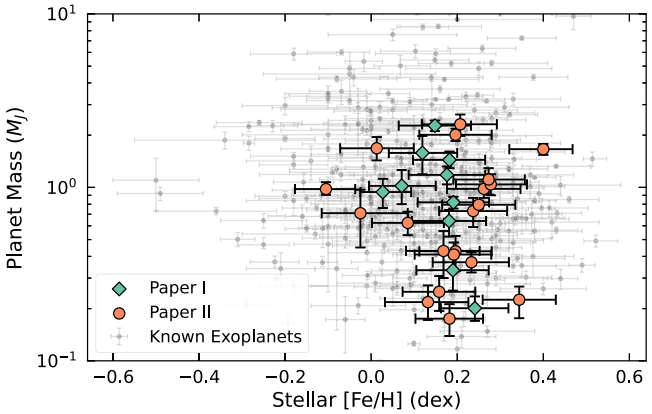

Figure 11. The distribution of hot Jupiters in the planet mass–stellar metallicity plane. Most gas giants orbit metal-rich stars, and our sample of planets follows this tendency, with a median metallicity of [Fe/H] = +0.20 dex.

TOI-2803b is the only planet in our sample orbiting a host with subsolar metallicity, with our adopted spectroscopic metallicity of [Fe/H] = − 0.11 ± 0.08 dex. However, we note that the `SpecMatch-Emp` and `ZASPE` analyses of the PFS template spectrum returned much lower spectroscopic metallicities of [Fe/H] = − 0.43 ± 0.09 and −0.35 ± 0.07 dex, respectively (see discussion in Section 3.1.1). If the low-metallicity results were accurate, TOI-2803b would be a surprising outlier, with only a handful of other hot Jupiters reported to orbit host stars with lower metallicities. Resolving this discrepancy in the stellar properties may be possible with future higher S/N observations or more detailed stellar modeling.

The observations for all 20 planets presented in this paper are consistent with the planets being on circular orbits, and as such we have adopted those fits for our fiducial set of parameters. This is unsurprising given the short tidal circularization timescales for most of these planets. We also performed fits for all the systems where eccentricity was allowed to float, allowing us to obtain upper limits on the eccentricity for each system. In most cases, the limited number of RV measurements per system does not allow us to constrain the eccentricity to much better than $e \lesssim 0.1$. However, for TOI-3364b, a planet on a $P = 5.88$ day orbit with the longest tidal circularization timescale in our sample, we were able to put a 1σ upper limit of $e < 0.036$.

We also note that for TOI-3976b, the longest-period planet in our sample ($P = 6.61$ days), the eccentric fit found $e = 0.180^{+0.060}_{-0.056}$, roughly 3σ greater than zero. We compared the circular and eccentric models using the Bayesian information criterion (BIC; Schwarz 1978) and found that the circular model is favored by $\Delta(\mathrm{BIC}) = 5$. Additional future observations may help place better constraints on the eccentricity of this longer-period hot Jupiter.

We also present the distribution of planet radii and bulk densities as a function of planet mass in Figure 12. Four of the objects in our sample (TOI-2364b, TOI-2583b, TOI-2587b, and TOI-3976b) are sub-Saturns, with masses less than 0.3 M_J. Three of them are highly inflated, with bulk densities $\rho_P < 0.25$ g cm^{-3}, similar to other objects in this regime. TOI-2364b does not appear to be inflated, nor would we expect it to be inflated given the comparatively low incident flux it receives; the host star (K0V, $T_{\rm eff} \approx 5300$ K) is one of the cooler stars in our sample.

Finally, we show in Figure 13 the distribution of planet radii with planet equilibrium temperature. Our planets are consistent with the radius inflation trend seen with the previously known sample (e.g., Demory & Seager 2011). One noteworthy planet is TOI-1937A b, which is relatively smaller than expected given its close-in ($P < 1$ day) orbit.

5.1. TOI-1937A b: Youngest Hot Jupiter, or Just Tidally Spun Up?

Section 3.3.1 described the evidence for, and against, the membership of TOI-1937 in NGC 2516 (150 Myr). The position and kinematics of the star suggest a probability of ≈60% that it is a member of the cluster's trailing tidal tail. The stellar rotation period is fast relative to the field, but in detail it would be more consistent with a gyrochronal age of 300–400 Myr, not 150 Myr. The supersolar metallicity is approximately consistent with that of other cluster members, although a homogeneous assessment using identical instruments and pipelines would help confirm this suggestion. The nondetection of lithium would be quite anomalous for a 150 Myr Solar-mass star and seems to be the best evidence for TOI-1937 being a field interloper. If TOI-1937A were a cluster member, the presence of the hot Jupiter would need to have both somehow spun down the star and also caused it to deplete its lithium much faster than is typical for Sunlike stars.

The alternative is that TOI-1937A is simply a tidally spun-up field star. If we take the age of the star to be $\gtrsim 1$ Gyr, as suggested by the lack of lithium, then by gyrochronal arguments, the rotation period should be $\gtrsim 11$ days, based on the observed rotation sequence of NGC-6811 (Curtis et al. 2019). The actual 6.6 day stellar spin period is highly discordant from this prediction. Combined with the 22.7 hr orbital period, which is much shorter than that of most hot Jupiters (Figure 14), TOI-1937 would seem to be a system that

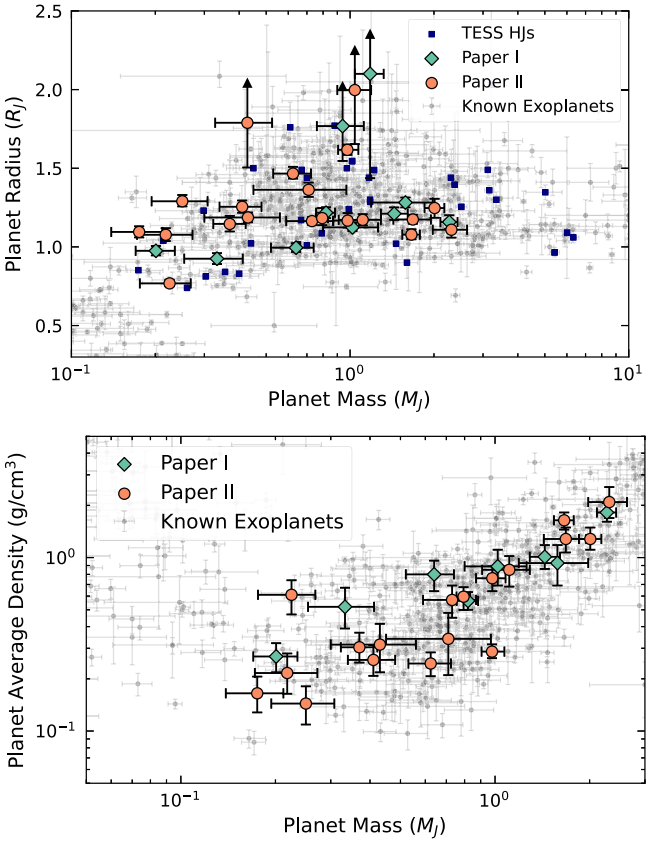

Figure 12. Top: planet mass–radius distribution for the newly confirmed hot Jupiters from our survey. For the objects with grazing transits, we plot the mode of the radius posterior distribution and the 2σ lower limit. Bottom: planet bulk density as a function of planet mass. In this plot, we have excluded the planets with grazing transits due to the large uncertainty in the planet density.

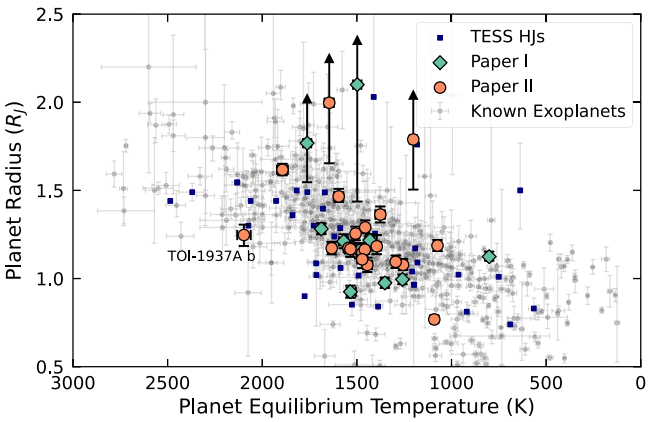

Figure 13. Distribution of planet radius as a function of planet equilibrium temperature, computed at the planets' semimajor axis and assuming no albedo and perfect heat redistribution. TOI-1937A b is anomalously small for its orbit and is labeled in the plot.

could provide new constraints on tidal spin-up, and perhaps eventually orbital decay.

6. Conclusions

We have confirmed and characterized 20 new short-period giant planets detected by the TESS mission, based on extensive

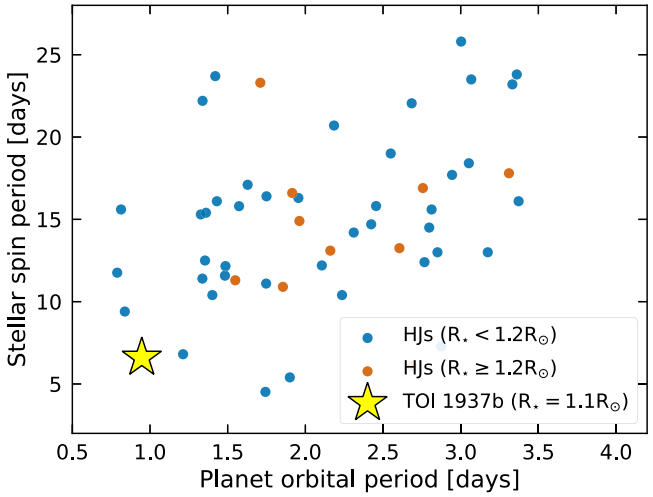

Figure 14. Stellar spin periods and planetary orbital periods for hot Jupiters. Data were collected by Penev et al. (2018); we only show hot Jupiter systems with stellar spin period S/Ns of at least 3. For a dwarf star, the 1.2 $R_\odot$ radius boundary corresponds to a stellar effective temperature of 6000 K, slightly below the Kraft break. Stars hotter than the Kraft break experience less efficient stellar spin down as the outer convection zone shrinks.

ground-based photometric, spectroscopic, and imaging observations. These objects join a host of other giant planets that have been discovered by TESS over the last few years (e.g., Rodriguez et al. 2019; Zhou et al. 2019; Brahm et al. 2020; Davis et al. 2020; Nielsen et al. 2020; Ikwut-Ukwa et al. 2021; Rodriguez et al. 2021; Sha et al. 2021; Wong et al. 2021; Knudstrup et al. 2022; Psaridi et al. 2022; Rodriguez et al. 2022; Yee et al. 2022), showcasing how TESS is rapidly transforming our knowledge of hot Jupiters by providing a uniform, all-sky sample of these planets.

Yee et al. (2021) found that the sample of known transiting hot Jupiters was only ∼40% complete at a magnitude-limit of $G < 12.5$. Since that publication, many planets have been newly confirmed, closing the gap between the number of expected planets and the number of known planets. Our survey has contributed to the confirmation of 30 of these objects and is continuing to observe more than 100 TESS planet candidates. This has only been possible with the collaboration of the broader community, in particular the many members of TFOP whose observations are key for guiding target selection and host star and planet characterization and making efficient use of follow-up resources.

The ultimate goal of our survey is to use TESS to assemble a relatively complete and unbiased sample of hot Jupiters with which we can study the demographics of this population of planets. We expect that TESS will be mostly complete to detecting such planets orbiting stars down to a magnitude limit of $G < 12.5$, and the ≈400 objects expected in such a sample will enable new investigations into the period, radius, and bulk density distributions of hot Jupiters, along with their correlations with host star properties like stellar metallicity. This large sample of planets will also be useful for selecting the most promising targets for additional studies, such as transit timing and obliquity measurements, as well as atmospheric characterization by missions like the James Webb Space Telescope (JWST) and the Atmospheric Remote-sensing Infrared Exoplanet Large-survey (ARIEL; Tinetti et al. 2016).

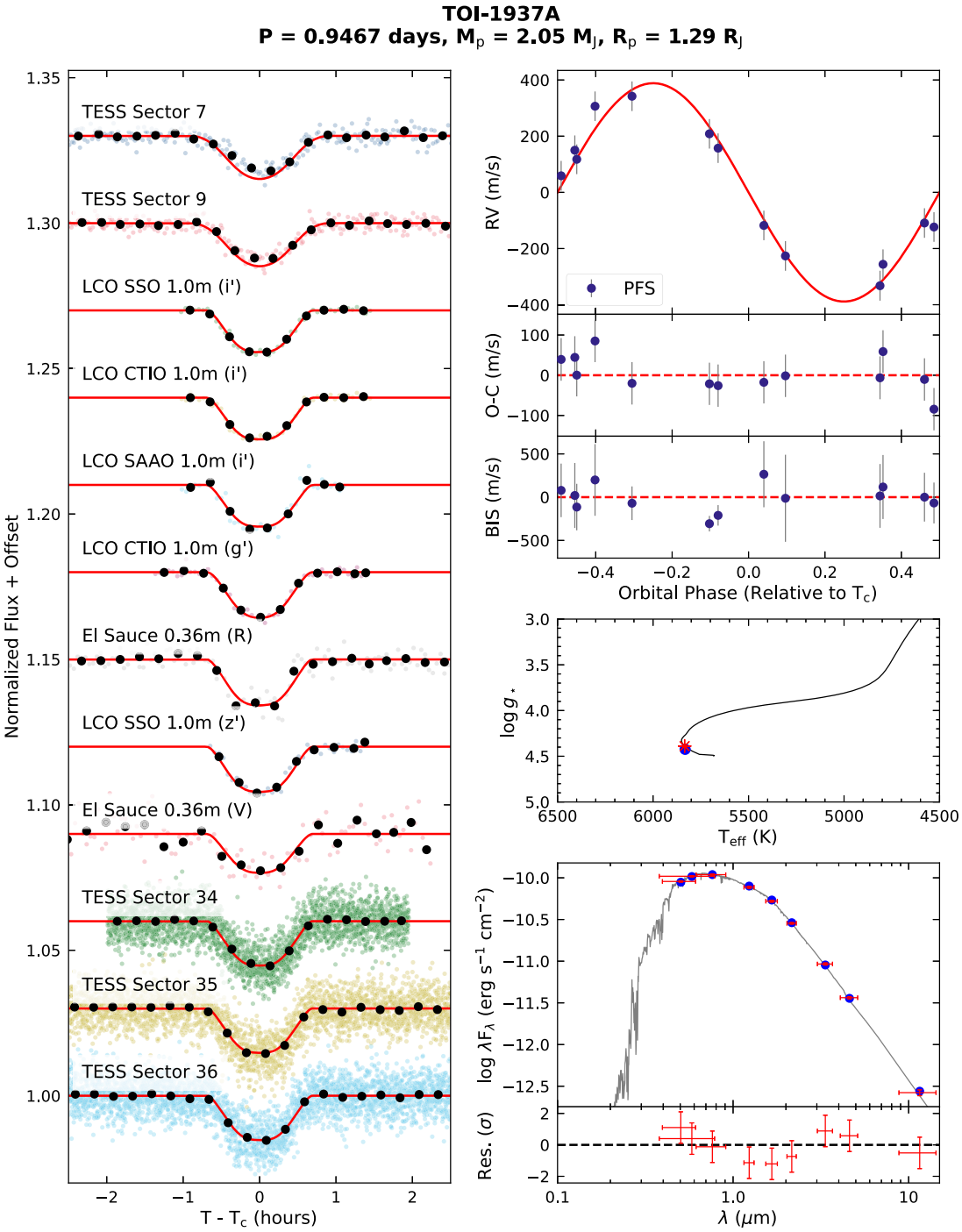

Figure 15. EXOFASTv2 fit results for TOI-1937A b. Left: TESS and ground-based light curves, phase folded onto the best-fit period and time of conjunction. The faint colored points are the unbinned data, while the black dots show the time-series data binned to 10 minutes cadence. The best-fit transit model in each band is shown as the red line. Top right: RV observations, also phased onto the best-fit orbital period. The fitted per-instrument jitter term $\sigma_{\rm jit}$ has been added in quadrature to the instrumental uncertainties to produce the gray error bars. The red line shows the best-fit circular model for the RVs. We plot the residuals after subtracting the model in the middle subpanel and the phased bisector span measurements in the lower subpanel. Middle right: the best-fit stellar $T_{\rm eff}$ and $\log g$ are plotted as the blue point. The best-fit MIST stellar evolution track is plotted in black, with the red asterisk showing the position along the track corresponding to the best-fit stellar age. The discrepancy between the blue point and red asterisk are well within the fitted uncertainties in each parameter, indicating no tension between the different constraints on the stellar properties. Bottom right: the observed stellar fluxes from the Gaia, Tycho, 2MASS, and WISE catalogs are plotted in red, with horizontal error bars corresponding to the width of the photometric bandpass. The blue points show the best-fit model flux derived from the stellar properties and MIST bolometric correction grid. We plot in gray an atmospheric model from Kurucz (1993) corresponding to the best-fit stellar parameters for illustrative purposes only, as the fit is performed directly to the MIST grid. The TESS and ground-based time-series photometry, as well as the RV measurements, is available as data behind the figure.

(The data used to create this figure are available.)

(The complete figure set (20 images) is available.)

We thank the anonymous reviewer for helpful comments that improved this manuscript.

This paper includes data collected by the TESS mission that are publicly available from the Mikulski Archive for Space Telescopes (MAST). The raw TESS data can be accessed at 10.17909/t9-nmc8-f686 (SPOC 2 minutes light curves), 10.17909/t9-wpz1-8s54 (TESS-SPOC FFI light curves), 10.17909/t9-r086-e880 (QLP light curves), and 10.17909/t9-ayd0-k727 (CDIPS light curves). The Data Validation reports are available at 10.17909/t9-2tc5-a751 and 10.17909/t9-yjj5-4t42. Funding for the TESS mission is provided by NASA's Science Mission Directorate. We acknowledge the use of public TESS data from pipelines at the TESS Science Office and at the TESS SPOC. Resources supporting this work were provided by the NASA High-End Computing (HEC) Program through the NASA Advanced Supercomputing (NAS) Division at Ames Research Center for the production of the SPOC data products. We also acknowledge the use of data from the Exoplanet Follow-up Observation Program website, which is operated by the California Institute of Technology, under contract with the National Aeronautics and Space Administration under the Exoplanet Exploration Program (ExoFOP 2019; NExScI 2022).

This research made use of Lightkurve, a Python package for Kepler and TESS data analysis (Lightkurve Collaboration et al. 2018). We acknowledge that the work reported on in this paper was substantially performed using the Princeton Research Computing resources at Princeton University, which is a consortium of groups led by the Princeton Institute for Computational Science and Engineering (PICSciE) and Office of Information Technology's Research Computing.

Some of the data presented herein were obtained at the W. M. Keck Observatory, which is operated as a scientific partnership among the California Institute of Technology, the University of California, and the National Aeronautics and Space Administration. The observatory was made possible by the generous financial support of the W. M. Keck Foundation. Keck telescope time was granted by NOIRLab (Prop. IDs 2021B-0162, 2022A-543544, PI: Yee) through the Mid-Scale Innovations Program (MSIP). MSIP is funded by NSF. The authors wish to recognize and acknowledge the very significant cultural role and reverence that the summit of Maunakea has always had within the indigenous Hawaiian community. We are most fortunate to have the opportunity to conduct observations from this mountain.

This paper contains data taken with the NEID instrument, which was funded by the NASA-NSF Exoplanet Observational Research (NN-EXPLORE) partnership and built by Pennsylvania State University. NEID is installed on the WIYN telescope, which is operated by the National Optical Astronomy Observatory, and the NEID archive is operated by the NASA Exoplanet Science Institute at the California Institute of Technology. NN-EXPLORE is managed by the Jet Propulsion Laboratory, California Institute of Technology, under contract with the National Aeronautics and Space Administration. Data presented herein were obtained at the WIYN Observatory from telescope time allocated to NN-EXPLORE through the scientific partnership of the National Aeronautics and Space Administration, the National Science Foundation, and NOIRLab. This work was supported by a NASA WIYN PI Data Award, administered by the NASA Exoplanet Science Institute. The authors are honored to be permitted to conduct astronomical research on Iolkam Duâag (Kitt Peak), a mountain with particular significance to the Tohono Oâodham.

This paper includes data gathered with the 6.5 m Magellan Telescopes located at Las Campanas Observatory, Chile.

This research has used data from the CTIO/SMARTS 1.5 m telescope, which is operated as part of the SMARTS Consortium by RECONS (http://www.recons.org) members Todd Henry, Hodari James, Wei-Chun Jao, and Leonardo Paredes. At the telescope, observations were carried out by Roberto Aviles and Rodrigo Hinojosa. The CHIRON data were obtained from telescope time allocated under the NN-EXPLORE program with support from the National Aeronautics and Space Administration.

This work makes use of observations from the LCOGT network. Part of the LCOGT telescope time was granted by NOIRLab through the Mid-Scale Innovations Program (MSIP). MSIP is funded by NSF.

J.H. acknowledges funding from NASA grant 80NSSC21K0335. This work was supported by an LSSTC Catalyst Fellowship awarded by LSST Corporation to T.D. with funding from the John Templeton Foundation grant ID No. 62192. K.K.M. acknowledges support from the New York Community Trustâs Fund for Astrophysical Research. N.L.-B. thanks the NASA Massachusetts Space Grant for support. A.A.B., N.A.M., and B.S.S. acknowledge the support of the Ministry of Science and Higher Education of the Russian Federation under the grant 075-15-2020-780 (N13.1902.21.0039). A.P. acknowledges grant BK-246/RAu-11/2022. The research leading to these results has received funding from the ARC grant for Concerted Research Actions, financed by the Wallonia-Brussels Federation. TRAPPIST is funded by the Belgian Fund for Scientific Research (Fond National de la Recherche Scientifique, FNRS) under the grant PDR T.0120.21. TRAPPIST-North is a project funded by the University of Liege (Belgium), in collaboration with Cadi Ayyad University of Marrakech (Morocco). M. Gillon is F.R.S.-FNRS Research Director. E.J. is F.R.S.-FNRS Senior Research Associate. This publication benefits from the support of the French Community of Belgium in the context of the FRIA Doctoral Grant awarded to M.T.

Facilities: TESS, Keck:I (HIRES), Magellan:Clay (PFS), WIYN (NEID, NESSI), CTIO:1.5 m (CHIRON), FLWO:1.5m (TRES), FLWO:1.2m (KeplerCam), LCOGT, TRAPPIST-North, WASP, CMO:2.5 m (SPP), Gemini:Gillett ('Alopeke), Gemini:South (Zorro), Hale (PHARO), SOAR (HRCam), Shane (ShARCS).

Software: astropy (Astropy Collaboration et al. 2013, 2018), lightkurve (Lightkurve Collaboration et al. 2018), EXOFASTv2 (Eastman et al. 2013, 2019), SpecMatch-Emp (Yee et al. 2017), SpecMatch-Synth (Petigura 2015), AstroImageJ (Collins et al. 2017), TAPIR (Jensen 2013), numpy (Harris et al. 2020), scipy (Virtanen et al. 2020), pandas (McKinney 2010; pandas development team 2020), matplotlib (Hunter 2007).

Appendix
Additional Fit Parameters

We present in Table 11 the median and 68% confidence intervals for additional fit parameters not listed in Table 10 for the adopted fits. These are the linear and quadratic limb-darkening parameters (u_1, u_2) in each band, additional flux dilution from neighboring stars in each band (D), the relative RV offset for each instrument $\gamma_{\rm rel}$ (meters per second), and the RV jitter for each instrument σ_J (meters per second).

Table 11
Additional Fit Parameters (Median and 68% Confidence Intervals)

Parameter						
TOI-1937						
	R	g'	i'	z'	TESS	V
u_1	$0.369^{+0.053}_{-0.052}$	$0.598^{+0.055}_{-0.056}$	0.309 ± 0.032	0.270 ± 0.052	0.305 ± 0.027	0.462 ± 0.054
u_2	$0.276^{+0.051}_{-0.050}$	0.211 ± 0.052	0.278 ± 0.029	0.298 ± 0.050	0.277 ± 0.023	0.246 ± 0.052
A_D	$-0.35^{+0.17}_{-0.21}$	$-0.36^{+0.17}_{-0.21}$	$-0.16^{+0.13}_{-0.16}$	$-0.23^{+0.15}_{-0.19}$	$-0.20^{+0.13}_{-0.16}$	⋯
	PFS					
$\gamma_{\rm rel}$	-59 ± 15					
σ_J	52^{+16}_{-11}					
TOI-2364						
	R	TESS				
u_1	$0.479^{+0.049}_{-0.050}$	$0.385^{+0.034}_{-0.033}$				
u_2	0.208 ± 0.050	$0.224^{+0.036}_{-0.035}$				
A_D	⋯	-0.0002 ± 0.0029				
	PFS	TRES				
$\gamma_{\rm rel}$	$-4.9^{+3.9}_{-3.8}$	-30^{+24}_{-19}				
σ_J	$7.8^{+8.2}_{-3.6}$	19^{+44}_{-20}				
TOI- 2583						
	B	I	g'	z'	TESS	
u_1	0.611 ± 0.051	0.260 ± 0.048	0.554 ± 0.046	$0.197^{+0.048}_{-0.049}$	0.291 ± 0.025	
u_2	0.168 ± 0.051	0.278 ± 0.049	0.239 ± 0.049	0.269 ± 0.050	0.296 ± 0.025	
A_D	⋯	⋯	⋯	⋯	0.0020 ± 0.0069	
	HIRES					
$\gamma_{\rm rel}$	$0.2^{+4.2}_{-4.4}$					
σ_J	$7.3^{+11}_{-7.3}$					
TOI-2587						
	i'	r'	TESS			
u_1	0.309 ± 0.052	0.391 ± 0.052	$0.311^{+0.037}_{-0.036}$			
u_2	0.282 ± 0.050	$0.272^{+0.051}_{-0.050}$	0.284 ± 0.035			
A_D	⋯	⋯	-0.000 ± 0.014			
	NEID					
$\gamma_{\rm rel}$	$-24502.3^{+4.1}_{-3.7}$					
σ_J	$8.2^{+6.4}_{-5.1}$					
TOI-2796						
	B	g'	i'	TESS		
u_1	0.658 ± 0.055	0.611 ± 0.051	$0.319^{+0.051}_{-0.052}$	0.322 ± 0.037		
u_2	0.115 ± 0.053	0.197 ± 0.051	$0.275^{+0.051}_{-0.050}$	0.280 ± 0.035		
A_D	⋯	⋯	⋯	0.00000 ± 0.00092		
	HIRES	NEID				
$\gamma_{\rm rel}$	-4 ± 27	$20592.2^{+8.5}_{-9.0}$				
σ_J	47^{+32}_{-24}	$19.9^{+15}_{-8.7}$				
TOI-2803						
	B	R	g'	i'	TESS	
u_1	0.518 ± 0.040	0.311 ± 0.048	0.471 ± 0.043	0.195 ± 0.048	0.239 ± 0.031	
u_2	0.239 ± 0.038	0.335 ± 0.049	0.285 ± 0.048	0.286 ± 0.049	$0.301^{+0.033}_{-0.034}$	
A_D	⋯	⋯	⋯	⋯	0.046 ± 0.019	
	PFS	TRES				
$\gamma_{\rm rel}$	$121.0^{+10.}_{-9.3}$	243 ± 59				
σ_J	$20.3^{+19}_{-8.8}$	61^{+28}_{-61}				
TOI-2818						
	R	g'	TESS			
u_1	0.428 ± 0.042	$0.570^{+0.055}_{-0.054}$	0.308 ± 0.028			
u_2	0.315 ± 0.047	0.195 ± 0.053	0.276 ± 0.029			
A_D	⋯	⋯	0.022 ± 0.014			
	CHIRON					
$\gamma_{\rm rel}$	58996 ± 28					
σ_J	64^{+50}_{-25}					
TOI-2842						

Table 11
(Continued)

Parameter						
	B	*R*	TESS			
u_1	0.648 ± 0.056	0.371 ± 0.053	0.287 ± 0.038			
u_2	0.165 ± 0.054	0.301 ± 0.051	0.284 ± 0.036			
A_D	⋯	⋯	-0.005 ± 0.017			
	PFS					
$\gamma_{\rm rel}$	$-1.6^{+4.2}_{-3.7}$					
σ_J	$5.3^{+9.9}_{-5.3}$					
TOI-2977						
	R	g'	i'	TESS		
u_1	0.315 ± 0.045	$0.602^{+0.055}_{-0.054}$	$0.318^{+0.052}_{-0.051}$	0.315 ± 0.030		
u_2	0.237 ± 0.049	0.206 ± 0.053	0.269 ± 0.050	0.272 ± 0.029		
A_D	0.150 ± 0.014	0.0966 ± 0.0096	0.162 ± 0.016	$0.146^{+0.024}_{-0.025}$		
	CHIRON					
$\gamma_{\rm rel}$	7839^{+34}_{-33}					
σ_J	66^{+79}_{-37}					
TOI-3023						
	R	i'	TESS			
u_1	0.342 ± 0.045	0.291 ± 0.050	0.288 ± 0.024			
u_2	0.275 ± 0.048	0.269 ± 0.050	0.272 ± 0.025			
A_D	⋯	⋯	0.003 ± 0.010			
	PFS					
$\gamma_{\rm rel}$	$-43.1^{+8.1}_{-8.3}$					
σ_J	$17.7^{+18}_{-7.7}$					
TOI-3364						
	R	TESS				
u_1	$0.376^{+0.049}_{-0.050}$	0.335 ± 0.029				
u_2	0.248 ± 0.050	0.275 ± 0.029				
A_D	⋯	$-0.024^{+0.034}_{-0.035}$				
	PFS					
$\gamma_{\rm rel}$	$-90.5^{+6.4}_{-6.3}$					
σ_J	$13.3^{+13}_{-5.4}$					
TOI-3688						
	i'	TESS				
u_1	0.280 ± 0.052	$0.279^{+0.052}_{-0.051}$				
u_2	$0.286^{+0.050}_{-0.051}$	0.285 ± 0.051				
A_D	⋯	0.010 ± 0.031				
	NEID					
$\gamma_{\rm rel}$	$-146.3^{+9.6}_{-8.8}$					
σ_J	$18^{+17}_{-10.}$					
TOI-3807						
	B	*R*	i'	r'	z'	TESS
u_1	0.681 ± 0.042	0.382 ± 0.051	0.320 ± 0.051	$0.413^{+0.050}_{-0.051}$	0.249 ± 0.050	0.315 ± 0.032
u_2	0.125 ± 0.039	0.276 ± 0.050	$0.282^{+0.050}_{-0.049}$	0.277 ± 0.049	$0.273^{+0.050}_{-0.049}$	0.278 ± 0.030
A_D	⋯	⋯	⋯	⋯	⋯	$0.178^{+0.066}_{-0.075}$
	NEID					
$\gamma_{\rm rel}$	-28660 ± 13					
σ_J	25^{+30}_{-13}					
TOI-3819						
	R	i'	TESS			
u_1	$0.384^{+0.053}_{-0.052}$	0.314 ± 0.049	0.294 ± 0.025			
u_2	$0.299^{+0.050}_{-0.051}$	$0.298^{+0.049}_{-0.048}$	0.279 ± 0.023			
A_D	⋯	⋯	$-0.00000^{+0.00042}_{-0.00043}$			
	NEID					
$\gamma_{\rm rel}$	30839^{+16}_{-17}					
σ_J	33^{+36}_{-16}					
TOI-3912						
	B	*R*	i'	TESS		

Table 11
(Continued)

Parameter					
u_1	$0.683^{+0.041}_{-0.042}$	0.387 ± 0.052	$0.358^{+0.034}_{-0.035}$	0.311 ± 0.034	
u_2	0.126 ± 0.039	0.278 ± 0.050	0.301 ± 0.034	$0.266^{+0.035}_{-0.034}$	
A_D	⋯	⋯	⋯	$0.000000^{+0.000090}_{-0.000089}$	
	HIRES				
$\gamma_{\rm rel}$	12.2 ± 6.2				
σ_J	$13.4^{+10.}_{-5.4}$				
TOI-3976					
	i'	TESS			
u_1	0.226 ± 0.050	0.299 ± 0.030			
u_2	0.244 ± 0.049	$0.310^{+0.029}_{-0.030}$			
A_D	⋯	-0.00005 ± 0.00060			
	HIRES				
$\gamma_{\rm rel}$	2.0 ± 2.6				
σ_J	$6.6^{+3.7}_{-3.0}$				
TOI-4087					
	B	R	TESS		
u_1	0.581 ± 0.052	0.348 ± 0.048	$0.250^{+0.016}_{-0.017}$		
u_2	0.175 ± 0.051	0.314 ± 0.049	0.286 ± 0.019		
A_D	⋯	⋯	0.00000 ± 0.00019		
	NEID	TRES			
$\gamma_{\rm rel}$	-14263^{+15}_{-14}	152^{+65}_{-64}			
σ_J	31^{+23}_{-12}	166^{+71}_{-48}			
TOI-4145					
	B	I	TESS		
u_1	$0.802^{+0.054}_{-0.056}$	0.351 ± 0.051	0.396 ± 0.029		
u_2	0.029 ± 0.054	0.219 ± 0.050	0.233 ± 0.026		
A_D	⋯	⋯	0.0009 ± 0.0064		
	NEID				
$\gamma_{\rm rel}$	1836^{+12}_{-13}				
σ_J	$32^{+19}_{-10.}$				
TOI- 4463					
	R	g'	r'	z'	TESS
u_1	0.411 ± 0.053	0.626 ± 0.051	$0.427^{+0.049}_{-0.050}$	0.267 ± 0.049	0.342 ± 0.049
u_2	0.262 ± 0.051	$0.150^{+0.052}_{-0.051}$	0.258 ± 0.050	0.261 ± 0.049	0.267 ± 0.048
A_D	⋯	⋯	⋯	⋯	0.010 ± 0.025
	NEID				
$\gamma_{\rm rel}$	$-90370.8^{+2.2}_{-2.0}$				
σ_J	$2.5^{+5.5}_{-2.5}$				
TOI-4791					
	R	TESS			
u_1	0.318 ± 0.051	0.275 ± 0.035			
u_2	0.295 ± 0.050	0.300 ± 0.035			
A_D	⋯	$-0.071^{+0.069}_{-0.080}$			
	CHIRON				
$\gamma_{\rm rel}$	33780^{+29}_{-25}				
σ_J	38^{+69}_{-38}				

ORCID iDs

Samuel W. Yee https://orcid.org/0000-0001-7961-3907
Joshua N. Winn https://orcid.org/0000-0002-4265-047X
Joel D. Hartman https://orcid.org/0000-0001-8732-6166
Luke G. Bouma https://orcid.org/0000-0002-0514-5538
George Zhou https://orcid.org/0000-0002-4891-3517
Samuel N. Quinn https://orcid.org/0000-0002-8964-8377
David W. Latham https://orcid.org/0000-0001-9911-7388
Allyson Bieryla https://orcid.org/0000-0001-6637-5401
Joseph E. Rodriguez https://orcid.org/0000-0001-8812-0565
Karen A. Collins https://orcid.org/0000-0001-6588-9574
Owen Alfaro https://orcid.org/0000-0003-0125-0039
Khalid Barkaoui https://orcid.org/0000-0003-1464-9276
Corey Beard https://orcid.org/0000-0001-7708-2364
Alexander A. Belinski https://orcid.org/0000-0003-3469-0989
Zouhair Benkhaldoun https://orcid.org/0000-0001-6285-9847
Paul Benni https://orcid.org/0000-0001-6981-8722
Krzysztof Bernacki https://orcid.org/0000-0003-4647-7114
Andrew W. Boyle https://orcid.org/0000-0001-6037-2971
R. Paul Butler https://orcid.org/0000-0003-1305-3761
Douglas A. Caldwell https://orcid.org/0000-0003-1963-9616
Ashley Chontos https://orcid.org/0000-0003-1125-2564
Jessie L. Christiansen https://orcid.org/0000-0002-8035-4778
David R. Ciardi https://orcid.org/0000-0002-5741-3047
Kevin I. Collins https://orcid.org/0000-0003-2781-3207
Dennis M. Conti https://orcid.org/0000-0003-2239-0567
Jeffrey D. Crane https://orcid.org/0000-0002-5226-787X
Tansu Daylan https://orcid.org/0000-0002-6939-9211
Courtney D. Dressing https://orcid.org/0000-0001-8189-0233
Jason D. Eastman https://orcid.org/0000-0003-3773-5142
Zahra Essack https://orcid.org/0000-0002-2482-0180
Phil Evans https://orcid.org/0000-0002-5674-2404
Mark E. Everett https://orcid.org/0000-0002-0885-7215
Sergio Fajardo-Acosta https://orcid.org/0000-0001-9309-0102
Raquel Forés-Toribio https://orcid.org/0000-0002-6482-2180
Elise Furlan https://orcid.org/0000-0001-9800-6248
Michaël Gillon https://orcid.org/0000-0003-1462-7739
Coel Hellier https://orcid.org/0000-0002-3439-1439
Ian Helm https://orcid.org/0000-0002-0473-4437
Andrew W. Howard https://orcid.org/0000-0001-8638-0320
Steve B. Howell https://orcid.org/0000-0002-2532-2853
Howard Isaacson https://orcid.org/0000-0002-0531-1073
Emmanuel Jehin https://orcid.org/0000-0001-8923-488X
Jon M. Jenkins https://orcid.org/0000-0002-4715-9460
Eric L. N. Jensen https://orcid.org/0000-0002-4625-7333
John F. Kielkopf https://orcid.org/0000-0003-0497-2651
Naunet Leonhardes-Barboza https://orcid.org/0000-0001-5782-3719
Pablo Lewin https://orcid.org/0000-0003-0828-6368
Sarah E. Logsdon https://orcid.org/0000-0002-9632-9382
Jack Lubin https://orcid.org/0000-0001-7047-8681
Michael B. Lund https://orcid.org/0000-0003-2527-1598
Mason G. MacDougall https://orcid.org/0000-0003-2562-9043
Andrew W. Mann https://orcid.org/0000-0003-3654-1602
Natalia A. Maslennikova https://orcid.org/0000-0003-4147-5195
Bob Massey https://orcid.org/0000-0001-8879-7138
Kim K. McLeod https://orcid.org/0000-0001-9504-1486
Jose A. Muñoz https://orcid.org/0000-0001-9833-2959
Patrick Newman https://orcid.org/0000-0003-3848-3418
Valeri Orlov https://orcid.org/0000-0002-4650-2984
Peter Plavchan https://orcid.org/0000-0002-8864-1667
Adam Popowicz https://orcid.org/0000-0003-3184-5228
Francisco J. Pozuelos https://orcid.org/0000-0003-1572-7707
Don J. Radford https://orcid.org/0000-0002-3940-2360
Michael Reefe https://orcid.org/0000-0003-4701-8497
George R. Ricker https://orcid.org/0000-0003-2058-6662
Boris S. Safonov https://orcid.org/0000-0003-1713-3208
Richard P. Schwarz https://orcid.org/0000-0001-8227-1020
Heidi Schweiker https://orcid.org/0000-0001-9580-4869
Nicholas J. Scott https://orcid.org/0000-0003-1038-9702
S. Seager https://orcid.org/0000-0002-6892-6948
Stephen A. Shectman https://orcid.org/0000-0002-8681-6136
Chris Stockdale https://orcid.org/0000-0003-2163-1437
Thiam-Guan Tan https://orcid.org/0000-0001-5603-6895
Roland Vanderspek https://orcid.org/0000-0001-6763-6562
David Vermilion https://orcid.org/0000-0002-4501-564X
David Watanabe https://orcid.org/0000-0002-3555-8464
Lauren M. Weiss https://orcid.org/0000-0002-3725-3058
Richard G. West https://orcid.org/0000-0001-6604-5533
Judah Van Zandt https://orcid.org/0000-0002-4290-6826
Carl Ziegler https://orcid.org/0000-0002-0619-7639

References

Adams, F. C., & Laughlin, G. 2006, ApJ, 649, 1004
Agol, E., Luger, R., & Foreman-Mackey, D. 2020, AJ, 159, 123
Astropy Collaboration, Price-Whelan, A. M., Sipőcz, B. M., et al. 2018, AJ, 156, 123
Astropy Collaboration, Robitaille, T. P., Tollerud, E. J., et al. 2013, A&A, 558, A33
Bailey, J. I., Mateo, M., White, R. J., Shectman, S. A., & Crane, J. D. 2018, MNRAS, 475, 1609
Baranne, A., Queloz, D., Mayor, M., et al. 1996, A&AS, 119, 373
Baratella, M., D'Orazi, V., Carraro, G., et al. 2020, A&A, 634, A34
Barkaoui, K., Burdanov, A., Hellier, C., et al. 2019, AJ, 157, 43
Barnes, S. A., Weingrill, J., Granzer, T., Spada, F., & Strassmeier, K. G. 2015, A&A, 583, A73
Beleznay, M., & Kunimoto, M. 2022, MNRAS, 516, 75
Berger, T. A., Howard, A. W., & Boesgaard, A. M. 2018, ApJ, 855, 115
Bossini, D., Vallenari, A., Bragaglia, A., et al. 2019, A&A, 623, A108
Bouma, L. G., Curtis, J. L., Hartman, J. D., Winn, J. N., & Bakos, G. Á. 2021, AJ, 162, 197
Bouma, L. G., Hartman, J. D., Bhatti, W., Winn, J. N., & Bakos, G. Á. 2019, ApJS, 245, 13
Brahm, R., Jordán, A., Hartman, J., & Bakos, G. 2017, MNRAS, 467, 971
Brahm, R., Nielsen, L. D., Wittenmyer, R. A., et al. 2020, AJ, 160, 235
Brown, A. G. A., Vallenari, A., Prusti, T., et al. 2021, A&A, 649, A1
Brown, T. M., Baliber, N., Bianco, F. B., et al. 2013, PASP, 125, 1031
Buchhave, L. A., Bitsch, B., Johansen, A., et al. 2018, ApJ, 856, 37
Buchhave, L. A., Bakos, G. Á., Hartman, J. D., et al. 2010, ApJ, 720, 1118
Buchhave, L. A., Latham, D. W., Johansen, A., et al. 2012, Natur, 486, 375
Butler, R. P., Marcy, G. W., Williams, E., et al. 1996, PASP, 108, 500
Caldwell, D. A., Tenenbaum, P., Twicken, J. D., et al. 2020, RNAAS, 4, 201
Carter, J. A., & Agol, E. 2013, ApJ, 765, 132

Castelli, F., & Kurucz, R. L. 2003, in IAU Symp. 210, Modelling of Stellar Atmospheres, ed. N. Piskunov et al. (San Francisco, CA: ASP), A20
Choi, J., Dotter, A., Conroy, C., et al. 2016, ApJ, 823, 102
Claret, A. 2017, A&A, 600, A30
Claret, A., & Bloemen, S. 2011, A&A, 529, A75
Cameron, A. C., & Jardine, M. 2018, MNRAS, 476, 2542
Collins, K., Quinn, S. N., Latham, D. W., et al. 2018, AAS Meeting, 231, 439.08
Collins, K. A., Kielkopf, J. F., Stassun, K. G., & Hessman, F. V. 2017, AJ, 153, 77
Crane, J. D., Shectman, S. A., & Butler, R. P. 2006, Proc. SPIE, 6269, 626931
Crane, J. D., Shectman, S. A., Butler, R. P., et al. 2010, Proc. SPIE, 7735, 773553
Crane, J. D., Shectman, S. A., Butler, R. P., et al. 2008, Proc. SPIE, 7014, 701479
Curtis, J. L., Agueros, M. A., Douglas, S. T., & Meibom, S. 2019, ApJ, 879, 49
Cutri, R. M., Skrutskie, M. F., van Dyk, S., et al. 2003, yCat, II/246
Cutri, R. M. 2012, yCat, II/311
Dalba, P. A., Fulton, B., Isaacson, H., Kane, S. R., & Howard, A. W. 2020, AJ, 160, 149
Davis, A. B., Wang, S., Jones, M., et al. 2020, AJ, 160, 229
Dawson, R. I., & Johnson, J. A. 2018, ARA&A, 56, 175
Dawson, R. I., & Murray-Clay, R. A. 2013, ApJL, 767, L24
Delgado Mena, E., Bertran de Lis, S., Adibekyan, V. Z., et al. 2015, A&A, 576, A69
Demory, B.-O., & Seager, S. 2011, ApJS, 197, 12
Donati, J.-F., Semel, M., Carter, B. D., Rees, D. E., & Cameron, A. C. 1997, MNRAS, 291, 658
Dotter, A. 2016, ApJS, 222, 8
Douglas, S. T., Agueros, M. A., Covey, K. R., et al. 2017, ApJ, 842, 83
Eastman, J., Gaudi, B. S., & Agol, E. 2013, PASP, 125, 83
Eastman, J. D., Rodriguez, J. E., Agol, E., et al. 2019, arXiv:1907.09480
El-Badry, K., Rix, H.-W., & Heintz, T. M. 2021, MNRAS, 506, 2269
ExoFOP 2019, Exoplanet Follow-up Observing Program—TESS, IPAC doi:10.26134/EXOFOP3
Fausnaugh, M. M., Burke, C. J., Ricker, G. R., & Vanderspek, R. 2020, RNAAS, 4, 251
Feinstein, A. D., Montet, B. T., Foreman-Mackey, D., et al. 2019, PASP, 131, 094502
Fűrész, G. 2008, PhD thesis, Univ. of Szeged, Hungary
Figueira, P., Faria, J. P., Delgado-Mena, E., et al. 2014, A&A, 570, A21
Fortney, J. J., Dawson, R. I., & Komacek, T. D. 2021, JGRE, 126, e2020JE006629
Fressin, F., Torres, G., Charbonneau, D., et al. 2013, ApJ, 766, 81
Fritzewski, D. J., Barnes, S. A., James, D. J., & Strassmeier, K. G. 2020, A&A, 641, A51
Fritzewski, D. J., Barnes, S. A., James, D. J., & Strassmeier, K. G. 2021, A&A, 652, A60
Gaia Collaboration, Vallenari, A., Brown, A., & Prusti, T. 2022, A&A, in press
Gavel, D., Kupke, R., Dillon, D., et al. 2014, Proc. SPIE, 9148, 914805
Gelman, A., & Rubin, D. B. 1992, StaSc, 7, 457
Gillon, M., Jehin, E., Magain, P., et al. 2011, EPJWC, 11, 06002
Gillon, M., Anderson, D. R., Collier-Cameron, A., et al. 2013, A&A, 552, A82
Ginsburg, A., Sipocz, B. M., Brasseur, C. E., et al. 2019, AJ, 157, 98
Gray, R. O. 1999, SPECTRUM: A stellar spectral synthesis program, Astrophysics Source Code Library, ascl:9910.002
Guerrero, N. M., Seager, S., Huang, C. X., et al. 2021, ApJS, 254, 39
Halverson, S., Terrien, R., Mahadevan, S., et al. 2016, Proc. SPIE, 9908, 99086P
Harris, C. R., Millman, K. J., van der Walt, S. J., et al. 2020, Natur, 585, 357
Hartman, J. D., & Bakos, G. Á 2016, A&C, 17, 1
Hartman, J. D., Bakos, G. Á., Bayliss, D., et al. 2019, AJ, 157, 55
Hayward, T. L., Brandl, B., Pirger, B., et al. 2001, PASP, 113, 105
Healy, B. F., & McCullough, P. R. 2020, ApJ, 903, 99
Hirano, T., Suto, Y., Taruya, A., et al. 2010, ApJ, 709, 458
Hirano, T., Suto, Y., Winn, J. N., et al. 2011, ApJ, 742, 69
Høg, E., Fabricius, C., Makarov, V. V., et al. 2000, A&A, 355, L27
Horch, E. P., Howell, S. B., Everett, M. E., & Ciardi, D. R. 2014, ApJ, 795, 60
Howard, A. W., & Fulton, B. J. 2016, PASP, 128, 114401
Howard, A. W., Johnson, J. A., W. Marcy, G., et al. 2010, ApJ, 721, 1467
Howell, S. B., Everett, M. E., Sherry, W., Horch, E., & Ciardi, D. R. 2011, AJ, 142, 19
Huang, C. X., Vanderburg, A., Pál, A., et al. 2020a, RNAAS, 4, 204
Huang, C. X., Vanderburg, A., Pál, A., et al. 2020b, RNAAS, 4, 206
Hunter, J. D. 2007, CSE, 9, 90
Ikwut-Ukwa, M., Rodriguez, J. E., Quinn, S. N., et al. 2021, AJ, 163, 9
Israelian, G., Mena, E. D., Santos, N. C., et al. 2009, Natur, 462, 189
Jehin, E., Jehin, E., Gillon, M., et al. 2011, Msngr, 145, 2
Jenkins, J. M., Twicken, J. D., McCauliff, S., et al. 2016, Proc. SPIE, 9913, 99133E
Jensen, E. 2013, Tapir: A web interface for transit/eclipse observability, Astrophysics Source Code Library, ascl:1306.007
Katz, D., Sartoretti, P., Guerrier, A., et al. 2022, arXiv:2206.05902
Kipping, D. M. 2010, MNRAS, 408, 1758
Knudstrup, E., Serrano, L. M., Gandolfi, D., et al. 2022, A&A, 667, A22
Kostov, V. B., Mullally, S. E., Quintana, E. V., et al. 2019, AJ, 157, 124
Kounkel, M., & Covey, K. 2019, AJ, 158, 122
Kovács, G., Zucker, S., & Mazeh, T. 2002, A&A, 391, 369
Kruse, E., Agol, E., Luger, R., & Foreman-Mackey, D. 2019, ApJS, 244, 11
Kunimoto, M., Huang, C., Tey, E., et al. 2021, RNAAS, 5, 234
Kunimoto, M., Daylan, T., Guerrero, N., et al. 2022, ApJS, 259, 33
Kupke, R., Gavel, D., Roskosi, C., et al. 2012, Proc. SPIE, 8447, 84473G
Kurucz, R. L. 1993, SYNTHE spectrum synthesis programs and line data (Cambridge, MA: Smithsonian Astrophysical Observatory)
Lightkurve Collaboration, Cardoso, J. V. d. M., & Hedges, C. 2018, Lightkurve: Kepler and TESS time series analysis in Python, Astrophysics Source Code Library, ascl:1812.013
Lindegren, L., Klioner, S. A., Hernández, J., et al. 2021, A&A, 649, A2
Lissauer, J. J. 1993, ARA&A, 31, 129
Mandel, K., & Agol, E. 2002, ApJL, 580, L171
Matson, R. A., Howell, S. B., Horch, E. P., & Everett, M. E. 2018, AJ, 156, 31
Maxted, P. F. L., Serenelli, A. M., & Southworth, J. 2015, A&A, 577, A90
Mayor, M., Marmier, M., Lovis, C., et al. 2011, arXiv:1109.2497
McGurk, R., Rockosi, C., Gavel, D., et al. 2014, Proc. SPIE, 9148, 91483A
McKinney, W. 2010, in Proc. 9th Python in Science Conf., ed. S. van der Walt & J. Millman, 56
McLaughlin, D. B. 1924, ApJ, 60, 22
Meingast, S., Alves, J., & Rottensteiner, A. 2021, A&A, 645, A84
Mireles, I., Hesse, K., Guerrero, N., et al. 2021, Results from the Evaluation of Community TOIs, Zenodo doi:10.5281/zenodo.5130661
Montalto, M., Borsato, L., Granata, V., et al. 2020, MNRAS, 498, 1726
Mordasini, C., Alibert, Y., Benz, W., Klahr, H., & Henning, T. 2012, A&A, 541, A97
Morton, T. D. 2015, isochrones: Stellar model grid package, Astrophysics Source Code Library, ascl:1503.010
NASA Exoplanet Archive 2022, Planetary Systems Composite Parameters, v2022-02-14 NExScI-Caltech/IPAC, doi:10.26133/NEA13
NExScI 2022, Exoplanet Follow-up Observing Program Web Service IPAC, doi:10.26134/EXOFOP5
Nielsen, L. D., Brahm, R., Bouchy, F., et al. 2020, A&A, 639, A76
Olmschenk, G., Ishitani Silva, S., Rau, G., et al. 2021, AJ, 161, 273
Oshagh, M., Boisse, I., Boué, G., et al. 2013, A&A, 549, A35
Oshagh, M., Triaud, A. H. M. J., Burdanov, A., et al. 2018, A&A, 619, A150
Pal, A. 2012, MNRAS, 421, 1825
pandas development team 2020, pandas-dev/pandas: Pandas, Zenodo, doi:10.5281/zenodo.3509134
Paredes, L. A., Henry, T. J., Quinn, S. N., et al. 2021, AJ, 162, 176
Penev, K., Bouma, L. G., Winn, J. N., & Hartman, J. D. 2018, AJ, 155, 165
Pepe, F., Mayor, M., Galland, F., et al. 2002, A&A, 388, 632
Petigura, E. A. 2015, PhD thesis, Univ. of California, Berkeley
Pollacco, D. L., Skillen, I., Cameron, A. C., et al. 2006, PASP, 118, 1407
Psaridi, A., Bouchy, F., Lendl, M., et al. 2022, A&A, 664, A94
Quinn, S. N., White, R. J., Latham, D. W., et al. 2012, ApJL, 756, L33
Reefe, M., Alfaro, O., Foster, S., et al. 2022, JATIS, 8, 027002
Riello, M., Angeli, F. D., Evans, D. W., et al. 2021, A&A, 649, A3
Rodriguez, J. E., Quinn, S. N., Huang, C. X., et al. 2019, AJ, 157, 191
Rodriguez, J. E., Quinn, S. N., Zhou, G., et al. 2021, AJ, 161, 194
Rodriguez, J. E., Quinn, S. N., Vanderburg, A., et al. 2022, arXiv:2205.05709
Rossiter, R. A. 1924, ApJ, 60, 15
Safonov, B. S., Lysenko, P. A., & Dodin, A. V. 2017, AstL, 43, 344
Santos, N. C., Israelian, G., & Mayor, M. 2004, A&A, 415, 1153
Savel, A. B., Dressing, C. D., Hirsch, L. A., et al. 2020, AJ, 160, 287
Schlafly, E. F., & Finkbeiner, D. P. 2011, ApJ, 737, 103
Schlegel, D. J., Finkbeiner, D. P., & Davis, M. 1998, ApJ, 500, 525
Schwab, C., Rakich, A., Gong, Q., et al. 2016, Proc. SPIE, 9908, 99087H
Schwarz, G. 1978, AnSta, 6, 461
Scott, N. J., Howell, S. B., Horch, E. P., & Everett, M. E. 2018, PASP, 130, 054502
Scott, N. J., Howell, S. B., Gnilka, C. L., et al. 2021, FrASS, 8, 138
Seager, S., & Mallen-Ornelas, G. 2003, ApJ, 585, 1038
Sha, L., Huang, C. X., Shporer, A., et al. 2021, AJ, 161, 82
Shallue, C. J., & Vanderburg, A. 2018, AJ, 155, 94

Skrutskie, M. F., Cutri, R. M., Stiening, R., et al. 2006, AJ, 131, 1163
Smith, J. C., Stumpe, M. C., Van Cleve, J. E., et al. 2012, PASP, 124, 1000
Soderblom, D. R. 2010, ARA&A, 48, 581
Soderblom, D. R., Jones, B. F., Balachandran, S., et al. 1993, AJ, 106, 1059
Stassun, K. G., Oelkers, R. J., Pepper, J., et al. 2018, AJ, 156, 102
Stassun, K. G., Oelkers, R. J., Paegert, M., et al. 2019, AJ, 158, 138
Stumpe, M. C., Smith, J. C., Catanzarite, J. H., et al. 2014, PASP, 126, 100
Stumpe, M. C., Smith, J. C., Van Cleve, J. E., et al. 2012, PASP, 124, 985
Tejada Arevalo, R. A., Winn, J. N., & Anderson, K. R. 2021, ApJ, 919, 138
Tinetti, G., Drossart, P., Eccleston, P., et al. 2016, Proc. SPIE, 9904, 99041X
Tokovinin, A. 2018, PASP, 130, 035002
Tokovinin, A., & Cantarutti, R. 2008, PASP, 120, 170
Tokovinin, A., Fischer, D. A., Bonati, M., et al. 2013, PASP, 125, 1336
Valenti, J. A., & Fischer, D. A. 2005, ApJS, 159, 141
Vanderburg, A., & Johnson, J. A. 2014, PASP, 126, 948
Virtanen, P., Gommers, R., Oliphant, T. E., et al. 2020, NatMe, 17, 261
Vogt, S. S., Allen, S. L., Bigelow, B. C., et al. 1994, Proc. SPIE, 2198, 362
Wong, I., Shporer, A., Zhou, G., et al. 2021, AJ, 162, 256
Wright, J. T., Marcy, G. W., Howard, A. W., et al. 2012, ApJ, 753, 160
Yee, S. W., Petigura, E. A., & von Braun, K. 2017, ApJ, 836, 77
Yee, S. W., Winn, J. N., & Hartman, J. D. 2021, AJ, 162, 240
Yee, S. W., Winn, J. N., Hartman, J. D., et al. 2022, AJ, 164, 70
Yu, L., Vanderburg, A., Huang, C., et al. 2019, AJ, 158, 25
Zhou, G., Huang, C. X., Bakos, G. Á., et al. 2019, AJ, 158, 141
Zhou, G., Quinn, S. N., Irwin, J., et al. 2020, AJ, 161, 2
Ziegler, C., Tokovinin, A., & Brice no, C. 2019, AJ, 159, 19
Ziegler, C., Tokovinin, A., Latiolais, M., et al. 2021, AJ, 162, 192